Material Flow Analysis of Similar and Dissimilar Friction Stir Welding

A Thesis Submitted in

Partial Fulfillment of the Requirements

for the Degree of

DOCTOR OF PHILOSOPHY

by

ARUN KUMAR KADIAN

(Roll No. 126103029)

DEPARTMENT OF MECHANICAL ENGINEERING

INDIAN INSTITUTE OF TECHNOLOGY GUWAHATI

GUWAHATI-781039, INDIA

December 2018

DEPARTMENT OF MECHANICAL ENGINEERING
INDIAN INSTITUTE OF TECHNOLOGY GUWAHATI
GUWAHATI–781039, ASSAM, INDIA

CERTIFICATE

This is to certify that the thesis entitled **"Material Flow Analysis of Similar and Dissimilar Friction Stir Welding"** submitted by **Mr. Arun Kumar Kadian (Reg. No. 126103029)** to the Department of Mechanical Engineering, Indian Institute of Technology Guwahati, is a record of original research work carried out under my supervision and it has not been submitted elsewhere for the award of any other degree or diploma.

The thesis in my opinion, has reached the standard fulfilling the requirements for the award of degree of Doctor of Philosophy in accordance with the regulations of the institute.

Prof. Pankaj Biswas

Department of Mechanical Engineering,
Indian Institute of Technology Guwahati,
Guwahati – 781039, India

21st December, 2018

Declaration

I declare that the present written submission is my thoughts in my own words. I have adequately cited and referenced the original sources, where others' works have been involved. I also declare that I have followed all principles of academic morality and honesty and have neither fabricated nor falsified any idea/data in the present thesis. I realize that any defilement of the above will be cause for disciplinary action by the Institute and can also induce disciplinary action from the sources which have thus not been properly cited.

(Arun Kumar Kadian)

Dated: 21st December, 2018

Reg. No. 126103029

Dedicated

To

My Family

ACKNOWLEDGEMENTS

I would like to express my heartfelt gratitude towards all those who have immensely helped me during this long arduous journey and eventually assisted me to emerge as an experienced researcher and a mature individual.

First and foremost, I must express my deepest sense of appreciation and respect for my thesis supervisor Prof. Pankaj Biswas for providing me the opportunity to work under their supervision. His persistent patience and friendliness in the moments of difficulties have always been remembered and also his constant encouragement have played a crucial role in writing the thesis and bringing it to its present form.

I would like to thank my doctoral committee members, Prof. P. S. Robi, Prof. M. Das, and Prof. T. K. Mandal for carefully reading the reports at various stages of evaluation and providing many useful comments, which have helped in the development of this thesis.

My sincere gratefulness to past and present departmental heads Prof. D. Chakraborty, Prof. P. Mahanta, Prof. A. K. Dass and Prof. S. K. Dwivedy for their kind permission for enrollment, registration and several important supports at IIT Guwahati. I am also grateful to all the faculty members of Mechanical Engineering Department for giving me a comfortable and friendly environment for pursuing my research. I would also like to acknowledge the contribution of office staff, for helping me with various academic as well as non-academic issues.

I would like to express my sense of gratitude to Mr. N K Das, present Assistant Workshop Superintendent and all the staffs of the workshop specially Mr. Dilip Chetri, Mr. Dipak K. Deka, Mr. Chandan Banikya, Mr. Minesh Ch. Medhi, Mr. Nidul Saikia and Mr. Amzad Khan for extending their help in fabrication of the different experimental set-ups for this work.

I also wise to express my gratitude to the Central Instrument Facility, IIT Guwahati to providing technical support with SEM, and FESEM.

The financial support of this research, which was provided by the Department of Mechanical Engineering, Indian Institute of Technology Guwahati, is gratefully acknowledged.

The most important support for this work came from my parents, Sri. Naresh Kumar Kadian and Smt. Raj Bala Kadian, and my siblings, Mr. Varun Kumar Kadian and Miss Komal Kadian for encouraging me to go still further at every points of life. I would like to thank my extended family for all of their love and support through the years, especially at peak of the economy encouraged me to pursue Ph.D on a modest stipend.

Finally the friends form an important part of this long and enduring journey, and without their constant support and encouragement, the completion of this thesis perhaps would have been an impossible task. I express my sincere thanks to Dr. Anil Deepati, Dr. Arpan Mondal, Mr. Biplab Das, Dr. Syed Shahanawazuddin, Mr Shatrughan Jaiswal and Mr. Rajendra Soni for their help and support.

I acknowledge the moral support of Prof. S. N. Bora, Mrs. Swapnali Bora, Prof. Gagan Kumar, Dr. Punit Sharma, Dr. Pankaj Singh, Mr. Gaurav Kumar, Mr. Ashutosh Singh, Mr. Kishor Gajrani, Mr. Anand Aggarwal, Mr. Mukul Parmanand, Mr. Shyam Trivedi, Mr. Vinay Kulkarni, Mr. Jimmy Daimari, Mr. Nand Kishor Roy, Mr. Shiv Sahaya Shukla, Mr. Vishesh Singh, Mr. Karam Malik, Mr. Gaurav Saini, Mr. Deepak Joshi, Mr. Subrat Mallick, Dr. Ravindra Patil, my other hostel mates and colleagues. I shall forever be grateful to all my friends and well-wishers.

I consider myself privileged and fortunate to work in the Indian Institute of Technology Guwahati.

Above all, I am thankful to the Almighty.

21st December, 2018 Arun Kumar Kadian

Abstract

The friction stir welding is a solid-state joining process in which joining takes place just below the melting point temperature where the material undergoes high plastic deformation under the influence of rotating tool. The tool and process parameters (like tool rotation speed, tool traverse speed, plunging force, tool geometry) not only affect the welding temperature but also decide the material flow patterns in the welding region. The knowledge of material flow provides the sufficient information to the operator about the selection of right tool geometry in order to obtain a defect-free weld. Therefore in this thesis, the numerical and experimental studies are conducted to understand the material flow behaviour of friction stir welding process.

In this work, the numerical models are created for thermal and material flow analysis of the process. The thermal analysis is conducted using heat generation equations derived based on Coulombs fiction and the plastic deformation heat generation inside the plate. The material flow models for similar and dissimilar friction stir welding are developed to study the material flow behaviour in the weld region. The convective heat loss is considered from all the surfaces and a comparative study has been made with and without the use of temperature dependent material properties and their significance in the finite volume method model. The backing plate heat loss is also considered along with the convective heat loss in the simulation. The material flow analysis of AA6061 weld plates is performed in ANSYS Fluent 14.5. It is observed that the material properties are highly significant in the development of a flow model, therefore temperature and strain rate dependent material properties have been used in the current analysis. The viscosity of the material used in all the models is based on Zener-Holloman parameters which are found to be best-suited for the material flow model. Two types of models are used to study the material flow behaviour i.e. turbulent and laminar model. The material flow velocities are analyzed to predict the flow behaviour and characteristics in friction stir welding. The results obtained from the numerical model are compared with experimental results.

The numerical models further extended to study the influence of seven different tool geometries on material flow. It is observed that the tool pin geometry significantly affects the material flow in the welding region. A swirling motion of the material is

observed in all the cases but it took place at different positions according to different tool pin geometries. A better material mixing is observed with tool having circular pin profile in comparison to the flat pin profiles. It is observed from the viscosity distribution that the conical pins are unable to mix the material properly near the probe tip region.

This study is further extended to analyze the dissimilar friction stir welding. In this case, cylindrical threaded tool geometry is considered to join Aluminium alloy (AA-6061) and Copper alloy (Cu-B370) plates. The model used the volume of fluid (VOF) approach in the commercial FVM package ANSYS fluent 14.5. Experiments are also conducted to validate the model with thermal profiles and optical micrographs. Furthermore, the effect of tool rotational and the welding speed are studied on the material movement. It is found that process parameter had a huge impact on the nugget zone formation during the welding. The tool rotaion and welding speed directly affect the amount of platisized material mixing for conducting the dissimilar friction stir welding.

For further study, the VOF model is extended to analyze the material flow behaviour of a weldment having worm defect. It is found that the influence of tool shoulder is more on the velocity response for defected plate in comparison to undefected plate in the welding region.

Table of contents

List of Figures

List of Tables

Nomenclature

Symbol	Description	Units
r_p	Radius probe	m
l	Height of the probe	m
ω	The angular speed	rpm
Pn	Plunging force	N
P	Pressure	N/m^2
δA	Small elemental area	-
f	Frictional coefficient between the tool and workpiece	-
Q_{s1}	Heat generation due to vertical pressure	W
Q_{s2}	Heat generation due to travelling of shoulder	W
h_1	Depression in the welding	m
S_{ys}^{*}	Yield strength of the material at 80% of the melting point	N/m^2
Q_{p1}	Heat generation due to vertical pressure at probe tip	W
Q_{p2}	Heat generation due to the probe rotational movement	W
Q_{p3}	Heat generation due to travelling of the probe	W
$Q_{sliding}$	Total heat generation due to friction	W
r_p	Tool tip radius	m
r_b	Slant thickness	m
τ^{*}	Shear strength of the material at 80% of its melting point	N/m^2
$Q_{sticking}$	Total heat generation due to material deformation	W

δ	Sliding factor	-
Q_{total}	Total heat generation	W
K	Thermal conductivity	W/mK
T	Temperature	K
ρ	Density of the material	kg/m^3
c	Specific heat	J/kgK
t	Time	s
T_∞	Ambient temperature	K
q_{sup}	Heat flux supplied	W/m^2
q_{conv}	Heat loss due to convection	W
u, v and w	The velocities in the X, Y and Z directions	m/s
Fx, Fy and Fz	Forces in X, Y and Z directions	N
p	Static pressure of the flow field	N/m^2
μ	The viscosity of fluid	Ns/m^2
$\dot{\varepsilon}$	Strain rate	1/s
σ_R	Effective stress	N/m^2
Q	Activation energy (Al)	kJ/mol
R	Universal gas constant	J/molK
Z	Zener-Holloman parameter	1/s
E	Activation energy (Cu)	kJ/mol
β	Volume fraction of the fluid	-
α	Tool area inside Al plate/ the total area of the tool wall	-

Vx	X- component of velocity obtained in results	m/s
Vy	Y- component of velocity obtained in results	m/s
Vz	Z- component of velocity obtained in results	m/s

Chapter 1

Introduction

1.1 Preamble

The Friction Stir Welding (FSW) is a solid-state joining process which is known for its significant advantages over conventional welding methods [1] for softer material like Aluminium (Al), Copper (Cu) etc. The process invented by Thomas et al. [2] at The Welding Institute (TWI), Cambridge, UK and patented in 1991 which requires no filler material or consumable electrode. The welding takes place above the recrystallization temperature (RT) but below the melting point (MP) temperature. Above the RT, the material becomes soft enough that it can be mixed with the help of tool. Since the temperature of welding goes to 80% of the melting point temperature, it is also known as the hot working process. The material adjacent to the tool sticks to the tool wall and moves with rotational movement of the tool. As the tool starts moving along weld line, the fresh material from the front side of the tool pushes the old rotating material or the soft material and replaces it to participate in welding and a welding mixture is left behind the tool. The FSW Process is most suitable for critical applications, for the joining of structural components made of Aluminium and its alloys. The history and evolution of welding, FSW terminology, basic microstructure features of the welding is described in the various section of the chapter. After having the basic understanding of the welding process the governing process parameters are explained with their role in the FSW process

1.2 Motivation

Light weight high strength materials have attracted a lot of industries because of the fast mobility of products in day to day life. Due to product driven economies in the world, countries want lighter products from their industries for mass transportation in order to achieve higher and faster trade. Therefore, the vehicles needed to transport these products have to be lighter such that a larger number of products can be accommodated into the transporting vehicles. Thus, not only buyer based industries

want light weight material but the transport industries also need light weight high strength material to increase the load as well as fuel efficiency [3].

Considering the current scenario, Aluminium is the best-suited material [4]. Earlier, it was quite expensive because of difficult extraction, but the recent advances in past decades led to the higher production of Aluminium [5]. In spite of the desirable properties of Aluminium, industries were not able to use it on a full scale as in many application the joining of metal is required and in this case, the metal is not perfectly suited for welding. The welding of the mentioned metal is difficult to achieve due to the problems caused by the metal oxide. Aluminium is a highly reactive metal with a very high affinity towards the oxygen. Thus, in the open air, it readily reacts with the oxygen present in the atmosphere to form an Aluminium oxide. The Aluminium oxide is a much harder material and having a much higher melting point than the pure Aluminium metal. This oxide layer causes a huge problem in welding in comparison to any other commercial metals [6]. Therefore, a highly skilled worker is required with huge experience in welding to form healthy Aluminium welding joints.

To overcome these welding difficulties, huge researches were carried out in the past few decades. As a result in the year 1991, the welding Institute came up with a new method of friction welding that can weld produce a good quality of butt weld with the help of a spinning tool. This technique is quite new and shown promising results in welding softer metal like Aluminium and Copper. A number of potential advantages of FSW over conventional fusion-welding processes have been identified [7] like good mechanical properties in the as-welded condition, Improved safety due to the absence of toxic fumes or the spatter of molten material, no consumables - so economically cheaper than conventional welding processes, easily automated on simple milling machines - lower setup costs and less training, Low environmental impact- it is also known as green welding and environmental friendly welding technology. According to the survey conducted by AWS, the FSW can save up to $ 34.4 billion per year in the USA. So, the adoption of FSW has increased and 10% of the welding process will be replaced by FSW [8].

1.3 History

Although, the solid state joining process is the oldest joining technique used by the blacksmith in the middle age to make tools and weapons [9], the joining of metal emerged as a manufacturing process in the late 1800's. Since then, the welding processes have undergone many inventions and discoveries [10]. A brief timeline of welding is shown in Figure 1.1.

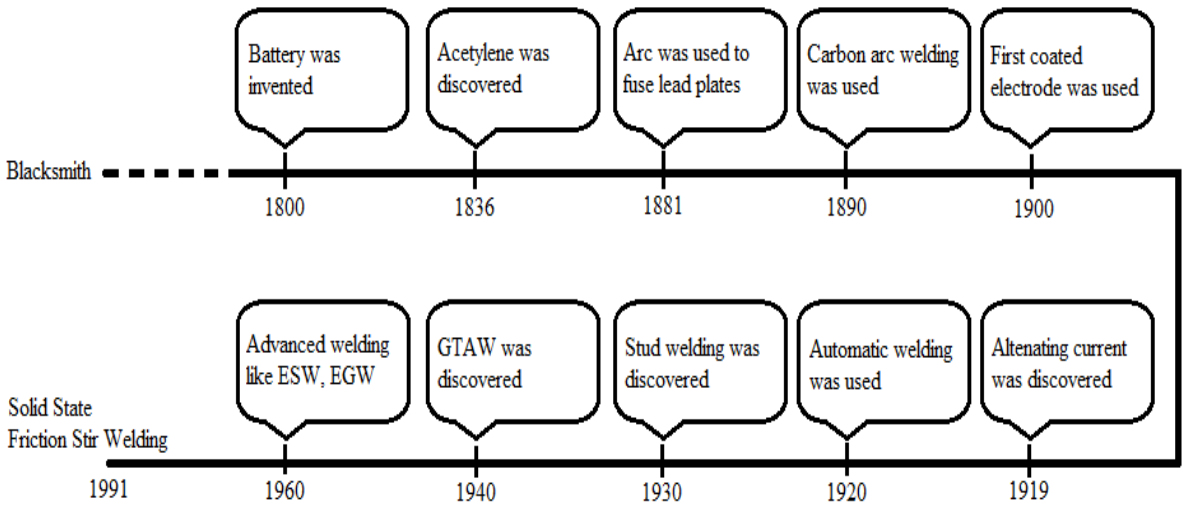

Figure 1.1: Welding timeline (1800-1991) from early age blacksmith to advanced FSW solid state welding.

Till now a lot of welding techniques have been developed that can be categorized based on the methodology as shown in Figure 1.2. Each technique has its pros and cons based on their working principle. So every technique best fits for some special materials. A good welding of mild steel is achieved by fusion technique but Aluminium fusion welding produces defected welds. To weld a soft metal like Al and Cu the FSW showed promising results. A high-quality Al welding can be produced by this method of welding.

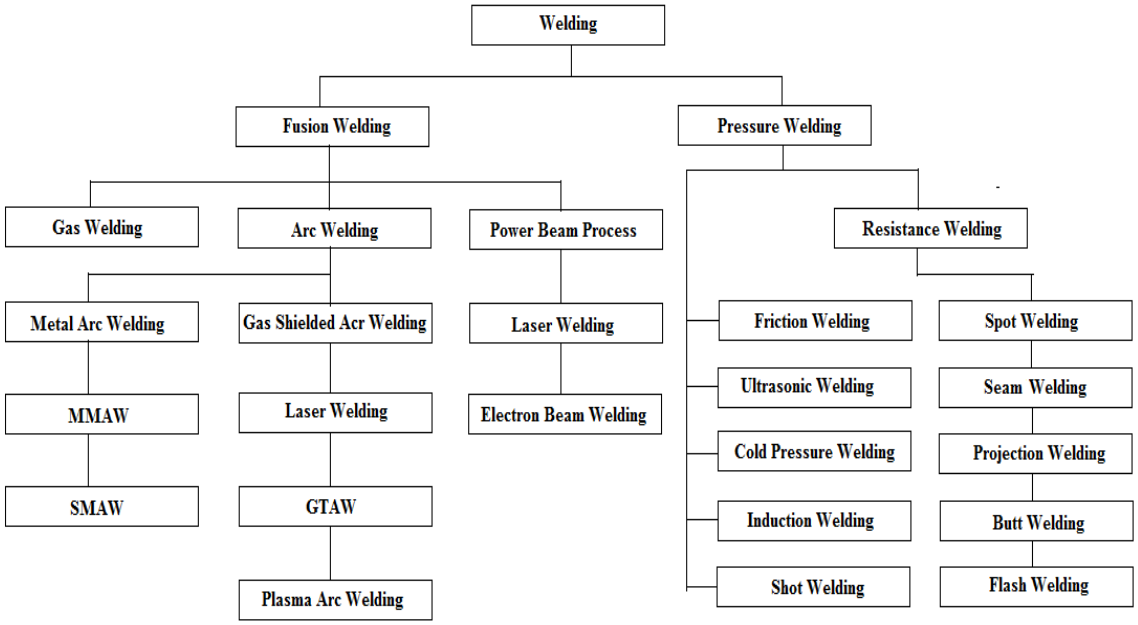

Figure 1.2: Different welding techniques categorized based on their methodology.

1.4 Terminology

The terminology of FSW is very important to have a better understanding of the process. The rotating part is known as a tool which consists of a cylindrical shoulder with a probe/tool pin. The material in which the tool plunged and welded can be called as the work piece/part/sample/welded plate. The line joining the two pieces of the workpieces where the samples are butted together is referred as the weld line. The device used to support and clamp the workpiece is called the anvil/backing plate. The tool rotates at an angular velocity given in revolutions per minute (rpm), which is referred as rotational speed. The translational velocity at which the tool travels along the weld line is called the feed rate or travel/ transverse speed i.e. in millimetre per second (mm/s).

The side of the weld where the angular velocity and forward velocity of the tool is in the same direction is called the advancing side. The other side where the angular velocity and translational velocity are in opposite directions is called the retreating side as shown in Figure 1.3.

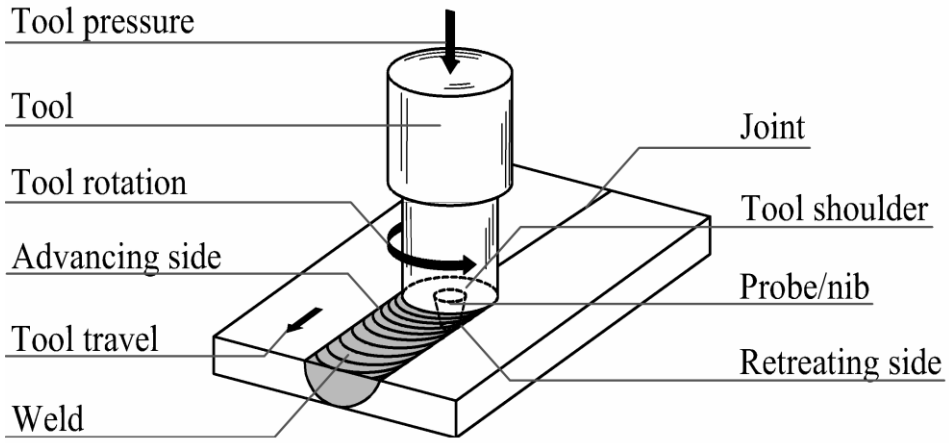

Figure 1.3: Diagram showing various terminologies used in a butt joint FSW with tool rotation and traverse direction.

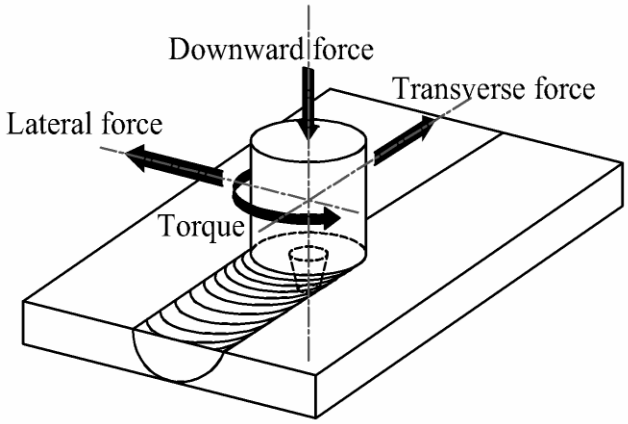

Figure 1.4: Different forces acting in butt joint FSW.

The different component of forces and moment act in three-dimensional spaces is shown in Figure 1.4. The force along the X-axis, Y-axis, and Z-axis have been referred to as the translational (F_x), transverse (F_y) and axial force (F_z) respectively [11], and the unit of force given in Newton's (N). The moment (Mz) about the axis of rotation has been referred to as the torque and given in Newton-meters (N-m).

1.5 Microstructural features

In the FSW process, the microstructure can be broken up into four zones [12] as shown in Figure 1.5. The *stir zone* (also nugget, dynamically recrystallized zone) is a region of heavily deformed material that roughly corresponds to the location of the pin during welding. The grains within the stir zone are roughly equiaxed and often an order of magnitude smaller than the grains in the parent material.

The *flow arm zone* is on the upper surface of the weld and consists of material that is dragged by the shoulder from the retreating side of the weld, around the rear of the tool, and deposited on the advancing side.

The *thermo-mechanically affected zone* (TMAZ) occurs on either side of the stir zone. In this region, the strain and temperature are lower and the effect of welding on the microstructure is correspondingly smaller. Unlike the stir zone, the microstructure is recognizably that of the parent material, albeit significantly deformed and rotated. Although the term TMAZ technically refers to the entire deformed region it is often used to describe any region not already covered by the terms stir zone and flow arm.

The *heat-affected zone* (HAZ) is common to all welding processes. As indicated by the name, this region is subjected to a thermal cycle but is not deformed during welding. The temperatures are lower than those in the TMAZ but may still have a significant effect if the microstructure is thermally unstable. In fact, in age-hardened Aluminium alloys, this region commonly exhibits the poorest mechanical properties.

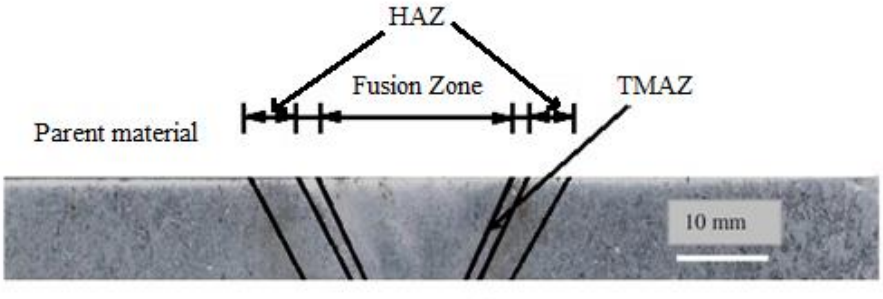

Figure 1.5: Different zones found in FSW [13].

1.6 Process parameters

There are different process parameters on which the friction stir welded material quality depends. It is categorising into two main parts, one is related to tool movement whereas other is related to welding pressure. The tool movement is controlled by the tool rotational and travel speed while welding pressure is controlled by tool tilt, plunge depth and plunging force.

- The *tool rotational and travel speed* play a significant role in heating and cooling of weldment which in turn affects the microstructure of the weld zone. An increase in rotational speed of tool or decrease in its traverse speed results into a hotter weld. In order to produce a successful weld, it is necessary that the material surrounding the tool is hot enough to enable the extensive plastic flow and minimize the forces acting on the tool. If the material is too cool then voids or other flaws may appear in the stir zone and in extreme cases the tool may break.
- The *tool tilt, plunge depth and plunging force* are related to the welding pressure. The plunge depth is defined as the depth of the lowest point of the shoulder below the surface of the welded plate and has been found to be a critical parameter for ensuring weld quality. Plunging the shoulder below the plate surface increases the pressure below the tool and helps to ensure adequate forging of the material at the rear of the tool [14]. Tilting the tool by 2-4 degrees, such that the rear of the tool is lower than the front, has been found to assist this forging process [15]. The plunge depth needs to be correctly set, both to ensure the necessary downward pressure is achieved and to ensure that the tool fully penetrates the weld [16]. Considering a high required load for full penetration of tool may deflect the welding machine, whereas the reduction in plunge depth compared to the nominal setting may result in flaws in the weld [17]. The plunging force has different component as mentioned in section 1.4. A downward force is necessary to maintain the position of the tool at or below the material surface. Some FSW machines operate under load control but in many cases, the vertical position of the tool is pre-set and so the load varies during welding. The traverse force acts parallel to the tool motion and is positive in the traverse direction. Since this force arises as a result of the

resistance of the material to the motion of the tool it might be expected that this force will decrease as the temperature of the material around the tool is increased. The lateral force may act perpendicular to the tool traverse direction and is defined here as positive towards the advancing side of the weld. A torque is required to rotate the tool, the value of which depends upon the down force and friction coefficient (sliding friction) and/or the flow strength of the material in the surrounding region (sticking friction).

1.7 Research objectives

From the detailed review of published research, the following objectives have been made.

- Detailed transient thermal analysis of FSW process which includes heat flux calculation and prediction of transient temperature distribution.
- Prediction of material flow behaviour during the welding period of a similar AA6061 with a suitable thermo-fluid coupled model.
- Study the effect of process parameter on the material flow of butt welded FSW for AA6061.
- Study the effect of different tool pin profiles on the material flow during the welding to obtain the suitable pin profile for the welding.
- Prediction of material flow behaviour during the welding period of Al and Cu alloys with a suitable transient model.
- Study the effect of process parameter on material flow for dissimilar FSW.
- Study the material flow behaviour of a defected plate in comparison to a healthy weld.
- Experimental studies and validations of the numerical methodologies.

1.8 Thesis structure

The content of this thesis focused on thermal and material flow models of FSW for similar and dissimilar materials. The effect of process parameters on the real-time material flow behaviour of the FSW process is one part of this study. The other part contains the behaviour of the material under different tool pin profile. The principal

intention of this study is to find the best tool geometry with suitable process parameter to obtain a healthy and defect-free weld.

The content of this thesis is divided into the following chapters:

- Chapter 1 gives the motivation, basic background on FSW and objectives of the thesis work.
- Chapter 2 provides a detailed review of the various study conducted on FSW through numerical and experimental methods.
- Chapter 3 contributes to the information regarding the methodologies applied to conduct the current numerical and experimental study.
- Chapter 4 presents the results on the transient thermal analysis focused on the process parameter optimization.
- Chapter 5 covers the results regarding the different material flow model used for AA6061 friction welding analysis with experimental validation.
- Chapter 6 contains the material flow behaviour of AA6061 under the influence of different pin profiles and the effect of process parameters on material flow.
- Chapter 7 is dedicated to the material flow modelling of Al and Cu alloys i.e. dissimilar FSW and the study of material flow behaviours according to the process parameter.
- Chapter 8 contains a comparative study of defected and undefected FSW material flow.
- Chapter 9 summarizes the entire work of the thesis, the conclusions drawn from the conducted research and the future scope of this particular area.

1.9 Target applications

The biggest challenge in performing FSW is to get a healthy defect-free weld that depends on the welding process parameters including the tool geometry. The process parameters change the material flow behaviours that either rectify or produce a defect in the welding. The knowledge of material flow patterns provides sufficient information in the selection of right tool for achieving a defect-free weld. The current work provides the detailed information regarding the material flow for different tool geometry used in similar and dissimilar FSW.

Chapter 2

Literature Review

2.1 Introduction

This chapter contains the review of the literature available in the field of FSW related to the objective of the current thesis. The initial section of this chapter provides the information regarding the material selections used in this present work. The section also includes the details about the number of research articles published in the field of FSW. The material selection is followed by the work conducted in the field of the process parameter, microstructural study, tool geometries and common defects found in FSW joints. The current thesis is primarily focused on the material flow behaviour of the similar and dissimilar material. Therefore, the literature related to flow patterns found in the FSW is studied in more details. This chapter also contains the detail literature review on the selection of process parameter, tool geometry, material position and the tool offset used in the dissimilar FSW process. The next section provides the insight of different analytical and numerical simulation models used by the researchers till the date.

2.2 Material selection

Pure Aluminium has the inadequate strength for any industrial application. This weakness of metal can be overcome by alloying with elements like Magnesium, Copper, Manganese, Zinc and Silicon. Desirable properties are achieved by controlling the amount of alloying elements and heat treatments. Aluminium alloys have good ductility and formability due to the face-centred cubic (FCC) microstructure. They are classified in term of series according to the alloying elements. The AA1xxx, AA3xxx and AA5xxx series are non-heat treatable and weldable alloys. Whereas, the AA2xxx, AA6xxx and AA7xxx series are heat treatable and non-weldable alloys [6], [18]. Welding is a very important joining process used in any manufacturing industry. It is a permanent, lightweight and leakproof joining process. There are many methods by which welding can be performed. The fusion welding is the cheapest and fastest of all.

The main problem in fusion welding of Aluminium is the loss of strength and defect formation. Defects like trapped porosity, dissolution of shielding gas, electrode moisture, and flux inclusion are common with fusion welding of Aluminium. Furthermore, the insufficient fusion of high melting (2060ºC) Aluminium oxide and centerline solidification cracking formed during the welding process, add the complexity to the joining process. In contrast, good healthy joints are obtained with no significant loss of mechanical properties with FSW of Aluminium alloys.

As mentioned in the previous chapter this technique is among the new advancements in joining. After the invention of this process by the TWI Institute, the UK in 1991, a lot of research is carried out in order to make this technique easy and commercialized. The general trend of recognized work published in this area by the researcher is shown in Figure 2.1. A rising trend in this research field is observed from 2012 to 2016. In the last 3-4 years, the research output has gone up to 2 times the previous rate of published articles per year.

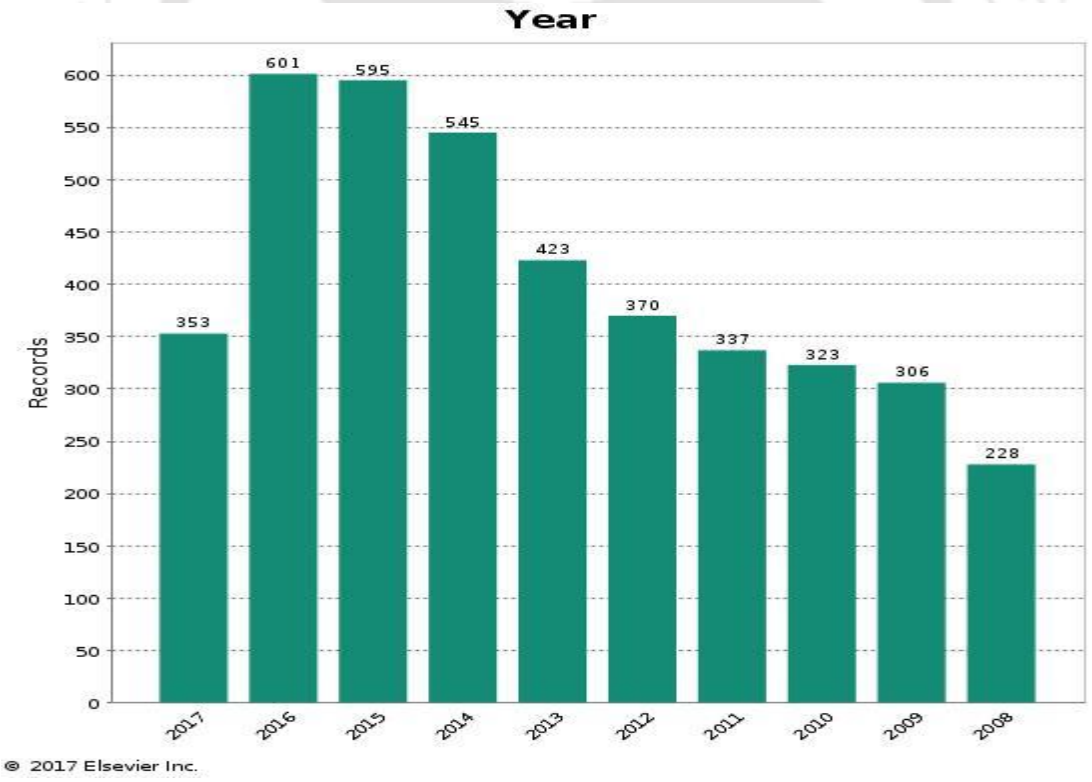

Figure 2.1: Research articles per year (picture from INSPEC-© Elsevier Inc.).

Prior to 2000, very less no of studies were conducted in the field of FSW. Majority of researchers studied the microstructure formed during the welding of unweldable series of welding. After the invention of this newer technique and better testing equipment,

the FSW research is extended to materials like Cu, Mg and harder material like mild steel etc. In 1996, the microstructure formed by fusion and friction welding of AA8009 [19] was compared and found that fusion welding completely destroyed the microstructure distribution while friction welding retained it with a little loss at the welding edges. Another comparison of the microstructure was made among the two alloys of Aluminium AA6061 and AA1100 [20] and found large columnar grain structure in AA1100 plates which are a sign of dynamic recrystallization, a prominent feature of FSW. On the extension of study on AA1100, it was found that the Cold rolled AA1100 plates show better base plate and weld zone hardness than the casted ones [21]. With the help of Transmission electron microscopy (TEM) study conducted on AA6061 friction stir welded plates, it was found that the uniform microstructure precipitations caused the material hardening in the welding region [22]. Later, a similar study was conducted on AA6063 [23] and concluded that the hardness profile depends greatly on precipitations than the grain size. The precipitations formed during the welding were dissolved at higher temperatures. The unweldable alloys like AA7075 [24] were welded through the FSW process but the tensile strength decreased with a minor increase in the ductility in the process. Thus, the temperature at which welding takes place has an important role in microstructure formation in the welding. One such study was conducted on FSW of AA2024 [25]. Two experiments were conducted, (a) at room temperature and (b) at -30ºC (with the help of liquid nitrogen) and studied their microstructures. The microstructure obtained for the low temperature welding was much finer than the room temperature welding. Later, Schofer [26] informed that the lower distortions were observed in low heat input welding of Aluminium alloys. The research was not restricted to similar materials; many studies were conducted on the dissimilar Aluminium alloys due to good welding compatibility. The welding microstructure was studied on AA1100 and AA6061 by Murr et al. [27]. A healthy weld was obtained between the two alloys of Aluminium. However, the study was further extended to obtain another dissimilar welding AA6061 and Cu. A poor weld was obtained between the two materials with a complex microstructure. Later, two unweldable alloys AA6061 and AA2024 were joined at different traverse and rotational speeds.

2.3 Process parameters

The process parameter decides the weld quality as the heat input and strain rate in the weld zone depends on it. There are many process parameters in FSW i.e. tool rotation speed, traverse speed, plunging force, tilt angle. Among these parameters, the most important parameters are tool rotation and traverse speed. The rotational and traverse speed selected by the user inturn select the rate of heat input in the weld zone. Peel et al. [28] gave importance to the heat input instead of material deformation. From the experiments, it was found that mechanical properties of the joint were more affected by heat input produced at a constant rotational speed. The increase in traverse speed led to the shrinkage in the weld zone. Moreover, higher values of longitudinal stresses were obtained at higher values of traverse speed. Therefore, optimal process parameters provided the best mechanical properties of the joint [29]. Lui et al. [30] and Sakthivel et al. [31] created the underwater conditions to study the effect of traverse speed on the microstructure of the weld zone. The grain size increased with the traverse speed for certain limit and decrease with a further rise in traverse speed. Therefore, under all environmental conditions, the narrowing of weld zone is observed with the escalation in traverse speed.

The tensile testing conducted by the researchers found that the fracture occurs in the heat affected zone for lower traverse speeds while for higher values of traverse speed the fracture occurs at thermo-mechanically affected zone. Cavaliere et al. [32] studied the effect of welding and rotational speed on the mechanical properties of the weld joint. The welding parameters used for the analysis were significantly lower than the other authors. Therefore, the higher values of parameters used to conduct the study provided better results in terms of hardness, tensile and fracture strength, however, the lower values of parameters provided the better ductility. In contrary to that, Kim et al. [33] used much higher values of process parameters to perform the experiments. It was observed that the higher rotational speed and traverse speed increase the grain refinement. In another work, Cavaliere et al. [34] took a wide range of traverse speed in which rise of yield strength and grain size was observed upto an optimal level, on a further increase of parameters provided a decline in the same properties. The optimal parameter provided by the different researcher is shown in Table 2.1.The parameters like tool torque, temperature, frictional power significantly depend on the rotational

speed. Lombard et al. [35] worked on the effect of rotational speed on the weld quality in terms of mechanical properties of the joint based on the pitch i.e. welding to rotational speed ratio. Finding the optimum rotational speed and traverse speed is a challenge for different researchers. It depends on the tool geometry as well as on the weld material. Therefore, Balasubramanian [36] conducted a study to find the optimal parameters for different alloys of Aluminium. The optimal parameter for different alloys of Aluminium is given in Table 2.2. Based on these parameters different relationships were found between the material properties and the process parameter. The effect of process parameter on the corrosive behaviour of the weld zone was studied by M. Jariyaboon et al. [37]. It was observed that for low rotational speeds, the corrosion attack in the nugget region while for high rotational speeds, the corrosion attack in the HAZ region. The fatigue strength of friction stir welds was studied in comparison to the conventional welding methods. It was found that the fatigue strength was better in case of FSW samples than the weld samples obtained from TIG and MIG samples. According to Ericsson and Sandstrom [38], the fatigue strength is relatively independent of the weld speed. However, some authors denied the above conclusion and provided the optimum process parameter for fatigue and tensile strength of the weldment. The onion ring formed on the surface of the welding is dependent on the pitch of the welding i.e. rotations/traverse speed. Yong et al. [39] found that with increase in tool rotation the onion ring region increases and grain size decreases.

Table 2.1: The process parameters used by the authors to conduct their experiments.

Authors	Rotational Speed (rpm)	Traverse speed (mm/min)	Remarks
Elangovan and Balasubramanian [29]	1600	37, 76, 125	Highest tensile strength at 76 mm/min with square pin geometry
Lui et al. [30], Sakthivel et al. [31]	800, 1000	50- 200	Improvement in tensile property with an increase in traverse speed.
Cavaliere et al. [32]	500, 800, 1000	40, 56, 80	Low traverse speed and low rotation higher ductility. High tensile strength at higher tool rotation at 80 mm/ min traverse speed.
Kim et al. [33]	750-1750	250-1000	Increase in grain refinement at higher rotational speed.
Cavaliere et al. [34], Ericsson and Sandstrom [38]	1600	40-450	Grain size increase till 165 mm/min, yield strength till 115 then decreases; 115 mm/min provided best fatigue strength.
Lombard et al. [35]	300-600	85-185	Frictional power (2200 J/s) provided the best the optimum fatigue and tensile strength.

Table 2.2: Optimized FSW process parameters which provided defect-free weld [36].

Alloy	Tool rotational speed (rpm)	Traverse speed (mm/min)	Welding pitch (mm/rev)
AA1050	900	135	0.150
AA6061	1100	100	0.090
AA2024	1200	75	0.062
AA7039	1300	45	0.035
AA7075	1500	22	0.015

2.4 Tool geometries

The effects of tools were also investigated experimentally as well as numerically, as it is a significant factor in deciding the weld parameters. Tool geometries play a significant role in material movement in the weld zone. Every tool generates a different amount of heat and displaces the material uniquely. Many defects in the weld zone can be easily removed just by changing the tool geometry in the welding. Therefore, three different types of geometries were used by Krasnowski et al. [40] to study the microstructure and mechanical properties of the FSW joint. From the analysis, it was concluded that the triflute geometry produced the best tensile strength weld joint. Whereas, Colegrove and Shercliff [41] studied the trivex and triflute tool and concluded that trivex tool produces less vertical and traversing forces in comparison to triflute geometry. On the other hand, it was observed the scrolled probe performed better than the plain cylindrical shoulder [42]. However, according to Elangovan and Balasubramanian [29], the square pin profiled tool produced defect-free welds, irrespective of the traverse speeds. The analysis was performed using five different tool pin profiles (straight cylindrical, tapered cylindrical, threaded cylindrical, triangular and square) at three different traverse speeds. So, there is no common conclusion among the researchers on the FSW tool geometry.

The welds produced at a traverse speed of 0.76 mm/s showed superior tensile properties, irrespective of tool pin profiles by Elangovan and Balasubramanian [29]. The 18 mm shoulder size was suggested by the author to obtain the defect-free weld. In agreement to that, Arora et al. [43] suggested the same shoulder diameter for 1200 rpm tool rotation speed for best tensile properties in the weld zone. However, Fujii et al. [44] found that the microstructure was not affected by the tool geometry by performing welding with cylindrical, cylindrical threaded and triangular prism tool pin. The studies didn't limit to this, the D.G. Hattingh et al. [45] calculated the

welding forces for different tool geometries with the help of strain gauges fitted in the tool holder. The different pin geometries used in the analysis is shown in Figure 2.2. The effect of the shoulder on the microstructure was studied by Rodrigues et al. [46]. The scrolled shoulder produced smaller grain size in comparison to the flat shoulders. The different tool geometries used for different Aluminium alloys are shown in Table 2.3.

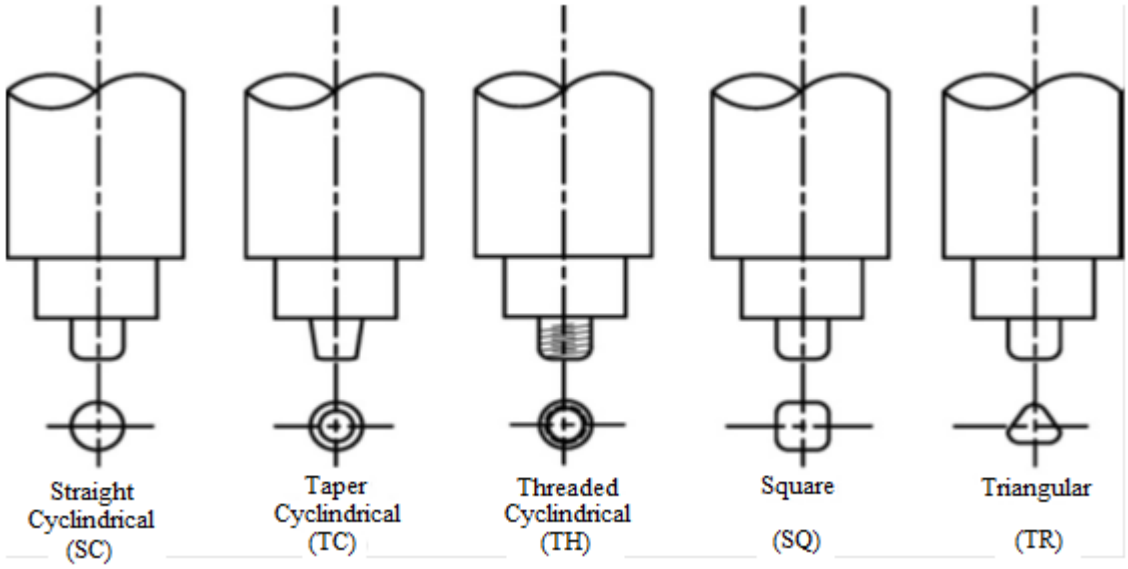

Figure 2.2: Different tool profiles used in Hattingh et al. [45].

Table 2.3: Tool geometries used for different alloys of Aluminium [47].

Tool shape and size	Tool material	Operating parameters	Workpiece material	Remarks
SS: Flat with scroll; SD: 10 mm; PL: 0–1.6 mm [48]	H13 steel	2000 rpm	6111-T4 Al alloy, 0.9 mm thick	Better quality with a pinless tool
PS: Triflute, Trivex [49]		394 and 457 rpm; 300–540 mm/min	7075-T7351, 6.35 mm thick	Weld UTS: 470–488 MPa
PS: Threaded [50]	1. MP159; 2. Dievar tool steel; 3. MP159 pin, H13 shoulder	190–457 rev min21 ; 0.3–1.4 mm rev21	7075-T7351; 6.35 mm, 16 mm thick	Peak joint efficiencies: 70–100%
SS: Concave; SD: 15 mm; PS: straight cylindrical, threaded, triangular; PL: 4.7, 6 mm [44]		600–1500 ; 25–1000 mm/min ; 3º tilt	Al alloys, 5 mm thick	Peak joint efficiency: 92%
SD: 10–20 mm, flat; PD: 3–8 mm; PL: 4.2 mm; PS: frustum and straight cylindrical [51]	Steel	1400 rpm; 80 mm/min	7020-T6 Al alloy, 4 mm thick	Joint efficiencies: y76%
SS: scroll, cavity, fillet; PD: 1.7 mm; PS: straight		1810 rpm ; 460 mm/min; 2º tilt	6082-T6 Al, 1.5 mm thick	

cylindrical; PL: 1.2 mm [52]				
SS: concave; SD: 26 mm; PD: 5.6 mm; PL: 5.9 mm; PS: threaded [53]		286–1150 rpm; 30–210 mm/min	6061-T6 Al, 6.3 mm thick	
SS:concave, convex, flat; SD: 12 mm; PD: 5 mm; PL: 1.6 mm [54]	H13 steel	1500 rpm; 20 mm/min;	5754 Al, 1.32 mm thick	
PD: 6 mm [55]	Tool steel	1000 rpm; 120 mm/min	A319 and A413 Al alloy, 6 mm thick	No property degradation in the weld metal
SS: concave; SD: 13 mm; PS: straight cylindrical, tapered circular; PL: 3.19 mm: PD: 5 mm [56]	High carbon steel	300–1620 rpm; 100–900 mm/min; 2.5º tilt	7020-T6 Al, 4 mm thick	
SD: 25.4 mm; PD: 5.2–7.6 mm; PL: 1.8–7.1 mm [57]	H13 steel	650 rpm; 150-200 mm/min ; 3º tilt	6061-T6 Al, 9.5 mm and 12.7 mm thick	

*SD: shoulder diameter; PL: pin length; PD: pin diameter; PS: pin shape; SS: shoulder shape

Other than simple tool geometries many advanced tools were also proposed by different authors such as non-moving shoulder, self-reacting tool etc. Many unconventional tool configuration provided by the authors such as unpinned tool [58] for welding Aluminium sheets. The bobbin tool FSW (BT-FSW) is an advanced tool used by the authors with a goal of generating higher heat with two shoulders [59]. Zhang et al. [60] studied the effect of traverse speed of Bobbin Tool FSW on a 6 mm 2A14-T6 Aluminium alloy plate using a triflat geometry and studied the grain structure at top bottom and middle layer. The top layer grain structure appears to be fine in comparison to the bottom due to higher heat dissipation from the top shoulder while with increasing traverse speed the grain size decreases [61]. The elliptical and equiaxed grained formation was found in the mid-surfaces for all the cases [62]. The traverse speed slightly affects the microhardness at the nugget zone in but through the thickness, not much variation was observed in the hardness values. The tensile strength and elongation appear to have an increasing trend upto a certain limit but it sharply decreases afterwards. The maximum values show 25% the reduction in tensile values of base metal in nugget zone. Esmaily et al. [63] compared conventional and BT-FSW process at two welding and rotational speeds. The study was conducted on a 10 mm thick AA6005-T6 plate. In BT-FSW a higher value of peak temperature was obtained due to the two shoulders. It was confirmed that the slower weld produces larger grain

size while the BT-FSW creates grain refinement and thus cause finer grain size in the SZ and thus produce a better hardness in the SZ.

2.5 Microstructure

The microstructure of welding provides much information about the quality of the weld. The mechanical properties are significantly affected by the microstructure of the welded joint. The process parameters like the tool rotational speed, traverse speed, tool selection, plunging force substantially affect the microstructure of the welding zone. Therefore, the quality of the weld directly depends on the process parameters used for performing the weld. The microstructural study revealed the nature of mixing the two mating material particles. Many authors mixed the foreign particles into the welding zone to study the distribution of the particle caused by the rotation of the tool. A homogeneous mixing of a foreign particle in the welding of AA2124 was found by Uzun [64]. Microstructure reveals the quality of the weld achieved with a particular process parameter and the tool geometry. According to the Rodrigues et al. [46], tool shoulder significantly affects the grain size of the weldment. The scrolled shoulder produces a smaller grain structure in comparison to plain shoulder structure. The mechanical properties of the weldments are dependent on the microstructure formed during the welding. The microstructure explains the failure of the tensile test specimens clearly for a healthy weld and a defected weld [65]. The study of microstructure helps in providing an optimum process parameter to obtain the best mechanical properties [66, 67]. The FSW can produce excellent electrochemical behaviour of the weldment with good corrosion resistance [68].

The microstructure studied by Murr et al. [69], [70] revealed the variations of the vortex and other swirl-like intercalations. The flow patterns of AA2024/6061 were also studied using a light microscopy. A complex vortex, whorl, and swirl feature characteristic were found in the mixing region shown in Figure2.3. The white regions represent the Aluminium whereas the Cu is represented by black. The flow patterns obtained were similar to extrusion. So tensile testing [71] were conducted on the FSW of 2XXX, 5XXX, 6XXX, and 7XXX series of Aluminium alloys.

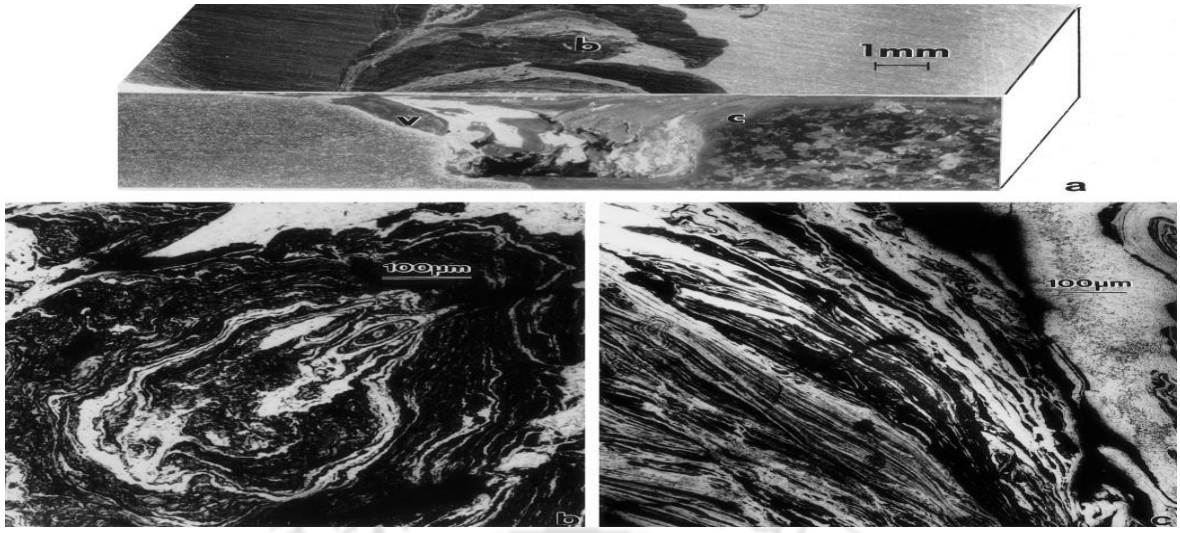

Figure 2.3: 6061 Aluminium/Copper friction-stir weld composite (R=650 rpm, T=1 mm/s). (b) An enlarged view of a region in the weld plane section marked (b) in (a) above showing intercalation swirl microstructure[69].

The Friction stir process not only used for welding purpose but finds many other applications related to microstructure refinement [72]. The Friction stir processing provides microstructure refinement, densification and homogeneity in the material. Therefore, the process is highly recommended in powder metallurgy of Aluminium alloy [73], metal matrix composite [74], and cast Aluminium alloys [75]. The desired mechanical properties in the processing zones are achieved by optimizing process parameters, tool design and cooling rates.

2.6 Defects

The defect formation in the FSW process is much different than the common fusion welding process. The common defects of the fusion welding processes are slag inclusion, porosity, cracks etc. which occurs due to the liquid state of the material in the weld region. However, in FSW the common defects are wormhole, tunnel defect, crack, kissing bond etc. which occur due to insufficient mixing of plasticized material. The process parameters have a significant role in the formation of a defect in FSW. The heat input provided in the weld joint depends on the rotational speed, traverse speed, tool shape and size, plunging depth as well as material to be weld. Based on the heat input few authors characterize the FSW into two main categories i.e. 'hot welding'(HW) and 'cold welding' (CW) [76]. This difference in microstructure conducted to a reduction in hardness around 15% in CW contrarily to the HW and a

reduction in elongation of 30% to 70% was observed for hot weld and cold welds respectively. The hot welds have shown better ductility and produced less hard weld zone in comparison to the clod welds [46]. The common flaws of cold welding FSW are kissing bonding, void formation, tunnel etc. However, the common defects caused by hot welding are flash formation, strength deterioration, cracking etc. The defect like insufficient penetration, joining are formed by operators errors or by choosing the wrong tool geometry. The defect formation and tool geometry used to weld the material are closely related to each other. Fujii et al. [44] observed that the AA1050 and AA6061 have low resistance to the deformation in comparison to AA5083. Three tool geometries were used for the experimentation. The welding performed by cylindrical tools on first two materials was better than the triangular prism. However, the triangular prism tool geometry was able to much better with AA5083 with a defect-free weld even at higher traverse speed.

The flashing of the material at the edge of the tool shoulder is another problem faced by many FSW operators. This is caused by higher heat input caused by the higher rotation of the tool. According to Li et al. [77], higher tool pressure provide a support to the tool rotation for flashing out the material on the retreating side. However, according to Keivani et al. [78], the pin of the tool plays a significant role in deciding the flashing out of the material. A high pin length causes the material extrusion toward the tool shoulder and result in flashing out of the soft material. However, a very high pin length cause the extrusion along the pin length and flashing out of the material occur at the root of the weld.

The tunnel defect is generally formed at higher traverse speeds. At higher traverse speeds, the insufficient mixing and less fluidity of the plasticized material occur in the weld region due to low heat input [79]. So, this leads to the formation of the tunnel defect in the weld region. For the increase of fluidity [80] of the material in the weld region, the reduction in the traverse speed is recommended [81]. According to Zhao et al. [82], the tunnel area formed in the weld zone increases with the traverse speed. Therefore, a larger tool shoulder is recommended to increase the heat input in the weld zone. The other defect form by low heat input is the ‘kissing bond’ which occur due to insufficient mixing of the two mating plates [83]. These kissing bonds become the source of crack formation in the weld region on the application of load. Thus, the fatigue and tensile strength of the weldment decrease drastically in the presence of

kissing bond defect [84]. The kissing bond was caused due to improper mixing of the material during the welding.

A void is a most common defect noticed by the authors, occurs on the advancing side of the weld zone at high traverse speed. A small groove defect is noted at 200 mm/min traverse speed [30], however bigger wormholes were noticed by Crawford et al. [85]. The most of the authors reported a defect on the advancing side. In contrary to that, the study conducted by Elangovan and Balasubramanian [29] reported defects on the retreating side. Sometimes, the overlapping passes of the FSW help in eliminating the defect. The overlapping doesn't change the microstructure much but alters the mechanical properties of the joint. An insignificant effect on the microstructure of the weld and a marginal improvement in the hardness and tensile strength of the FSW joint was achieved by Leal and Loureiro [86] with overlapping passes. The overlapping passes are a very effective way to eliminate the defects. However, some authors claim that an offset pass provides better repair quality than the symmetrical repair pass [87]. It is still unclear how much offset should be provided to obtain the best mechanical properties of the joint.

2.7 Material flow behaviour

The material flow of FSW is a complex phenomenon which depends on the tool geometry, process parameters and the welding material. The understanding of material flow patterns of the welding provides significant information in selecting a proper tool geometry and process parameter for a selected material. Different authors used different approache to visualize the material flow of the welding. One approach was the tracer technique in which foreign particles were injected in the weld zone before the weld and position were traced after the welding. The other approach was dissimilar material joining by FSW. Different tracer techniques were used by the researchers to study the material flow behaviour of the Aluminium alloy under the tool geometry.

Reynold [88] used a marker insert technique to study the material flow in the welding zone. The material used as the marker was AA5454-H32 in the welding of AA2195-T8 under threaded pin geometry. It was found that the material flow was not symmetrical around the weld line. The markers material was moved backwards during the welding with a distance equivalent to the pin diameter. The material was pushed

downward on the advancing side while on the retreating side it was moved upward. According to author [88], the stir action in the material was dominated in the top region around the tool shoulder. However, it was found that the transportation of the material across the centerline depend on the pin diameter of the tool. Guerra et al. [89] used a Cu strip as a marker in the weld zone for studying the material flow. It was observed that the front advancing side material was sloughed by the tool shoulder in the form of an arc shape in the weld zone. However, the retreating side material was extruded between the base material and the tool wall. A similar method was used by the Schmidt et al. [90] i.e. Cu strip was placed between the two welding plates and traced it with the X-ray and computer tomography (CT). However, Morisada et al. [91] used tungsten as a tracer material to analyze material flow through X-ray technique. The image produced in the procedure provided the information regarding the sticking condition material flow. The X-ray technique proved vital for tracing most of the materials like Cu as well as steel [92].

Colligan [93] used steel shot tracer technique to investigate the material flow. As the name suggested, the spherical steel balls were placed in the path of the welding tool and after the weld, the steel structure was traced with the help of radiography. In order to get the real-time movement of the tracer material particles, a "stop action" technique was used. In stop action technique the tool was stopped suddenly in the middle of welding and reversed the direction of the weld which creates a keyhole in that position. Later, that section of the weld was taken and plates were analyzed to obtain the stir action of the tool on the material. Two types of behaviour were observed in the weld zone i.e. chaotical and continuous distribution. In chaotical distribution, the steel material was scattered all around the weld zone behind the tool while in continuous distribution a continuous line of steel was obtained in the weld zone. Kumar et al. [94] used Particle image velocimetry (PIV) technique in which micro-spherical glass tracers in a transparent visco-plastic material was utilized to understand the material flow. Many authors believe that the pin geometry affects the material flow but few authors denied the above fact. Lorrain et al. [56] found the material flow with the unthreaded tool has the same features as the material flow using classical threaded tools. Though these studies produce a lot of understanding about the material flow behaviour of the material under the FSW tool, the marker material particles have different mechanical properties than the base

material in terms of viscosity, and density. So, the information provided by the authors still need better authentication.

2.8 Dissimilar friction stir welding

In the last decade, the substantial amounts of research were conducted on dissimilar metal FSW. Prior to this, the researchers were primarily confined to similar metal joining. The Dissimilar metal FSW process lacks the knowledge of weld quality obtained in terms of microstructure, intermetallic compounds, defects and mechanical properties of the joints. In the advanced world, many applications require dissimilar metal joining such as mild steel-Cu, Al-Cu, Al-Ti etc. Joining dissimilar metals having different mechanical properties is a tedious job. Many authors reported that FSW is capable of joining the dissimilar materials. The tool and machine require for Al-Cu are much cheaper in comparison to the equipment required to join harder materials. Therefore, huge experiments were reported on Al-Cu to gain sufficient knowledge on dissimilar metal FSW. The major problems associated with Al-Cu FSW process are common with other dissimilar material FSW.

The Al and Cu have excellent electrical and mechanical properties thus the joining of these two metals found many applications in sectors like power generation, electronic and transportation [95], [96]. Though the research started on the dissimilar metal joining in the late 90's [69], the extensive experimentations begin after 2006 [97]. The effect of process parameter like rotational, traverse speed, material position, tool geometry, tool offset etc. on the microstructure formation in the weld zone were reported in many articles. Two types of approaches were used by the authors for studying the influence of rotational and traverse speed. One in which a single parameter was varied with the remaining parameters constant, whereas in other approach both the parameters were varied simultaneously. Xue et al. [98] used the first approach to study the effect of rotational and traverse speed on microstructure. Liu et al. [99] followed the same approach to study welding parameter on the microstructure. Both of them concluded that the material interaction increases with rotational speed keeping the transverse speed constant. However, a decrease in traverse speed provided the same conclusion at a constant rotational speed. Abdollah-Zadeh et al. [100] and Barekatain et al. [101] agreed to the same conclusions by performing the

experiments in a similar approach. However, discords are found in case of the effect of process parameter on the surface finish of the weld joint among all authors. Higher formation of the brittle intermetallic compound at lower values whereas insufficient material mixing on higher values of traverse speeds were observed by Muthu and Jayabalan [102]. The authors like Galvão et al. [103] and Bisadi et al. [104] used the second approach to study the influence of rotational and traverse speed on the microstructure. The Galvão used rotational to traverse speed (ω/v) ratio to determine the weld quality and found that the material interaction increases with ratio while the Bisadi used ω^2/v ratio to decide that the higher values provide the better surface finish and the best material interaction. The higher heat input values provide better material mixing which occurs at higher rotational and lower traverse speed.

Some research articles placed Cu on the advancing side and some placed Al on the advancing side. Though the material welding side significantly affects the welding [97], there is no consensus among the authors regarding the material placement. Galvão et al. [105] noticed that healthier welds were obtained by placing Cu on the advancing side. A similar trend was observed by Xue et al. [98] and Liu et al. [99] and found inconsistent weld was obtained by placing Al on the advancing side. In contrary to that, Tan et al. [106], Kahl and Osikowicz [107], and Ouyang et al. [108] obtained a sound weld on placing Al on the advancing side.

Tool offset plays a significant role in achieving a proper weld. Many authors obtained a defect-free weld by offsetting the tool on the Al side. However, the amount of offsetting is not fixed; different authors provided different values of offset. Okamura and Aota [109] obtained better surface finish and less defective weld by completely shifting the tool towards the Al side. In agreement with that, Genevois et al. [110] achieved better surface finishing in joining AA1050 with pure Cu by doing the same. In the above cases, the welding obtained was not considered as good as the joining occurred by friction stirs diffusion bonding and many discontinuities were found in the microstructure. Avettand-Fenoël et al. [111] concluded that the welding conditions became worse on shifting the tool towards the interface. Similarly, Xue et al. [98] found improvement in surface finish and reduction in brittle intermetallic compounds formation by offsetting the tool on the Aluminium side.

2.9 Analytical and numerical methods

The analytical methods provide better insight of the process by decomposing the complex process into simpler understandable equations having certain assumptions. The above said decomposing process often used to analyze one or two aspects of the process completely to make the problem simpler to understand. The information gathered through these methods lead to a reduction in the number of experiments. The numerical methods like FEM improve the research productivity as experiments are costly and time-consuming.

The analytical study and numerical simulation is an important method for the understanding the mechanisms of the FSW process. It provides insights into the welding characteristics both qualitative and quantitative without performing costly experiments. The numerical methods (in particular FEM and FVM) are more flexible in treating complex geometries and boundary conditions, with respect to their analytical counterparts. The FSW simulation typically involves studies of the rotation and traverse speed on the temperature distribution and residual stresses in the work-piece, etc. This simulation is a complex task since it involves the interaction of thermal, mechanical and metallurgical phenomena. Different decoupled models were proposed by the authors with a simplified thermal and material flow model in different software. Vilaca et al. [112] determined the thermal history of 2D and 3D geometry and studied the heat flow by conduction mechanism inside the plate domain with the help of iSTIR model. The study was conducted for similar and dissimilar materials which were verified with the experimental data. The thermal histories were recorded with the help of thermocouples during the experiments. The analytical analysis was performed by recording the thermal history distribution patterns. The mathematical equations were fitted in the relation between the temperature and distance from the centerline by Hwang et al. [113]. The temperature distribution equations obtained were not general i.e. they belong to a specific case. Kim et al. [114] worked on an FVM code, utilizing full sticking condition, to study the effect of parameters on thermal history distribution whereas, Chen and Kovacevic [115] proposed a 3D finite element model to study the effect of process parameters. More different approaches were used to optimize the process parameters. Vilaca et al. [116] suggested an inverse engineering approach by using the analytical thermal code iSTIR to establish the

correlation between the parameter of FSW and the properties of the resulting joints. Hamilton et al. [117] used a new energy based slip factor in thermal modelling of FSW. Further, the plasticity models were used by Hamilton et al. [118] and Williamson [119], [120] to incorporate the heat generation with the plastic deformation of the material. It was found that the contribution of heat generation with plastic deformation was more at lower rotational speed. Kovacevic [121], [115] and Aval et al. [122] worked on the 3D moving the coordinate model to study the transient thermal history of the FSW process. The effect of process parameter on temperature distribution on the material plate was studied and validated experimentally. The studies are further extended to study residual stresses by Buffa [123], Kovacevic [115]. The minimisation of residual stress was achieved by optimizing process parameter. With the involvement of many factors in the thermal history distribution, therefore obtaining a general temperature distribution is a big challenge. Zhang [124] confirmed that the peak temperature and welding flash increases with rotational speed. It was found that longitudinal residual stresses were much higher than the transverse stresses and the simultaneous increase in rotating and translating speed leads to an increase of residual stress. The analysis conducted for studying the structural aspect of the welding is significantly affected by the boundary conditions [125]. The unconventional tools like bobbin tool were studied by Hilgert et al. [126] with the Arbitrary Lagrangian Eulerian (ALE) approach. Similarly, Assidi et al. [127] formulated a 3D numerical simulation in FORGE3 F.E. software using Notron's and coulomb's model with ALE formulation. The formulation achieved was best calibrated with coulomb's model using $\mu = 0.3$. So, selecting the right boundary condition for any analysis is very important.

Different models were proposed to study material flow by the authors. The authors like Feulvarch et al. [128], Chiumenti et al. [129], proposed a simple and robust moving mesh technique for finite element simulation to study material flow and heat transfer in the weld material with different kinds of tool pin geometry. The adaptive mesh is based on the ALE technique. This method incorporated momentum and mass conservation equations for flow problems, while energy balance equations are used for thermal analysis. However, Dialami et al. [130] used the same mesh approach and studied the material flow with particle tracer method. The predicted material flow was compared with the flow obtained with material insert technique. Zhang et al. [131]

used finite element package ABAQUS to perform 3D material flow modelling of FSW. The swirls motions were reported on the advancing side in the material flow of material. Similar vortex formations were also reported by Jacquin et al. [132], in 3D thermo-mechanical model based on Eulerian approach proposed by Heurtier et al. [133]. Partial sliding and partial sticking with non-linear material properties [134] were considered to perform the FSW simulation. However, Schmidt and Hattel [135] worked on a completely thermal-mechanical coupled model in Computational fluid dynamics (CFD) software packages. However, Zhang et al. [136] used a temperature-dependent elastic visco-plastic model for the simulation of the FSW process. The non-elastic response of the rate-dependent material in the large deformation problems was calculated by using the closest point algorithm. Chuan et al. [137] studied the plastic material flow by embedding the Copper sheets as marker material in the weld path 2024 Aluminium alloy plates. A three-dimensional model was developed to conduct the numerical simulation of the temperature profile and plastic material flow in FSW. Mendez et al. [138] coupled the plastic deformation and the heat transfer and derived the expressions for the thickness of the shear layer, maximum temperature and volumetric heat generation in the process.

Gemme et al. [139] studied the material behaviour in the dwell phase of FSW with a visco-plastic model based on Norton Hoff law. The tool geometry is one parameter that affect material flow significantly. The geometries were created in the 3D models to study the friction stir spot welding by Hirasawa et al. [140]. The analysis predicted that a triangular pin with a concave shoulder is the preferred tool geometry for friction stir spot welding.

2.10 Summary

The researchers studied FSW of various similar and dissimilar materials and optimize its process parameters. There was no consensus among the author regarding process parameter to be used but an optimal range of rotational and traverse speed can be obtained for a healthy weld from the above discussion. Various tool geometries were studied by different authors. Since it is an evolving field, many unconventional tools were proposed which specifies a special task. Each tool had certain set of a process parameters in which it performs the best. From the above discussion, it came into

focus that the process parameter and tool selection is highly sensitive to the type of materials and its thickness to be welded. The flow pattern study needs more exploration as very less literature is available. Most authors used foreign particles as a tracer material in welding which differs in mechanical properties of parent material. So, the experimental results produced by the authors are insufficient to make any conclusions. When it comes to dissimilar material, there are lots of uncertainties regarding the process parameter, material placement and the tool offset. Different authors produced different values of offset and process parameter. So, the study regarding the dissimilar material FSW is inevitable.

2.11 Gaps in literature

From the above literature study the following gaps are observed:

- Numerical simulation and analytical methods are mainly carried on Aluminium and Aluminium alloys i.e. similar metals. No literature is available for simulation of dissimilar material.
- So far no vigorous work is conducted in simulation therefore; it doesn't provide sufficient understanding of material flow during the welding.
- No comparative studies between different proposed models are found in the literature like the turbulent and laminar models.
- Effect of tool geometries on the material flow behaviour of the material is absent in the literature.
- The experimental study has been conducted on the dissimilar metals but the harder material and lighter material positions have not specified some authors says harder material to be placed on advancing side while some say lighter material to be placed on advancing side.
- Tool position or tool eccentricity is an important aspect for the welding of dissimilar metal which needs to be focused as the weld quality and material flow depends on the position of the tool.
- Flow behaviour in the defected plate is not found in the literature.

2.12 The scope of the thesis

The current thesis is primarily focused on the study of the material flow of similar and dissimilar material FSW. The initial work provided the heat generation formulation caused by friction and plastic deformation. The formulation can be utilized to calculate the heat flux for any numerical model. Further different material flow models are presented based on the complexity of the model. Each model provides the significance of each assumption used in the model. Further, the material flow for different tool geometries is provided. These studies provide the insight of material movement under the tool pin geometries used to perform the FSW. The information gathered from these models can be utilized to select the right pin geometry for the FSW process. The significance of process parameter on the material is also understood as it directly affects the heat input in the material. The study is conducted for AA6061 and provides the knowledge of temperature distribution on both advancing and retarding side. The temperature distribution in turns changes the material properties which are utilized to calculate the properties like the viscosity of the weld material.

The second part of the thesis deals with the material flow of dissimilar material which is based on a novel model. The model utilized a volume of fluid approach and provides a great insight into the material flow of Aluminium and Copper FSW. The thermal profiles of the model are found to be in good agreement with the experiments. So, this model can be utilized to study other dissimilar materials. These material flow models can be utilized to study the material flow for the defect formation in the FSW process.

Chapter 3

Model Methodology

3.1 Introduction

This chapter includes all the methodology used to fulfil the objectives stated in the first chapter. It provides the sequence in which work is performed based on each objective. The theory adopted in the models and the setups used for experiments are detailed below. The first section of the chapter includes the formulation of heat generation in FSW. The second section includes the details of 3D finite element model used to conduct the transient thermal analysis of FSW of AA6061. The above section is followed by the detailed CFD model to study the material flow behaviour of FSW. The later sections explain the model used to study the material flow behaviour of the dissimilar material and the final section explains the setup used to conduct the experiments and its details.

3.2 Heat generation in FSW tool

Heat generation formulations of friction stir welding i.e.

1) Flat Cylindrical shoulder with cylindrical probe.
2) Flat Cylindrical shoulder with conical probe.

3.2.1 Heat generation due to flat cylindrical shoulder with cylindrical probe

Let us consider a cylindrical tool whose shoulder radius is R and radius of its probe is r_p whereas considering the height of the probe as l which as shown in Figure 3.1. It is considered that the angular speed of the tool is ω and acted upon a plunging force P_n which generate a pressure P on the shoulder surface, due to this pressure the total heat generation is calculated as follows.

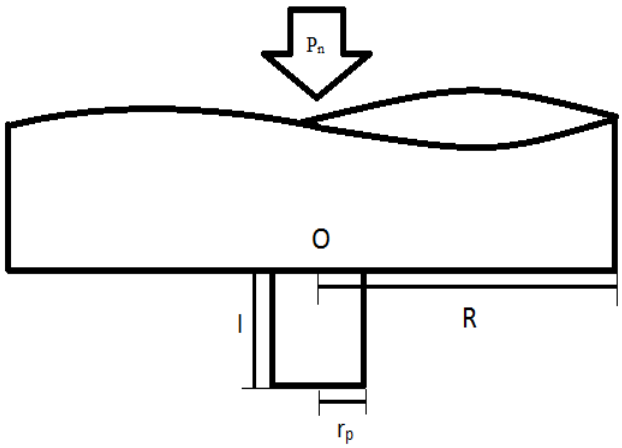

Figure 3.1: Schematic diagram of flat cylindrical FSW tool.

3.2.1.1 Heat generation due to sliding in the shoulder

There are two components of heat generation in shoulder i.e.

(i) Heat generation due to vertical pressure

(ii) Heat generation due to travelling of shoulder

Heat generation due to vertical pressure is explained below.

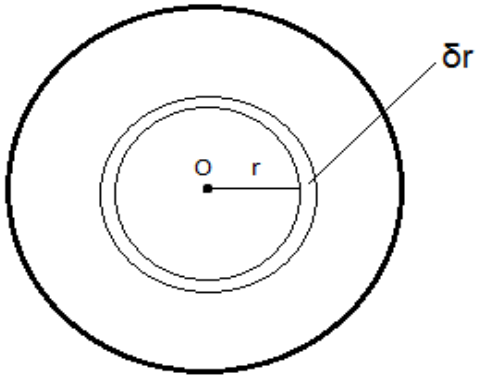

Figure 3.2: Small elementary area of shoulder.

Heat generation due to vertical pressure

Area responsible for heat generation of the shoulder is shown in Figure 3.2. Taking an elemental ring of thickness δr which is at r distance from the centre (O) of the area.

Therefore the area of the elemental ring is given by Eq. (3.1),

$$\delta A = 2\pi r \delta r \tag{3.1}$$

Normal force acting due to this elemental ring,

$$\delta N = P.2\pi \mathrm{r}\delta \mathrm{r} \tag{3.2}$$

Let us take the frictional coefficient between the tool and workpiece to be *f*.

Therefore, Frictional force,

$$\delta F = 2fP\pi \mathrm{r}\delta \mathrm{r} \tag{3.3}$$

Heat generation due to elemental ring,

$$\delta Q_{s1} = 2fP\pi \mathrm{r}\delta \mathrm{r}.\,\omega \mathrm{r} \tag{3.4}$$

Integrating both sides of Eq. (3.4),

i.e. $$Q_{s1} = 2\pi f\omega P \int_{r_p}^{R} r^2 \delta r$$

Or $$Q_{s1} = \frac{2}{3}\pi f\omega P\,(R^3 - r_p^3) \tag{3.5}$$

Heat generation due to travelling of tool shoulder

Let us consider the depression in the welding area is h_1 and the tool moves with a velocity of *v*, however, the yield strength of the material at 80% of the melting point temperature is S_{ys}^*.

Since the tool is moving forward, therefore, the force acts upon the front half curved surface area of the shoulder.

Area responsible for heat generation is given by Eq. (3.6),

$$A = \pi \mathrm{R}h_1 \tag{3.6}$$

Frictional force for heat generation

$$F = f\pi S_{ys}^* R h_1 \tag{3.7}$$

Heat generation

$$Q_{s2} = f\pi S_{ys}^{*} R h_1 v \tag{3.8}$$

Total heat generation

$$Q_s = Q_{s1} + Q_{s2}$$

$$Q_s = \frac{2}{3}\pi f \omega P \left(R^3 - r_p^3\right) + f\pi S_{ys}^{*} R h_1 v \tag{3.9}$$

3.2.1.2 Heat generation in cylindrical probe

There are two important part of Probe which is responsible for heat generation i.e.

i) Probe tip surface and

ii) Probe side surface

The details of heat generation both on probe tip and side surface are described below

Heat generation due to vertical pressure at probe tip

Heat generation formulation for probe tip having radius r_p can be derived similarly from Eq. (3.5),

i.e. $$Q_{p1} = \frac{2}{3}\pi f \omega P r_p^3 \tag{3.10}$$

Heat generation due to the rotational movement of the probe

Force acting on the probe on its surface can be obtained as,

$$F_p = f S_{ys}^{*} 2\pi r_p l \tag{3.11}$$

Heat generation through the curved surface area,

$$Q_{p2} = 2f\pi S_{ys}^{*} \omega r_p^2 l \tag{3.12}$$

Heat generation due to travelling of the probe

Only half of the curved surface area is responsible for heat generation during the travelling of probe.

i.e. $$A = \pi r l$$

Therefore, force acting on the probe due to travelling on workpiece.

$$F_p = fS_{ys}^{*}\pi r_p l \tag{3.13}$$

Therefore heat generation,

$$Q_{p3} = fS_{ys}^{*}\pi r_p l v \tag{3.14}$$

The total heat generation at the probe can be calculated by adding Eqs. (3.10), (3.12) and (3.14).

i.e. $$Q_p = Q_1 + Q_2 + Q_3$$

$$Q_p = \frac{2}{3}\pi f\omega P r_p^3 + 2f\pi S_{ys}^{*}\omega r_p^2 l + fS_{ys}^{*}\pi r_p l v \tag{3.15}$$

Therefore total heat generation due to friction in Flat Cylindrical shoulder with cylindrical probe is

$$Q_{sliding} = Q_s + Q_p$$

i.e. $$Q_{sliding} = \frac{2}{3}\pi f\omega P\,(R^3 - r^3) + f\pi S_{ys}^{*} R h_1 v + \frac{2}{3}\pi f\omega P r_p^3 + 2f\pi S_{ys}^{*}\omega r_p^2 l + fS_{ys}^{*}\pi r_p l v \tag{3.16}$$

3.2.2 Heat generation in flat cylindrical shoulder with conical probe

Let us consider a flat cylindrical tool whose shoulder radius is *R* and having a conical probe which is having base radius of r_p and tip radius of r_b, height of the probe is taken as *l* as in previous case. It is considered that it is rotating with an angular velocity of ω and acted upon a plunging force P_n which generate a pressure *P* on the shoulder surface as shown in Figure 3.3, due to this pressure the total heat generation is calculated as follows.

3.2.2.1 Heat generation in shoulder

As explained in the article 3.2.1 the total heat generation in shoulder is given by Eq. (3.9)

i.e. $$Q_s = \frac{2}{3}\pi f\omega P\left(R^3 - r_p^3\right) + f\pi S_{ys}^{*} R h_1 v$$

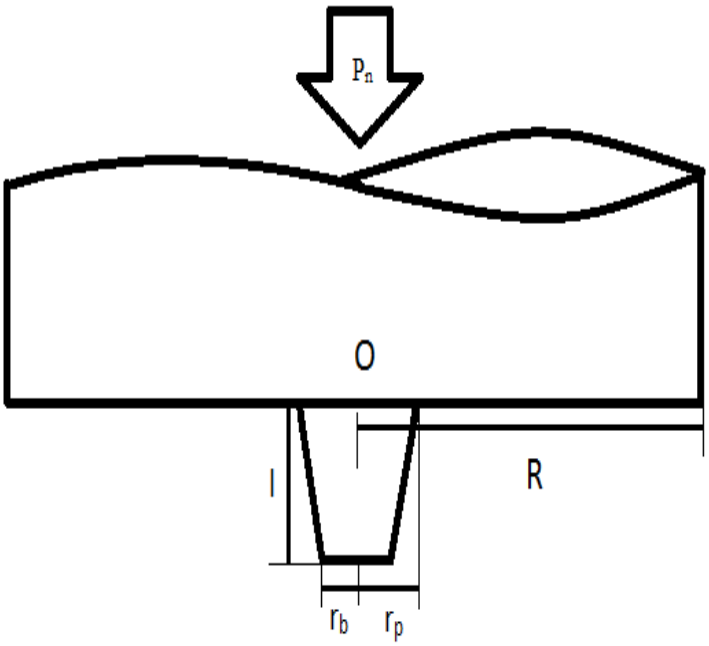

Figure 3.3: Schematic diagram of flat cylindrical shoulder and conical probe.

3.2.2.2 Heat generation in conical probe

There are two important part of Probe which are responsible for heat generation (as explained in 3.2.2) i.e.

i) Probe tip surface and

ii) Probe side surface

The details of heat generation both on probe tip and side surface are described below

Heat generation due to base

Heat generation due to base can be derived Similar to Eq. (3.5),

i.e. $$Q_{p1} = \frac{2}{3}\pi f \omega P r_b^3 \quad (3.17)$$

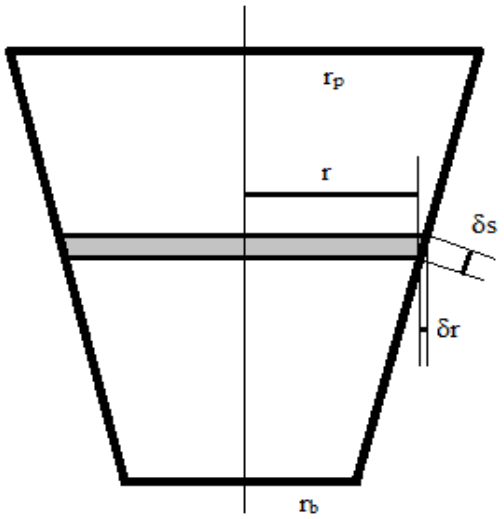

Figure 3.4: Small elemental area of probe.

Heat generation due to rotational movement of the probe

Taking elemental ring on the curved surface area of the probe at a distance *r* from the centre and thickness *δr* and slant thickness *δs* as shown in Figure 3.4.

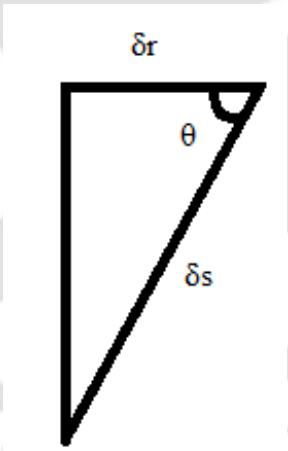

Figure 3.5: Small elemental triangle.

$$\cos\theta = \frac{(r_p - r_b)}{s} \tag{3.18}$$

Therefore elemental area of heat generation,

$$\delta A = 2\pi r \delta s \tag{3.19}$$

Frictional heat generation can be obtained as,

$$\delta F_p = f S^*_{ys}.2\pi r \delta s \tag{3.20}$$

Therefore heat generation,

$$\delta Q_{p2} = 2f\omega S^*_{ys}\pi r^2 \delta s \tag{3.21}$$

From Figure 3.5,

$$\cos\theta = \frac{\delta r}{\delta s}$$

$$\delta s = \frac{\delta r}{\cos\theta} \tag{3.22}$$

By Pythagoras theorem,

$$s = \sqrt{(r_p - r_b)^2 + l^2} \tag{3.23}$$

From Eqs. (3.22) & (3.21)

$$\delta Q_{p2} = 2\frac{f\pi\omega}{\cos\theta} S^*_{ys} r^2 \delta r$$

Integrating both sides,

$$Q_{p2} = 2\frac{f\pi\omega}{\cos\theta} S^*_{ys} \int_{r_b}^{r_p} r^2 \delta r$$

$$Q_{p2} = \frac{2}{3}\frac{f\pi\omega}{\cos\theta} S^*_{ys}(r_p^3 - r_b^3)$$

Using Eqs. (3.18) & (3.23)

$$Q_{p2} = \frac{2}{3}\pi f\omega S^*_{ys}(r_p^2 + r_p r_b + r_b^2)\sqrt{(r_p - r_b)^2 + l^2} \tag{3.24}$$

Heat generation due to travelling of the probe

Let us consider that probe is moving with a velocity of v, taking yield strength of the workpiece at 80% of its melting temperature S^*_{ys}. In this heat generation we only consider half of the curved surface area which is responsible for heat generation during the travelling of workpiece.

$$\delta A = \pi r \delta s \tag{3.25}$$

Therefore, force acting on the probe due to travelling of workpiece.

$$\delta F_p = f S_{ys}^* \pi r \delta s \tag{3.26}$$

Heat generation,

$$\delta Q_{p3} = f S_{ys}^* \pi r \delta s v \tag{3.27}$$

From Eq. (3.22)

$$\delta Q_{p3} = f S_{ys}^* \pi r \frac{\delta r}{\cos\theta} v$$

Integrating both sides

$$Q_{p3} = f S_{ys}^* \frac{\pi}{\cos\theta} v \int_{r_b}^{r_p} r \delta r$$

$$Q_{p3} = f S_{ys}^* \frac{\pi}{2\cos\theta} v (r_p^2 - r_b^2)$$

Now using Eqs. (3.18) & (3.23)

we get, $$Q_{p3} = \frac{f}{2} \pi S_{ys}^* v (r_p + r_b) \sqrt{(r_p - r_b)^2 + l^2} \tag{3.28}$$

Total heat generation in probe

$$Q_p = Q_{p1} + Q_{p2} + Q_{p3}$$

$$Q_p = \frac{2}{3} f \pi \omega P r_b^3 + \left\{ \frac{2}{3} f \pi \omega S_{ys}^* \left(r_p^2 + r_p r_b + r_b^2\right) + \frac{f}{2} \pi S_{ys}^* v (r_p + r_b) \right\} \sqrt{(r_p - r_b)^2 + l^2} \tag{3.29}$$

Therefore total heat generation in flat cylindrical shoulder with conical probe is

$$Q_{sliding} = Q_s + Q_p$$

i.e $$Q_{sliding} = \frac{2}{3} \pi f \omega P \left(R^3 - r_p^3\right) + f \pi S_{ys}^* R h_1 v + \frac{2}{3} f \pi \omega P r_b^3 + \left\{ \frac{2}{3} f \pi \omega S_{ys}^* \left(r_p^2 + r_p r_b + r_b^2\right) + \frac{f}{2} \pi S_{ys}^* v (r_p + r_b) \right\} \sqrt{(r_p - r_b)^2 + l^2} \tag{3.30}$$

3.3 Heat generation due to plastic deformation

There are two sources of heat generation in the FSW process. One is friction heat generation while the other is plastic heat generation. The friction heat generation is discussed in the earlier section whereas this section covers the plastic heat generation. The plastic heat generation is caused by the deformation of the material inside the plate.

3.3.1 Heat generation in flat cylindrical shoulder and cylindrical probe

It is considered that the sticking velocity of the tool is ω and τ be the shear strength of the workpiece and τ^* be the shear strength of the material at 80% of its melting point temperature, due to this shearing stress between the layers the total heat generation is calculated as follows.

3.3.1.1 Heat generation in shoulder

Taking an elemental ring of thickness δr which is at r distance from the centre O

Therefore the area of the elemental ring,

$$\delta A = 2\pi r \delta r \tag{3.31}$$

Force acting in elemental ring,

$$\delta F = \tau^* . 2\pi \mathrm{r} \delta \mathrm{r} \tag{3.32}$$

Heat generation due to elemental ring,

$$\delta Q_s = 2\tau^* \pi \mathrm{r} \delta \mathrm{r} . \omega \mathrm{r} \tag{3.33}$$

Integrating both sides of Eq. (3.33),

i.e. $$Q_S = 2\pi\tau^*\omega \int_{r_p}^{R} r^2 \delta r$$

Or $$Q_S = \frac{2}{3}\pi\omega\tau^* (R^3 - r_p^3) \tag{3.34}$$

3.3.1.2 Heat generation in probe

There are two important part of Probe which is responsible for heat generation i.e.

i) Probe tip surface and

ii) Probe side surface

The details of heat generation both on probe tip and side surface are described below.

Heat generation in cylindrical probe tip

Heat generation in cylindrical probe tip can be derived similarly to Eq. (3.34),

$$Q_{p1} = \frac{2}{3}\pi\omega\tau^* r_p^3 \tag{3.35}$$

Heat generation due to the rotational movement of the probe

Force acting on the probe on its surface,

$$F_p = \tau^* . 2\pi r_p l \tag{3.36}$$

Heat generation through the curved surface area,

$$Q_{p2} = 2\pi\tau^*\omega r_p^2 l \tag{3.37}$$

Total heat generation in probe,

$$Q_p = Q_{p1} + Q_{p2}$$

i.e. $$Q_p = \frac{2}{3}\pi\omega\tau^* r_p^3 + 2\pi\tau^*\omega r_p^2 l$$

Therefore total heat generation in Flat Cylindrical shoulder with cylindrical probe is

$$Q_{sticking} = Q_s + Q_p$$

i.e. $$Q_{sticking} = \frac{2}{3}\pi\omega\tau^* \left(R^3 - r_p^3\right) + \frac{2}{3}\pi\omega\tau^* r_p^3 + 2\pi\tau^*\omega r_p^2 l \tag{3.38}$$

3.3.2 Heat generation in flat cylindrical shoulder with conical probe

It is considered that sticking angular velocity is ω and τ^* be the shear strength of the material at 80% of its melting point temperature, due to this shearing stress between the layers the total heat generation is calculated as follows.

3.3.2.1 Heat generation in shoulder

The total heat generation in shoulder is given by Eq. (3.34)

i.e. $$Q_s = \frac{2}{3}\pi\omega\tau^* \left(R^3 - r_p^3\right)$$

3.3.2.2 Heat generation in conical probe

There are two important part of Probe which is responsible for heat generation i.e.

i) Probe tip surface and

ii) Probe side surface

The details of heat generation both on probe tip and side surface are described below.

Heat generation due to base

Heat generation due to probe base can be derived similarly to Eq. (3.35),

$$Q_{p1} = \frac{2}{3}\pi\omega\tau^* r_b^3 \quad (3.39)$$

Heat generation due to rotational movement of the probe

Taking elemental ring on the curved surface area of the probe at a distance r from the centre and thickness δr and slant thickness δs

$$\cos\theta = \frac{(r_p - r_b)}{s} \quad (3.40)$$

Taking elemental area of heat generation,

$$\delta A = 2\pi r \delta s \quad (3.41)$$

Frictional heat generation,

$$\delta F_p = \tau^* . 2\pi r \delta s \tag{3.42}$$

Heat generation,

$$\delta Q_2 = 2\omega\tau^*\pi r^2 \delta s \tag{3.43}$$

From Figure 3.5,

$$\cos\theta = \frac{\delta r}{\delta s}$$

$$\delta s = \frac{\delta r}{\cos\theta} \tag{3.44}$$

whereas,

$$s = \sqrt{(r_p - r_b)^2 + l^2} \tag{3.45}$$

From Eqs. (3.43) and (3.44)

$$\delta Q_{p2} = 2\frac{\pi\omega}{\cos\theta}\tau^* r^2 \delta r \tag{3.46}$$

Integrating both sides,

$$Q_{p2} = 2\frac{\pi\omega}{\cos\theta}\tau^* \int_{r_b}^{r_p} r^2 \delta r$$

$$Q_{p2} = \frac{2}{3}\frac{\pi\omega}{\cos\theta}\tau^*(r_p^3 - r_b^3) \tag{3.47}$$

Using Eqs. (3.45) and (3.47)

$$Q_{p2} = \frac{2}{3}\pi\omega\tau^*(r_p^2 + r_p r_b + r_b^2)\sqrt{(r_p - r_b)^2 + l^2} \tag{3.48}$$

Total heat generation in probe

$$Q_p = Q_{p1} + Q_{p2}$$

$$Q_p = \frac{2}{3}\pi\omega\tau^* r_b^3 + \left\{\frac{2}{3}\pi\omega\tau^*\left(r_p^2 + r_p r_b + r_b^2\right)\right\}\sqrt{(r_p - r_b)^2 + l^2} \tag{3.49}$$

Therefore total heat generation in Flat cylindrical shoulder with conical probe is

$$Q_{sticking} = Q_s + Q_p$$

i.e $$Q_{sticking} = \frac{2}{3}\pi\omega\tau^*\left(R^3 - r_p^3\right) + \frac{2}{3}\pi\omega\tau^* r_b^3 + \left\{\frac{2}{3}\pi\omega\tau^*\left(r_p^2 + r_p r_b + r_b^2\right)\right\}\sqrt{(r_p - r_b)^2 + l^2} \quad (3.50)$$

The above heat generation equations are derived for either completely sliding or completely sticking condition. But in actual phenomenon, partial sliding and partial sticking condition exist. To accommodate that, a sliding factor δ is introduced in the heat generation equations which relates the two phenomenon of heat generation give in Eq. (3.51).

$$Q_{total} = (1 - \delta)Q_{sliding} + \delta Q_{sticking} \quad (3.51)$$

The δ range from 0 to 1, when δ=1 the sticking heat generation dominates over the sliding heat generation. When δ=0 the sliding heat generation dominates over the sticking heat generation. But in the actual phenomenon, the sliding factor is much closer 0.58 [141] as the high transportation of the softer material from the advancing side to the retreating side occur on the tool front . On the retreating side, the material gets extruded between the tool wall and the colder material away from the weld zone. The extruded material is then forged by the tool on the trailing side to form a welded joint.

3.4 Three-dimensional finite element model

A three-dimensional finite element transient thermal model is presented in the current work to analyze the heat transfer and temperature distribution in an FSW process. All the thermal properties are considered for the analysis. The temperature dependent material properties of Aluminium alloy is shown in Table 3.1. The melting point of the commercial grade Aluminium alloy is about 660^{o}C. The temperature-dependent friction coefficient of Aluminium and steel is shown in Table 3.2.

Table 3.1: Temperature-dependent material properties of Aluminium used in FE analysis[142], [143].

Temperature ºC	Thermal Conductivity W/mºC	Heat Capacity J/kgºC
37.8	162	945
93.3	177	978
148.9	184	1004
204.4	192	1028
260	201	1052
315.6	207	1078
371.1	217	1104
426.7	223	1133

Table 3.2: Temperature-dependent friction coefficient of Aluminium and steel [142], [143].

Temperature (ºC)	Friction Coefficient, *f*
22	0.11
160	0.11
200	0.26
400	0.35
580	0.47

However, the natural convection in the simulation, a convective heat transfer is implemented on all the surfaces except the bottom surface. The convective heat transfer coefficient is taken to be 10 (W/m^2K) [144]. In the actual process, the main source of heat loss is due to the conduction of the backing plate (on which the workpiece rests). But in this simulation, an equivalent convective heat transfer is taken instead of conduction at the bottom surface. The conduction heat transfer is much higher than the convective heat transfer. So, for simulation purpose this convective (instead of conduction) heat transfer coefficient is taken as 100 (W/m^2K) [145]. This ensures the amount of heat loss by the bottom surface is the same as that of conduction through the backing plate.

In the thermal model, the actual conditions are accommodated as far as possible. The following assumptions are made in developing the present thermal model of an FSW process.

a) All the thermal properties are considered as a function of temperature.
b) Linear Newtonian convection cooling is considered on all the surfaces.
c) Heat generation is considered as a load.

The governing differential equation for heat conduction for a homogenous, isotropic solid without heat generation in the rectangular coordinate system (x, y, z) can be expressed as:

$$\frac{\partial}{\partial x}\left[K\ \frac{\partial T}{\partial x}\right]+\frac{\partial}{\partial y}\left[K\ \frac{\partial T}{\partial y}\right]+\frac{\partial}{\partial z}\left[K\ \frac{\partial T}{\partial z}\right]\ =\ \rho c\frac{\partial T}{\partial t} \tag{3.52}$$

where

K = thermal conductivity

T = temperature

ρ = density of the material

c = specific heat

t = time

Above equation can be written as:

$$\rho c\frac{\partial T}{\partial t}=-\{L\}^{T}\{q\} \tag{3.53}$$

where

$\{L\}=\begin{Bmatrix}\frac{\partial}{\partial x}\\ \frac{\partial}{\partial y}\\ \frac{\partial}{\partial z}\end{Bmatrix}$ = vector operator,

$\{q\}$ = heat flux vector,

$\{L\}^{T}\{q\}=\nabla.\{q\}$, and

$\{L\}T=\nabla T$

where

∇ represents grad operator,

$\nabla.$ represents divergence operator.

Fourier's law is used to relate the heat flux vector to the thermal gradient

$\{q\} = -[D]\{L\}T$

where

$[D] = \begin{bmatrix} K & 0 & 0 \\ 0 & K & 0 \\ 0 & 0 & K \end{bmatrix}$ = conductivity matrix.

Equation (3.53) can be written as:

$$\rho c \frac{\partial T}{\partial t} = \{L\}^T([D]\{L\}T) \tag{3.54}$$

To solve Eq. (3.54), we need a set of boundary conditions.

(i) Initial condition

A specified initial temperature for the FSW that covers all the elements of the specimen:

$$T = T_\infty \text{ for } t = 0 \tag{3.55}$$

where T_∞ is the ambient temperature.

To develop second and third boundary conditions we consider energy balance at the work surface as:

Heat supply = Heat loss.

(ii) First boundary condition

A specific heat flows acts over tool surface S_1:

$$q_n = -q_{\text{sup}} \tag{3.56}$$

The quantity q_n represents the component of the conduction heat flux vector normal to the work surface. The quantity q_{sup} represents the heat flux supplied to the work surface in $\frac{W}{m^2}$, from an external FSW tool.

$$q_n = \{q\}^T \{n\}$$

on the surface S_1 for $t > 0$ (3.57)

where

$\{n\}$ = unit outward normal vector.

(iii) Second boundary condition:

Considering heat loss (q_{conv}) due to convection over remaining surface S_2 (Newton's law of cooling):

$$q_n = q_{conv}$$

or

$$\{q\}^T \{n\} = h_f (T - T_\infty)$$

On surface S_2 for $t > 0$. (3.58)

Pre-multiplying Eq. (3.54) by a virtual change in temperature, integrating over the volume of the element, combining with Eqs. (3.57) and (3.58), and with some algebraic manipulation we get:

$$\int_{vol} \left(\rho c \delta T \left(\frac{\partial T}{\partial t} \right) + \{L\}^T (\delta T)([D]\{L\}T) \right) d(vol) = \int_{s_1} \delta T q_{\sup} d(S_1) + \int_{s_2} \delta T h_f (T_\infty - T) d(S_2) \quad (3.59)$$

where

δvol = volume of the element

δT= an allowable virtual temperature. $(= \delta T(x, y, z, t))$

Derivation of heat flow matrices

As stated before, the variable T is allowed to vary both in space and time. This dependency is expressed as:

$$T = \{N\}^T \{T_e\} \quad (3.60)$$

where

$T = T(x, y, z, t)$ = temperature

$\{N\} = \{N(x, y, z)\}$ = element shape function

$\{T_e\} = \{T_e(t)\}$ = nodal temperature vector.

The time derivatives of Eq. (3.60) may be written as:

$$\dot{T} = \frac{\partial T}{\partial t} = \{N\}^T \{T_e\} \quad (3.61)$$

δT has the same form as *T:*

$$\delta T = \{\delta T_e\}^T \{N\} \tag{3.62}$$

The combination of $\{L\}T$ is written as:

$$\{L\}T = [B]\{T_e\}$$

where

$$[B] = \{L\}\{N\}^T \tag{3.63}$$

The variational statement of Eq. (3.59) can be combined with Eqs. (3.60, 3.61, 3.62 & 3.63) to yield:

$$\int_{vol} \rho c \{\delta T_e\}^T \{N\}\{N\}^T \{\dot{T}_e\} d(vol) + \int_{vol} \{\delta T_e\}^T [B]^T [D][B]\{T_e\} d(vol) = \int_{S_1} \{\delta T_e\}^T \{N\} q_{\sup} d(S_1) + \int_{S_2} \{\delta T_e\}^T \{N\} h_f \left(T_\infty - \{N\}^T \{T_e\}\right) d(S_2) \tag{3.64}$$

The density ρ is assumed to remain constant and specific heat *c* may vary over the element. Finally $\{T_e\}$, $\{\dot{T}_e\}$ and $\{\delta T_e\}$ are nodal quantities and do not vary over the element, so that they also may be taken out from the integrals. Now, since all quantities are pre-multiplied by $\{\delta T_e\}$, this term may also be dropped from the resulting equation. Thus Eq. (3.64) may be reduced to:

$$\rho \int_{vol} c \{N\}\{N\}^T d(vol) \{\dot{T}_e\} + \int_{vol} [B]^T [D][B] d(vol) \{T_e\} = \int_{S_1} \{N\} q_{\sup} d(S_1) + \int_{S_2} T_\infty \{N\} h_f d(S_2) - \int_{S_2} h_f \{N\}\{N\}^T \{T_e\} d(S_2) \tag{3.65}$$

Equation (3.65) can be rewritten as:

$$[C_e^t]\{\dot{T}_e\} + ([K_e^{th}] + [K_e^{tc}])\{T_e\} = \{Q_e^f\} + \{Q_e^c\}$$

where

$[C_e^t] = \rho \int_{vol} c\{N\}\{N\}^T d(vol)$ = element specific heat matrix

$[K_e^{tb}] = \int_{vol} [B]^T [D][B] d(vol)$ = element diffusion conductivity matrix

$[K_e^{tc}] = \int_{S_2} h_f [N][N]^T d(S_2)$ = element convection surface conductivity matrix

$\{Q_e^f\} = \int_{S_1} \{N\} q_{sup} d(S_1)$ = element heat flow vector for surface S_1

$\{Q_e^c\} = \int_{S_2} T_\infty h_f \{N\} d(S_2)$ = element convection surface heat flow vector.

The element specific heat matrix $[C_e^t]$ is evaluated from the specific heat of the material. The solution is obtained using the ANSYS FE package.

3.4.1 Meshing details

For transient thermal analysis 3D 8 noded brick element, Solid 70 having temperature as the degree of freedom is used as shown in Figure 3.6. The nodes are represented by the small alphabets (i to p) and the face of element is represented by the numerical value (1 to 6) It is ideal for the problems associated with transient thermal conduction. The plate mesh for the transient thermal analysis is shown in Figure 3.7. The mesh is finer in the weld region while coarse away for the weld line. The plate dimensions used in the models are 200 × 150 × 6 mm for all the analysis.

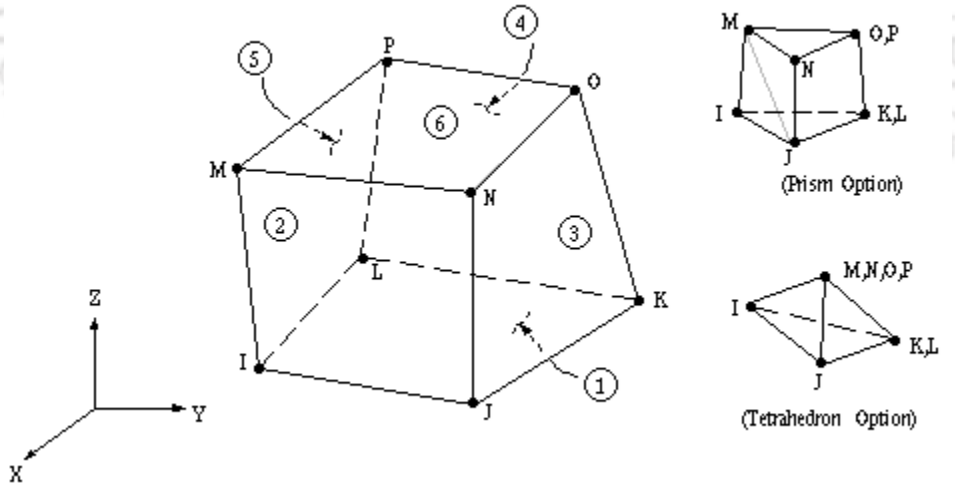

Figure 3.6: Solid 70 brick element (ANSYS) used for thermal analysis.

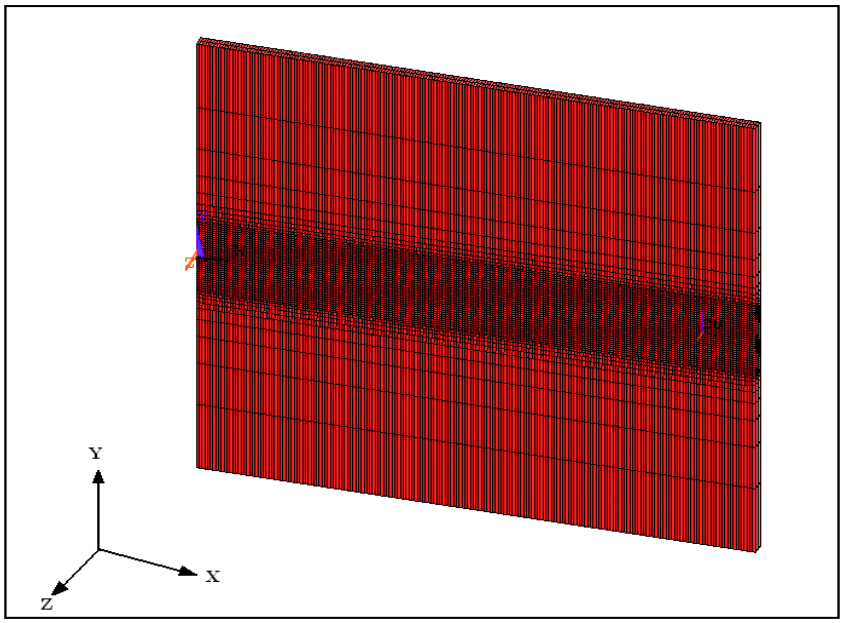

Figure 3.7: FE model and meshing view for transient thermal analysis.

To choose the right mesh sizes a mesh sensitive analysis is performed using four different sizes of element sizes. The analysis is performed on the temperature profile basis of the four different mesh sizes. The comparison of the peak temperature of all four meshes with the number of elements and calculation time is shown in Table 3.3. The tool is having 21 mm shoulder diameter and it is provided 1100 rpm rotational speed and 2 mm/s traverse speed. The temperature profile is obtained in all the four cases and no significant change in rise and fall of temperature is found across the welding direction as evident from Figures 3.8 and 3.9. It is observed that the peak temperature rises from Mesh 1 to Mesh 3 and no significant change is observed on further increase in the number of elements. So, Mesh 3 is taken for studying the temperature distribution pattern.

Table 3.3: The peak temperature obtained for all four meshes.

Mesh	No. of Elements	Computational Time (hr:min)	Peak Temperature (K)
Mesh 1	7500	00:35	625.89
Mesh 2	13400	01:15	627.77
Mesh 3	45000	03:47	628.63
Mesh 4	79000	05:53	628.95

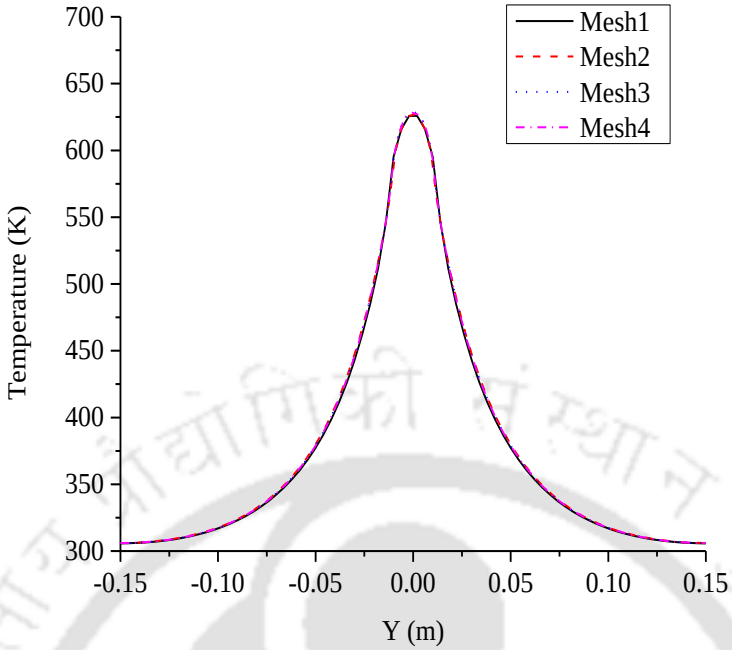

Figure 3.8: The rise and fall of temperature across the weld line of all four mesh sizes.

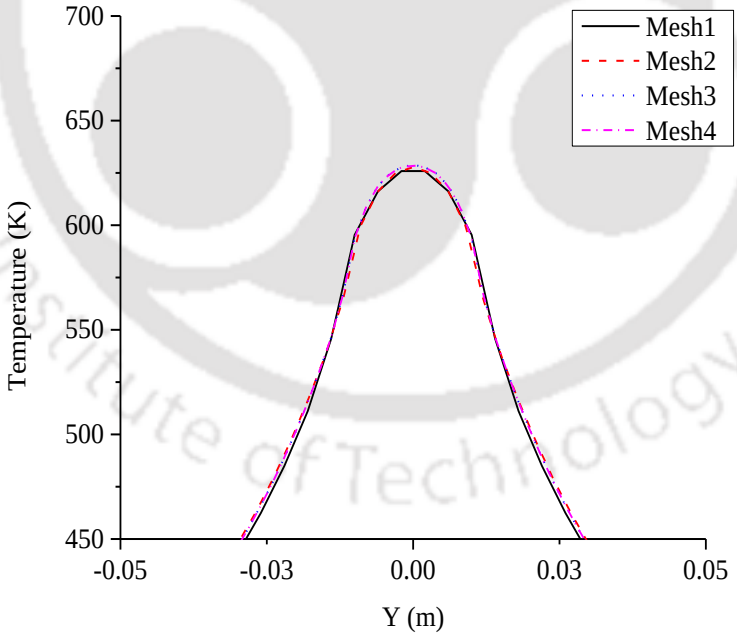

Figure 3.9: The variation of all four mesh sizes in the temperature profile.

3.5 Material flow models for similar material

In this work, the finite volume model is employed for simulating the task. Aluminium alloy 6061 is used as the plate material for the analysis. The dimensions of the plate are 200 mm long, 150 mm total width and 6 mm thick. A 25 mm diameter tool shoulder with a conical pin having 6 mm base and 3 mm pin tip diameter is used in this study. The length of the pin is 5.75 mm having threads with a pitch 1.5 mm is shown in Figure 3.10 (a). The tool is incorporated into the model as a wall with 0.1 mm depression in the weld plate due to the plunging force during the welding. The weld plate is meshed using tetrahedral elements. The tools are incorporated as walls in the weld plate into the model. The weld plate is meshed using tetrahedral elements. The mesh is refined near the tool pin region shown in Figure 3.10 (b). The analysis is performed in ANSYS Fluent 14.5. For further analysis, different tool geometries are considered to study their effect on material flow.

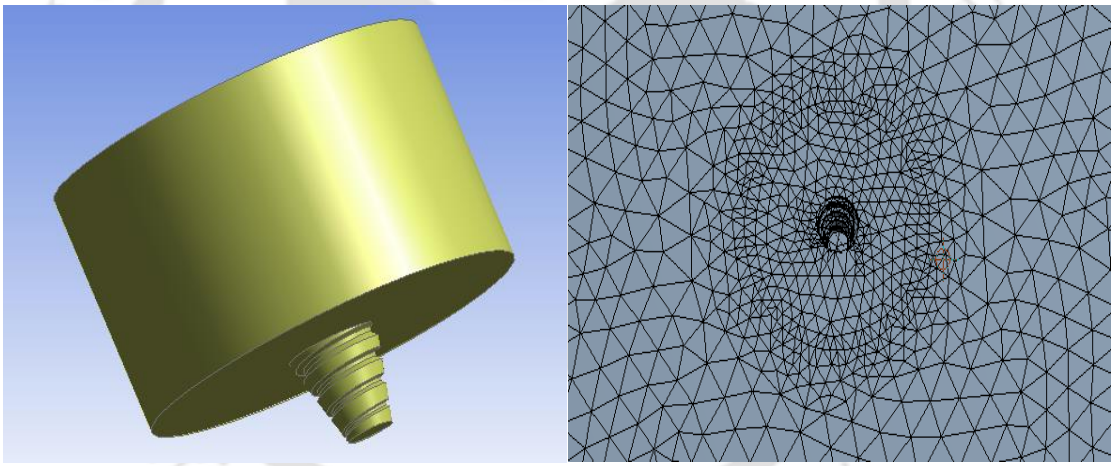

(a) (b)

Figure 3.10: (a) The model of the tool, (b) the meshing and the tool impression.

Table 3.4: The different mesh size taken for the analysis.

Mesh	No. of Elements	Computational Time (hr:min)	Peak Temperature (K)
Mesh1	33,669	8:33	742.25
Mesh2	132,533	13:47	744.44
Mesh3	198,057	18:16	746.07
Mesh4	394,145	32:17	746.87

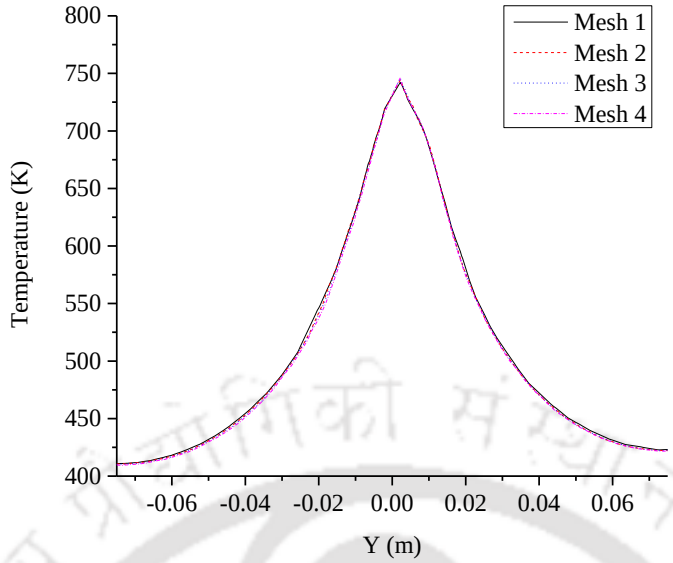

Figure 3.11: The welding cross-sectional temperature profile on Advancing and retreating side. The positive value of Y is Advancing and negative value of Y is retreating side while 0 is the centre line of the weld.

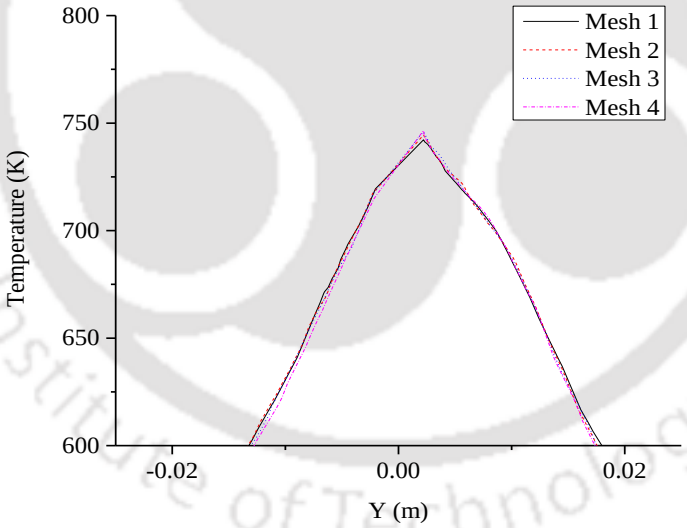

Figure 3.12: The difference in the peak temperature of all four meshes.

For right mesh sizes, a mesh sensitive analysis is performed using four different sizes of element sizes just like the previous case. The rise and fall of temperature profiles of all four cases are compared. The number of element and the time of computation with peak temperature are obtained in each case which is shown in Table 3.4. The tool is provided with 1100 rpm rotational speed and 2 mm/s traverse speed. All four cases provide similar value for rise and fall of temperature. The temperature profile along

the cross-section of the weld line is shown in Figures 3.11 and 3.12. A rising trend in peak temperature is observed from Mesh 1 to Mesh 4. The peak temperature rise in case of Mesh 3 and Mesh 4 is not significant but the calculation time rises significantly. So, here Mesh 3 is used for the flow analysis of FSW. The Computer configurations used to perform the current analysis are processor: Intel Core i3-4130 @ 3.40 GHz @3.40 GHz, RAM: 4 GB

3.5.1 Boundary conditions

In the simulation, the tool movement is assumed along the X direction from the positive to negative so the material flow is opposite i.e., from negative to the positive X direction. The tool is assumed to be in the positive Z direction and its rotation is considered to be in an anticlockwise direction. This flux has been calculated by the heat generation equations given in section 3.2 and 3.3. The heat generation is divided by the total tool surface area of the tool to provide heat flux. The schematic diagram of the material flow model used in the current analysis is shown in Figure 3.13.

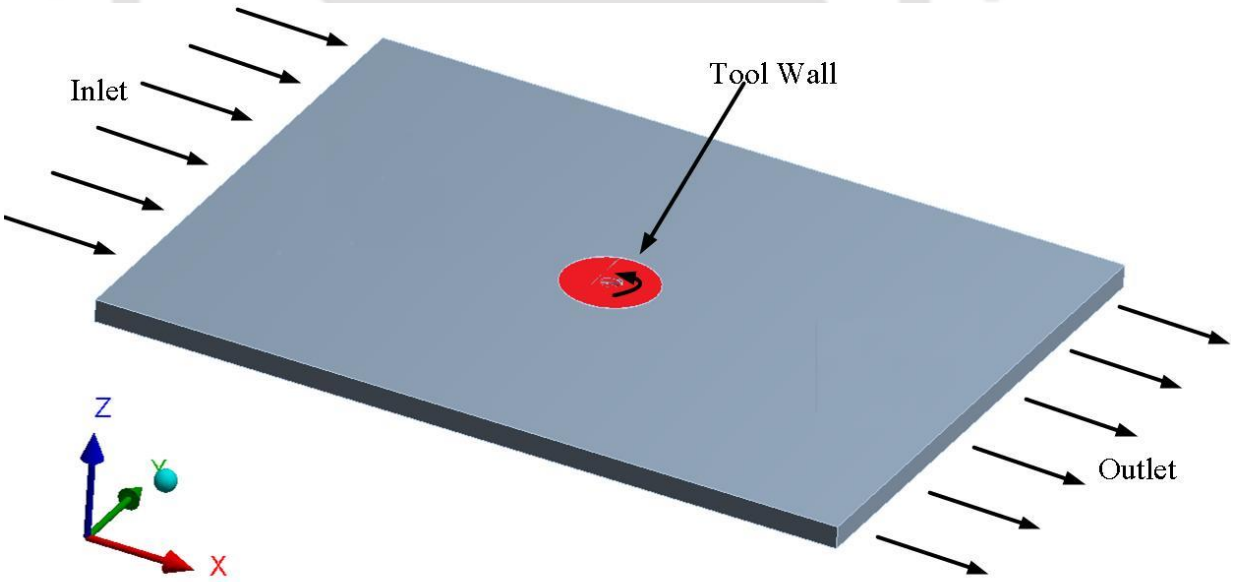

Figure 3.13: The schematic diagram of the material flow analysis of similar FSW.

This heat flux is given to the tool wall. The convection coefficient from all the surfaces is taken as 10 W/m^2-K except the bottom surface similar to previous analysis. The bottom surface is provided with 100 W/m^2-K as the convection coefficient.

3.5.2 Governing equations

The finite volume method (FVM) model incorporates a highly viscous material as the region near the pin gets plasticized due to the heat produced by the rotation of the tool. For the simplification of the model, the following assumptions have been made.

(a) There is no tilt angle given to the spindle of tool i.e. tool rotates perpendicularly inside the workpiece.

(b) The heat generation inside the material is not considered.

(c) There is a 'no slip condition' at the contact between the surface of pin and workpiece.

(d) The material has isotropic viscosity and is an incompressible fluid.

(e) The heat loss due to radiation is negligible.

(f) The effect of gravity on the material flow is negligible.

The process of FSW follows the equations of mass, momentum and energy conservation. Since the mass of material is constant; the mass conservation equation is given by:

$$\frac{\partial u}{\partial x}+\frac{\partial v}{\partial y}+\frac{\partial w}{\partial z}=0 \tag{3.66}$$

where u, v and w are the velocities in the x, y and z directions, respectively. The momentum conservation is governed by the Navier-Stokes equation:

$$\frac{\partial u}{\partial t}+u\frac{\partial u}{\partial x}+v\frac{\partial u}{\partial y}+w\frac{\partial u}{\partial z}=F_x-\frac{1}{\rho}\frac{\partial p}{\partial x}+\mu\left(\frac{\partial^2 u}{\partial x^2}+\frac{\partial^2 u}{\partial y^2}+\frac{\partial^2 u}{\partial z^2}\right)$$

$$\frac{\partial v}{\partial t}+u\frac{\partial v}{\partial x}+v\frac{\partial v}{\partial y}+w\frac{\partial v}{\partial z}=F_y-\frac{1}{\rho}\frac{\partial p}{\partial y}+\mu\left(\frac{\partial^2 v}{\partial x^2}+\frac{\partial^2 v}{\partial y^2}+\frac{\partial^2 v}{\partial z^2}\right)$$

$$\frac{\partial w}{\partial t}+u\frac{\partial w}{\partial x}+v\frac{\partial w}{\partial y}+w\frac{\partial w}{\partial z}=F_z-\frac{1}{\rho}\frac{\partial p}{\partial z}+\mu\left(\frac{\partial^2 w}{\partial x^2}+\frac{\partial^2 w}{\partial y^2}+\frac{\partial^2 w}{\partial z^2}\right) \tag{3.67}$$

where F_x, F_y and F_z are the forces in x, y and z directions, respectively; p is the static pressure of the flow field; μ is the viscosity of fluid and ρ is the density of material. The energy conservation equation is given by:

$$\rho c\left(\frac{\partial T}{\partial t}+u\frac{\partial T}{\partial x}+v\frac{\partial T}{\partial y}+w\frac{\partial T}{\partial z}\right)=K\left(\frac{\partial^2 T}{\partial x^2}+\frac{\partial^2 T}{\partial y^2}+\frac{\partial^2 T}{\partial z^2}\right) \tag{3.68}$$

here c is the specific heat of material, K is the thermal conductivity of material and T is the temperature of fluid.

3.5.3 Solver and discretization schemes

The details of the solution parameters used in the ANSYS Fluent package is provided in this section. The double precision is used throughout the analysis. The transient analysis is carried out using a pressure based solver as density is kept constant. The second order implicit method is used to formulate the transient problem. The SIMPLE scheme is used for pressure-velocity coupling. Different discretization schemes are used in the analysis like least square cell-based discretization is used for convection-diffusion terms. For pressure second order and for momentum and energy power law discretization is used in the formulation. The linear system of equations are solved by the Gauss-Seidel iteration methods where the initial values for pressure and u, v and w are taken zero while Temperature is taken as 300 K (ambient) throughout the domain.

The residual values to stop the iteration process are taken as 10^{-4} for x, y and z momentum and continuity equations while for the energy it is taken as 10^{-7}. The under-relaxation factors are also altered to reduce the complexity of the problem. The typical values for p, F, ρ, momentum and energy are 1, 1, 1, 0.85 and 0.9 respectively.

3.5.4 Material properties

The composition of the Aluminium 6061 alloy is Al (95.8-98.6), Cu (0.15-0.4), Mg (0.8-1.2), Cr (0.04-0.35), Si (0.4-0.8) and Fe are the major components, whereas Mn, Ti, Zn and other account less than 1 % by weight. However, Cu-B370 alloy contains 99.9 % Cu and Ni, Sn, Al, Fe and other account less than 0.1 % by weight.

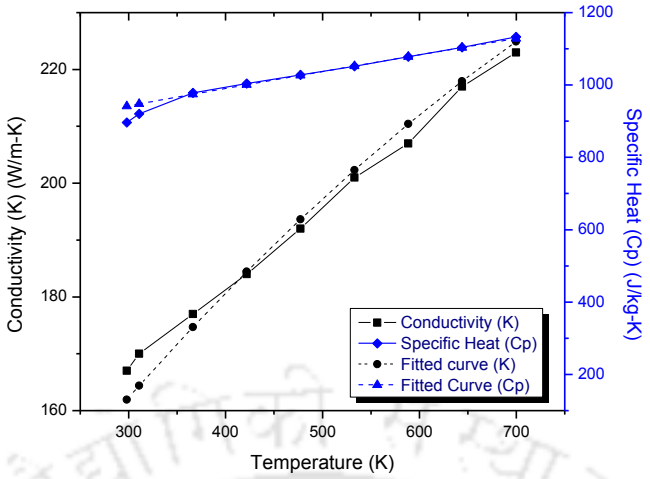

Figure 3.14: The temperature-dependent thermal conductivity and specific heat of AA6061 alloy, along with the fitted curve [144, 146].

The temperature dependent thermal material properties are considered for the analysis. The thermal conductivity (K) and specific heat (c) of AA6061 is given by the Eqs. (27) and (28) [144, 146]. The fitted curve for thermal conductivity (K) and specific heat (c) of AA6061 is shown in Figure 3.14.

$$K = 96.442 + 0.2466T - 0.00009T^2 \tag{3.69}$$

$$c = 794.58 + 0.5051T - 0.00004T^2 \tag{3.70}$$

where T is the temperature in Kelvin (K). For the simulation, the value of viscosity of the material is highly significant. A very high or very low value cannot be given to the whole material. The constant value of viscosity results in wrong values of temperature distribution and velocity magnitude. This is so because the temperature is high only the region close to the rotating tool and it decreases as the distance increases away from the tool. Consequently, the viscosity should change in different regions of the weld. Therefore, the viscosity approximated according to Colegrove et al. [147] as:

$$\mu = \frac{\sigma_R}{3\dot{\varepsilon}} \tag{3.71}$$

where μ is the viscosity of the material, $\dot{\varepsilon}$ is the strain rate and σ_R is the effective stress given by Eq. (30).

$$\sigma_R = \frac{1}{\alpha}\ln\left[\left(\frac{Z}{A}\right)^{\frac{1}{n}} + \left(1+\left(\frac{Z}{A}\right)^{\frac{2}{n}}\right)^{\frac{1}{2}}\right] \tag{3.72}$$

and

$$Z = \dot{\varepsilon}\exp\left(\frac{Q}{RT}\right) \tag{3.73}$$

where Q is the activation energy, R is the universal gas constant, T is the temperature, Z is the Zener-Holloman parameter, α, A and n are constants related to the material. The Tello et al. [148] experimentally obtained the material constant for AA6061 which are as follows:

A = 1.63 x 1013 s^{-1}

α = (1/60.7) MPa^{-1}

n = 5.33

Q = 191 kJ/mol

A constant density is taken for the Aluminium and Cu alloys i.e. 2700 kg/m^3 and 8960 kg/m^3. The temperature dependent thermal conductivity and specific heat for Cu B370 is given by

$$K = 421.272 - 0.07009T - 0.00000125T^2 \tag{3.74}$$

$$c = 373.2151 + 0.04384T + 0.000039T^2 \tag{3.75}$$

The temperature dependent viscosity of Cu is approximated by the Arrhenius equation[149]

$$v^{Cu} = v_0\, e^{\left(\frac{E}{RT}\right)} \tag{3.76}$$

where v_0 is the constant for Cu taken as 0.25 mPa-s[149], E is activation energy, R is the universal gas constant and T is the temperature in K.

3.6 Dissimilar material VOF Model

The volume of fluid (VOF) model is used for the dissimilar material FSW analysis. It is a multi-fluid interaction model in which the amount of fluid is determined by the volume fraction (β) of the fluid. The volume fraction of A fluid varies between 0 to 1 i.e. 0 means no amount of A fluid is present in that cell and 1 means the cell is full of

fluid A. Similarly, for fluid B the volume fraction varies between 0 to 1, such that the sum of all volume fraction is always unity. The governing equations are modified as: The continuity equation:

$$\frac{\partial}{\partial t}(\beta_A \rho_A) + \nabla.(\beta_A \rho_A \vec{v}) = 0 \tag{3.77}$$

The momentum conservation is governed by the Navier-Stokes equation:

$$\frac{\partial}{\partial t}(\beta_A \rho_A \vec{v}) + \nabla.(\beta_A \rho_A \vec{v}\vec{v}) = \vec{F} - \nabla p + \nabla.[\mu_A(\beta_A(\nabla \vec{v} + \nabla \vec{v}^T))] + \beta_A \rho_A \vec{g} \tag{3.78}$$

where p is the static pressure of the flow field; μ is the viscosity of the fluid and ρ is the density of the material. The energy conservation equation is given by:

$$\rho_A c_A \left(\frac{\partial T}{\partial t} + \vec{v}.\nabla T\right) = \nabla.K_A(\nabla T) \tag{3.79}$$

here, c is the specific heat of material, K is the thermal conductivity of material and T is the temperature of the fluid.

3.6.1 Boundary conditions

The heat input is provided as heat flux through the tool wall, which is based on the heat generation Eq. (3.80).

$$Q_T = (1-\delta)Q_{sliding} + \delta Q_{sticking} \tag{3.80}$$

where δ is the sliding factor which is taken as 0.58 [141], $Q_{sliding}$ is the frictional heat generation and $Q_{sticking}$ is the sticking heat generation. Heat generation by sliding and sticking condition is given by Eqs. (3.81) and (3.82).

$$Q_{sliding} = \alpha\left(\frac{2}{3}\pi f^A \omega P\left(R^3 - r_p^3\right) + \frac{2}{3}\pi f^A \omega P r_p^3 + f^A \pi S_{ys}^A r_p h v\right) + (1-\alpha)\left(\frac{2}{3}\pi f^C \omega P\left(R^3 - r_p^3\right) + \frac{2}{3}\pi f^C \omega P r_p^3 + f^C \pi S_{ys}^C r_p h v\right) \tag{3.81}$$

$$Q_{sticking} = \alpha(\pi \omega l \tau^A (R^2 - r_p^2)) + (1-\alpha)(\pi \omega l \tau^C (R^2 - r_p^2)) \tag{3.82}$$

where α is the ratio of tool area inside Al plate to the total area of the tool wall, f^A and f^C are the coefficient of friction of Al and Cu taken as constant 0.3 [127] and 0.45 [150] respectively, ω and v are the rotational and travelling speed, P is the plunging pressure and R and r_p are the shoulder and pin radius, τ^A, τ^C, S_{ys}^A and S_{ys}^C are the shear and yield strength of the Al and Cu and l is the height of the pin. The equation is

further divided by the total area of the tool wall to get the value of heat flux. Similar to the previous analysis, the convection coefficient from all the surfaces is taken as 10.0 W/m^2-K except from the bottom surface as it remains in contact with the base plate so the heat loss is due to conduction. The base plate considered in this case is mild steel for which the convection coefficient is taken as 100 W/m^2-K. The schematic diagram of the model used in the present dissimilar material flow analysis is shown in Figure 3.15. The diagram shows all the solid and fluid regions along with advancing and retreating sides and the co-ordinate system used in the present analysis. The origin of the coordinate system is taken at the tool rotation axis on the top surface of the tool wall same as previous analysis.

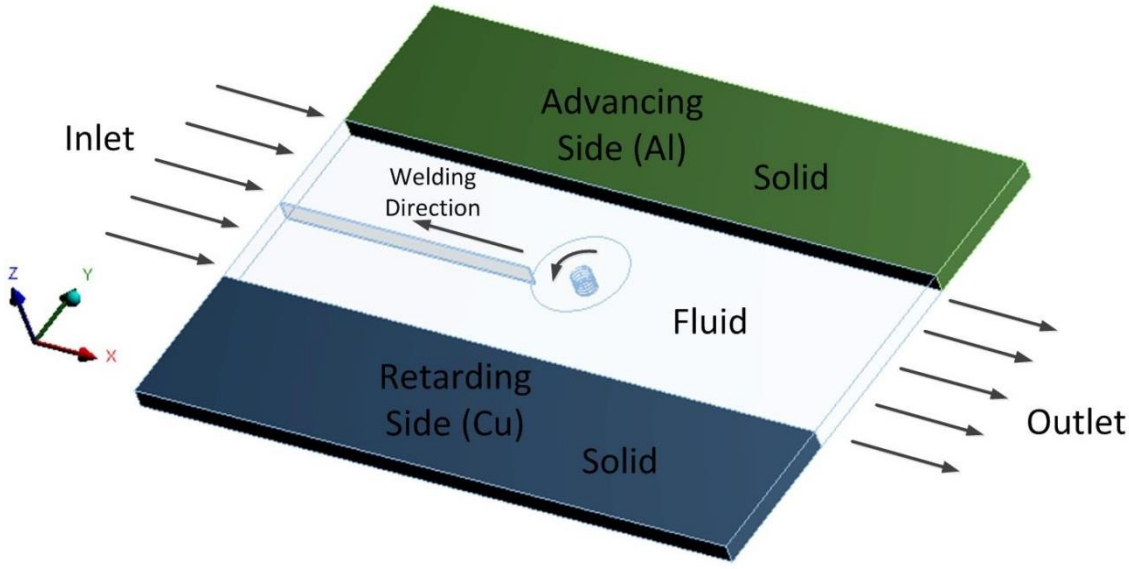

Figure 3.15: The Schematic diagram used in material flow model of dissimilar FSW.

3.7 Experimental details

Experiments are performed to study the thermal history data of the welding. This thermal history is then compared with the thermal history obtained from the simulation. The 6 mm thick with a surface area of 200 mm long and 75 mm wide material is used for the experiments is i.e. same as simulation. The AA6061 workpiece is prepared for similar FSW as shown in Figure 3.16.

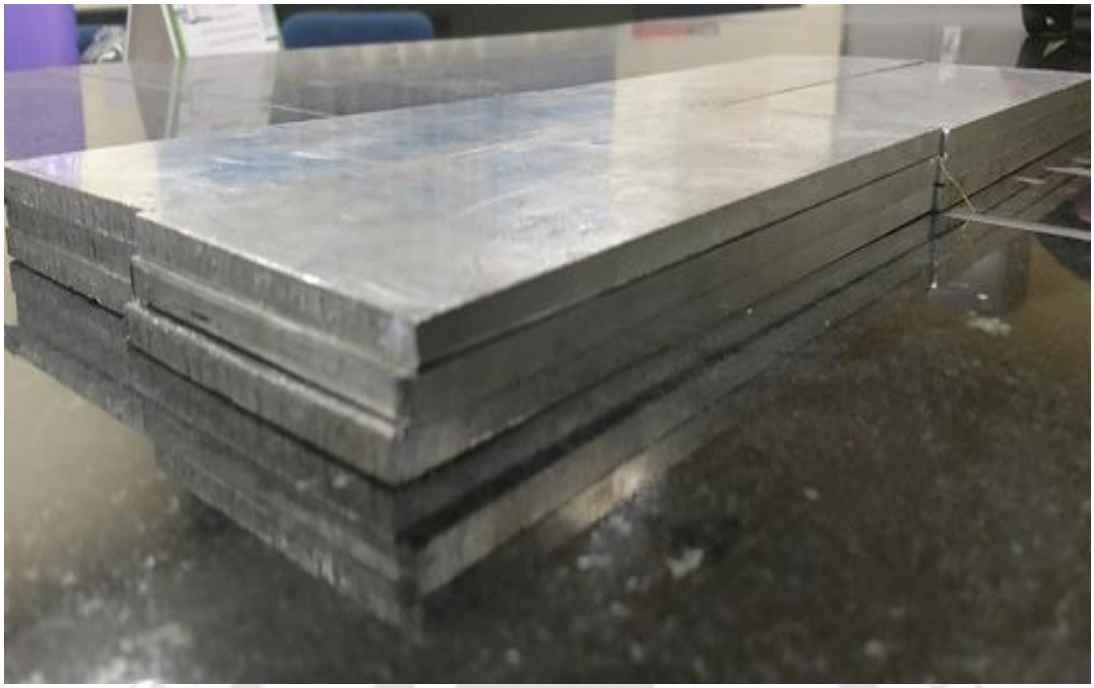

Figure 3.16: AA6061 workpieces used to perform welding.

Figure 3.17: Conical pin geometry used to perform welding.

Figure 3.18: FSW machine with thermocouples and data acquisition system.

A conical SS310 alloy tool is used to perform the FSW as shown in Figure 3.17. The reason for choosing this material is its ease of machinability, high strength, low thermal conductivity, high formability and highly resistant to corrosion. For the measurement of the temperature of the workpieces 1 mm diameter K-type thermocouples (chromel and alumel wires) are used. The thermocouples are connected to the data acquisition system (Agilent-34970A) to record the temperature data. Different locations are chosen to attach the thermocouple based on the requirement. The FSW machine with mounted tool and workpieces with thermocouples and data acquisition system is shown in Figure 3.18. A square butt welding with zero root gap is clamped into the horizontal bed. The milling machine with a 7.5 hp capacity is used to perform the weld. The machine has a range of 50-1500 rpm tool rotation and 22-555 mm/min welding speed. The workpieces are kept on an anvil/backing plate of stainless steel. All thermocouples are attached 20 mm away from the weld line to record the temperature data. The schematic diagram of the experimental setup for recording thermal profile is shown in Figure 3.19. Here, the tool moves to perform welding and

thermocouples are kept at a particular place. However, in the case of material flow model the temperature profile recording point moves with time and tool wall is kept at the middle place as shown in Figure 3.20. The welding setup with thermocouples is shown in Figure 3.21.

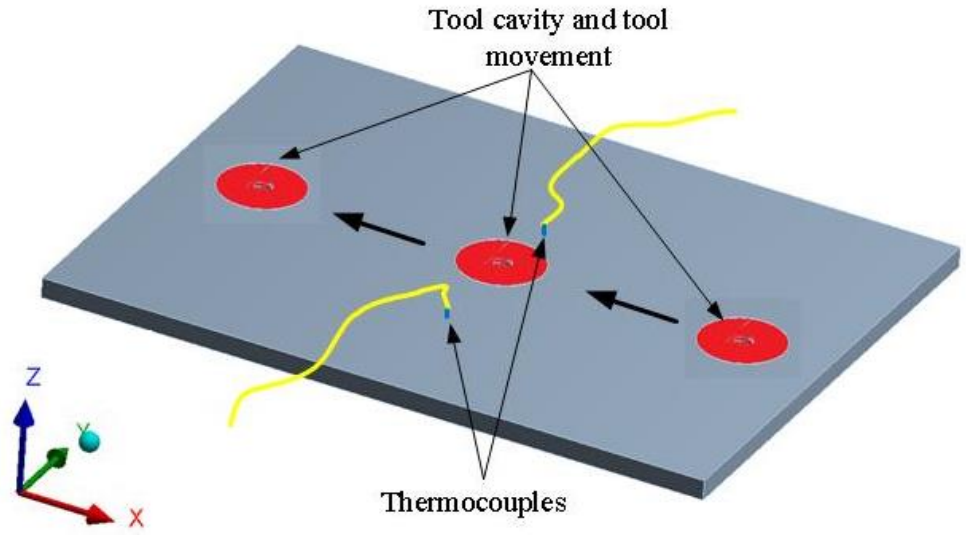

Figure 3.19: Experimental setup for measuring the thermal profile of FSW.

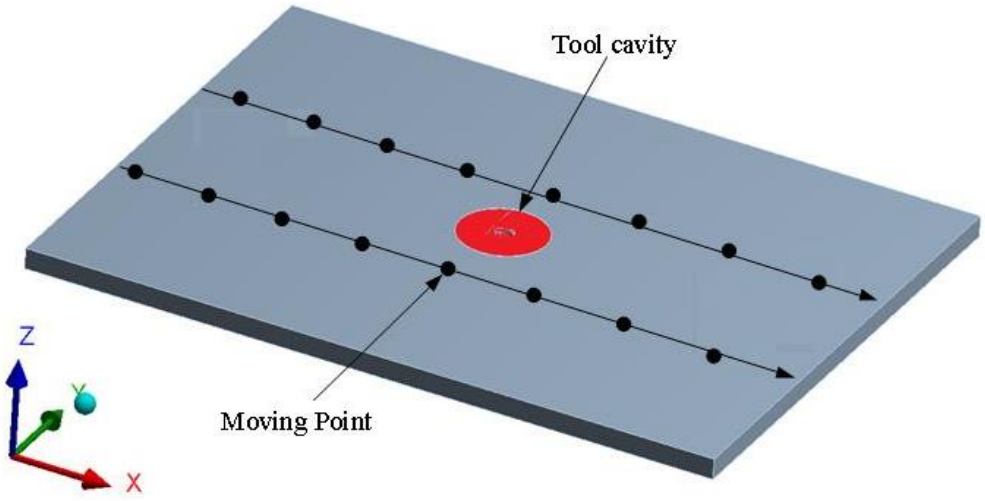

Figure 3.20: The moving point method used in transient material flow model to study the thermal profile of FSW.

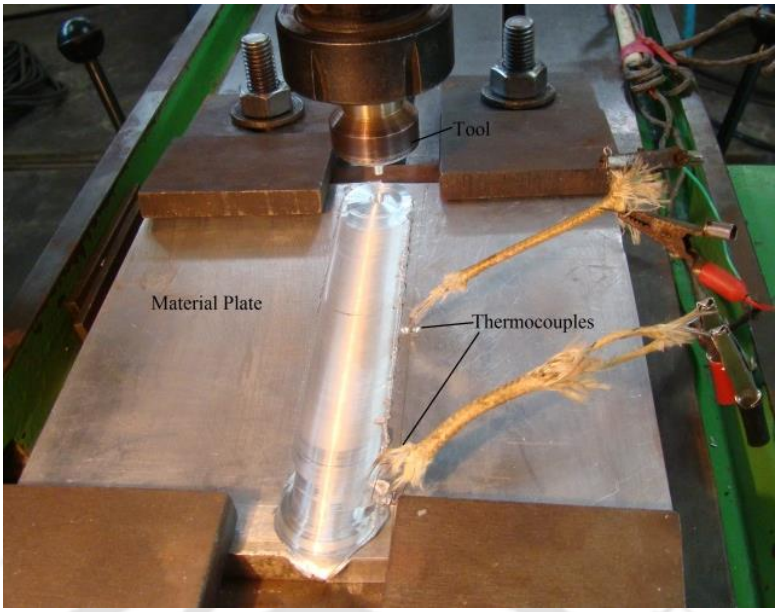

Figure 3.21: Experimental setup of the FSW performed.

Microstructural study

In FSW, the temperature of the process reaches upto 80-90% melting point temperature of the base material. Therefore, the microstructure of the material changes in the weld zone. The study of microstructure provides useful information regarding the material flow from both sides of the weld plates. In case of dissimilar material FSW, the microstructure study provides details about the dispersion one material into other which eventually reveals the mixing phenomenon of the welding process. The microstructure also helps in finding the defects in the welding joint. The procedure adopted for studying the microstructure is shown in Figure 3.22.

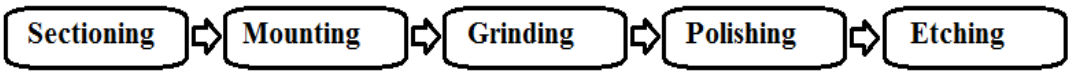

Figure 3.22: Procedure for microstructure analysis.

The first step is the sectioning of the weld plate to obtain a sample. Then the specimen is mounted in compression mounting compound (phenolic resin) in a hydraulically operated press. The moulds are heated by a thermostatically controlled slip-on heater and cooled by a finned slip-on cooler after reaching the curing temperature. Various polishing papers starting from 240 grit size upto 2000 are used to polish the sample. Polishing is performed by a single disc with five specimen holder automated polishing

machine. The specimen is rinsed with a continuous water supply. After grit polishing, cloth polish using a metal polish (silvo for Aluminium; brasso for Copper samples) is done. The polishing is performed with a slower disc rotation to obtain a scratchless mirror-like finish. The polishing is followed by etching by Keller's reagent. After etching the sample is thoroughly examined using the optical microscope.

3.8 Summary

This chapter provides the details of methodologies used to reach the stated objectives of the thesis. The chapter begins with the derivation of heat generation equations for cylindrical and conical pin geometries. The heat generation equations are formulated for frictional heat as well as plastic deformation heat. These equations are implemented in a finite element 3D transient thermal model. The FE modelling details are followed by the finite volume models which are used to analyze the material flow behaviour of the material during the process. Different approaches are used to analyze the similar material flow behaviour and dissimilar material flow behaviour of FSW with suitable boundary conditions. The temperature dependent thermal material properties are used in all the models. The mesh sensitivity analysis is carried out to achieve the best possible solution. The last part of the chapter details the experimental setup used for the validation of the model.

Chapter 4

Transient Thermal Analysis

4.1 Introduction

In this chapter, the finite element (FE) based model is used to study the transient temperature distribution of AA6061 plates FSW. The heat source model is proposed and the effect of process parameter on the temperature profile is studied. The investigations are also conducted on the importance of sticking condition implementation in the heat source. The shape of the contour along thickness is analyzed to understand the significance of the base plate. The model proposed is well verified with the experimentally obtained thermal profile.

4.2 Effect of rotational speed

For the study of the effect of rotational speed, a range of 1200-1600 rpm are taken with 2 mm/s welding speed and 27 mm shoulder diameter. Two points named as A and B is considered for the study of temperatures. The point A is taken on the weld line and the point B at a distance of 14 mm from the weld line (just outside the shoulder radius) as shown in Figure 4.1. The maximum temperature at A and B is shown in Table 4.1 with rotational speed. It is noted that the highest temperature is achieved in the case of highest rotational speed. The temperature variation perpendicular to the weld line is shown in Figure 4.2.

Table 4.1: Maximum Temperature vs. Rotational speed.

Rotational Speed, ω (rpm)	Max Temp point A (K)	Max Temp point B (K)
1200	673.3	598.7
1300	686.6	609.8
1400	698.9	620.1
1500	710.4	629.5
1600	721.2	638.2

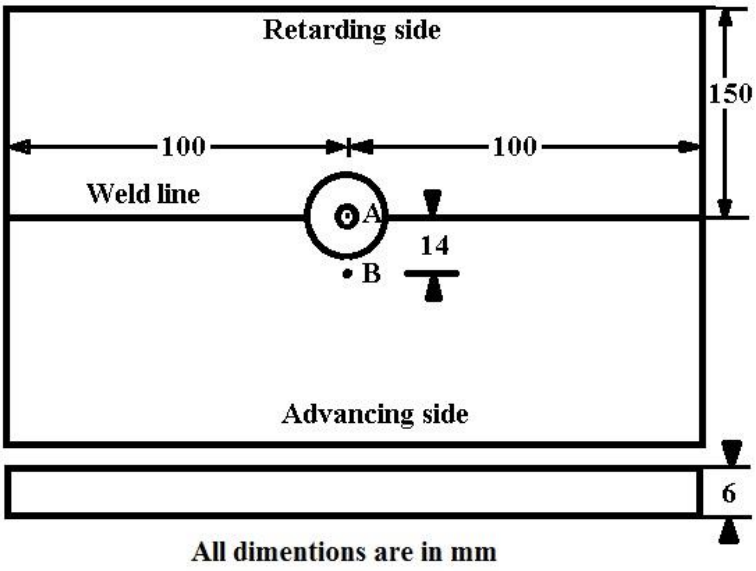

Figure 4.1: Location of point A and B on the plate top surface.

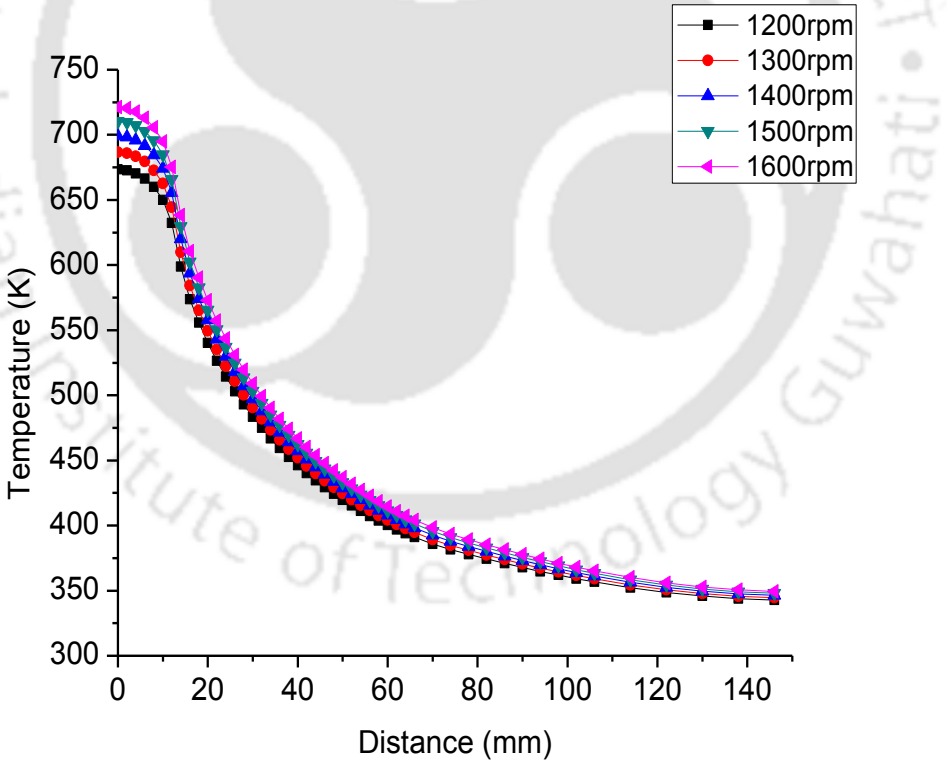

Figure 4.2: Temperature variation at 2 mm/s tool traverse speed and 27 mm tool shoulder diameter with rotational speed (t=50s).

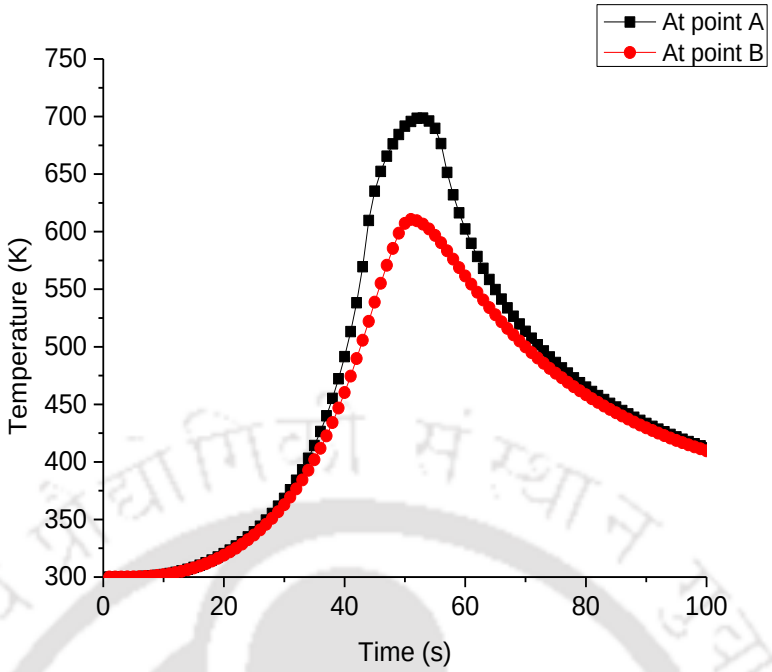

Figure 4.3: Transient temperature graph for 1400 rpm and 2 mm/s tool traverse speed.

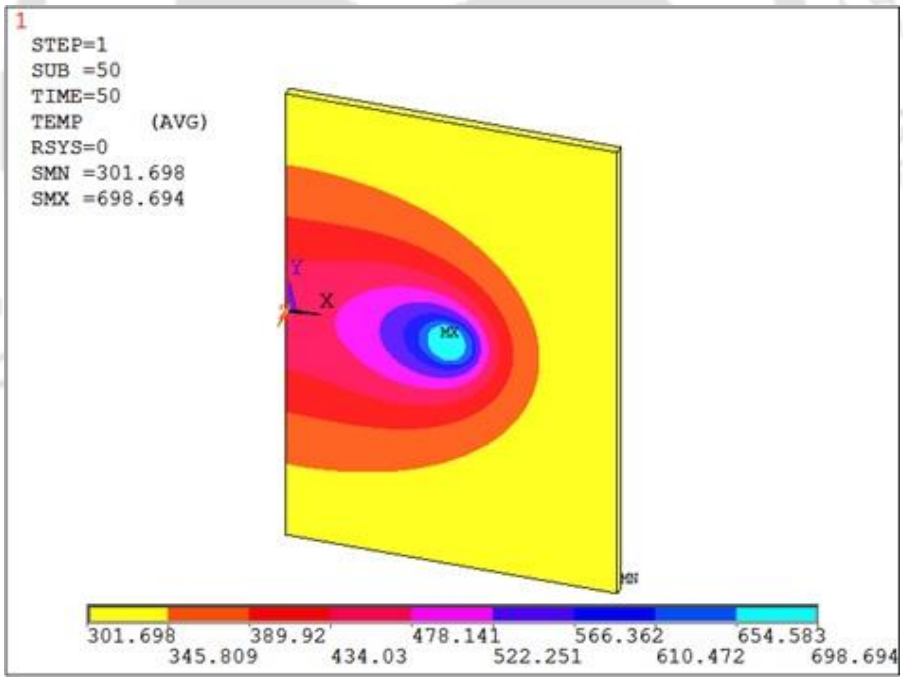

Figure 4.4: Temperature profile for 1400 rpm rotational speed and 2 mm/s tool traverse speed at 50s.

The temperature values attained in the weld line and at 14 mm away from the weld line is shown in Figure 4.3. It shows the heating and cooling rate at the centre line and away from the centre line. Whereas, the temperature contour of the 1400 rpm

simulation taken at 50 s time is shown in Figure 4.4. The temperature variation around the weld line is explained by showing the temperature pool of the weld material during the welding.

4.3 Effect of traverse speed

Four simulations are done in order to study the effect traverse speed. The rotational speed is remained same i.e. 1400 rpm for all the cases and tool shoulder is kept at 27 mm. The traverse speed is varied from 1.5 to 3 mm/s.

Table 4.2: The Maximum temperature at point A and B at different tool traverse speed.

Transverse Speed (mm/s)	Max Temp point A (K)	Max Temp point B (K)
1.5	702.7	628.2
2	698.9	620.1
2.5	683.3	600.3
3	679.1	590.3

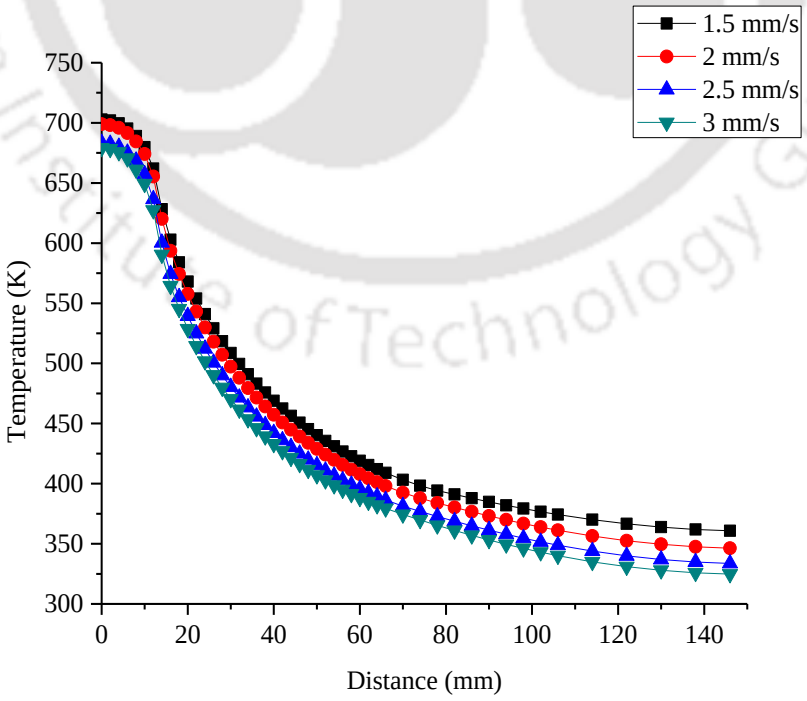

Figure 4.5: Temperature variation with traverse speed.

The maximum temperature values at points A and B are noted and shown in Table 4.2. Whereas, the temperature values with respect to the perpendicular distance from the weld line is shown in Figure 4.5. It represents the maximum temperature attained at the weld line with the cooling rate in the above cases.

4.4 Effect of tool diameter

For studying the tool diameter effect, the rotational speed of the tool is taken constant at 1400 rpm and traverse speed is taken as 2 mm/s. The tool diameters are varied between 21 to 30 mm. The temperature profiles for the different tool geometries are shown in Figure 4.6.

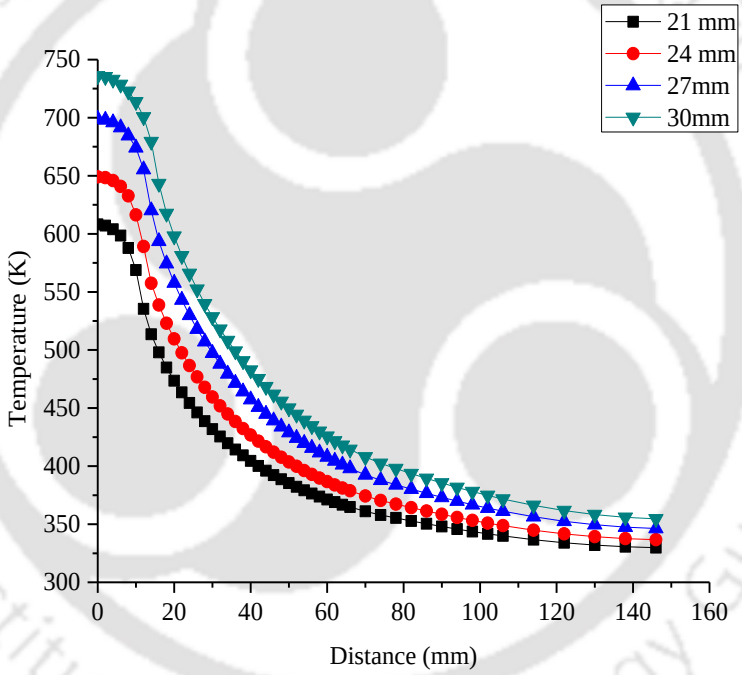

Figure 4.6: Temperature profiles for different shoulder diameter.

4.5 Results of sticking and sliding conditons

The temperature profiles of points A and B, with and without sticking conditions are explained in Figure 4.7.

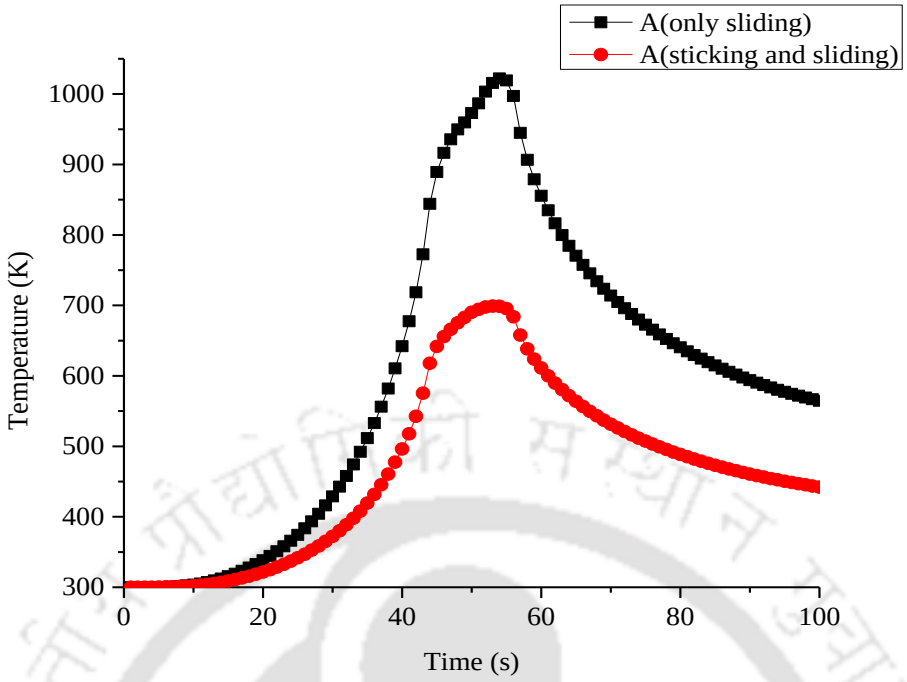

(a)

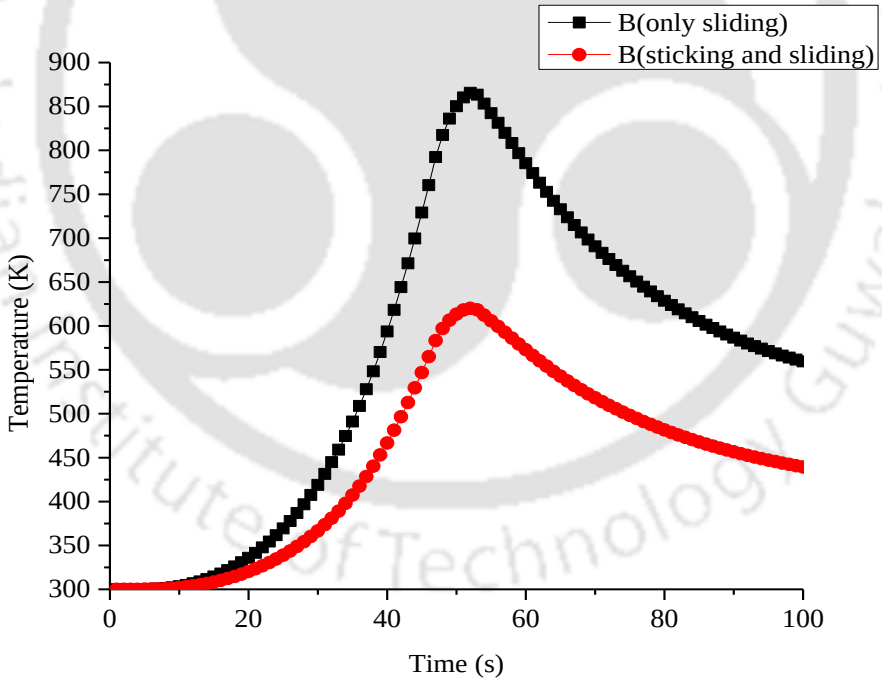

(b)

Figure 4.7: Temperature variation at (a) point A and (b) point B.

The maximum welding temperature is very high when only sliding condition is considered. It is found to be much higher than the melting point temperature of the material i.e. 923 K. But the maximum temperature attained with sticking and sliding

condition remains well under the limits. The analysis is done at 1400 rpm rotational speed, 2 mm/s welding or traverse speed for a 27 mm tool diameter. The maximum welding temperature value in case of the complete sliding condition is 1020 K however; the value for combined sticking and sliding condition is 723 K on the weld line. The value obtained in the case of combined sticking and sliding condition is more feasible. So, it is necessary to involve the sticking condition along with the sliding into the heat source computation. The temperature obtained by the implementation of both the condition is more reasonable and close to the real one.

4.6 Temperature distribution along the thickness

It is observed that there are temperature differences at the top and the bottom surface of the weld plate. This difference in top and bottom surface is found higher at centre line but it gradually decreases on moving away from the centre line or weld line. This difference in temperature is studied at A and B is shown in Figure 4.8. The parameters used in this study are 1500 rpm tool rotational speed, 2 mm/s welding speed and 27 mm tool shoulder diameter.

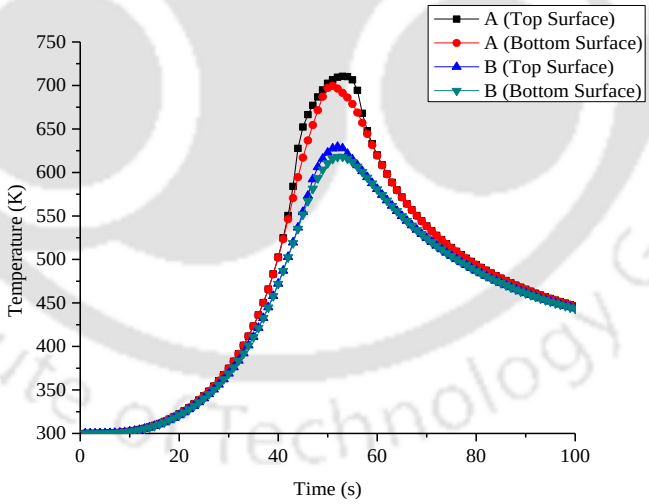

Figure 4.8: Top and Bottom surface temperature at A and B points.

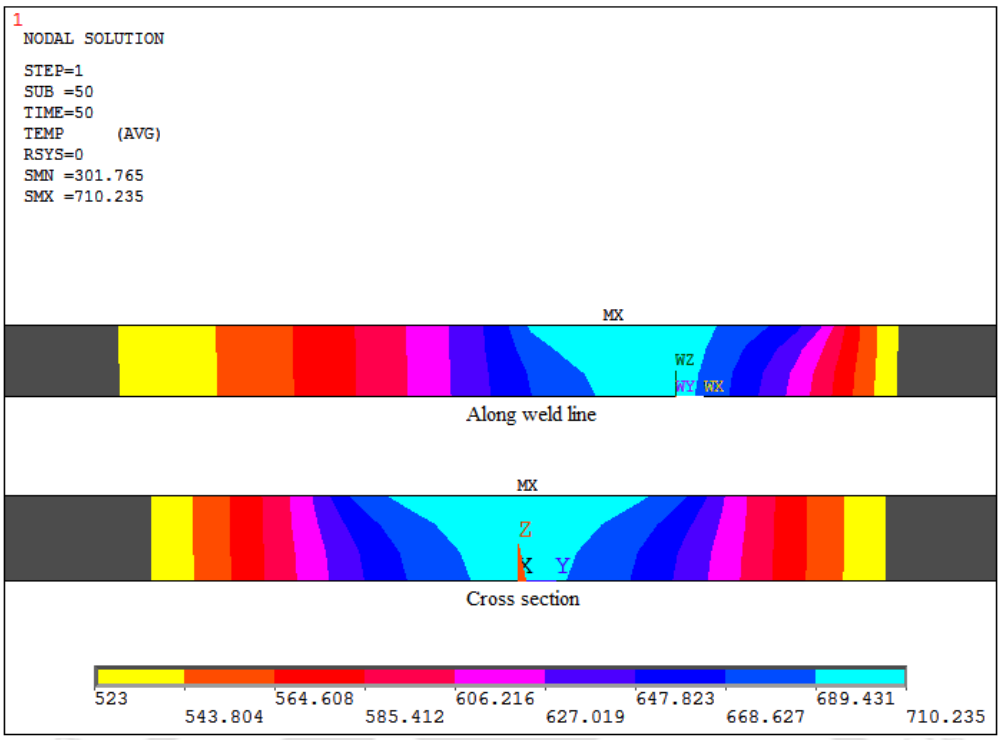

Figure 4.9: Temperature contours along the weld line and cross-section.

The A(top surface) shows a different temperature curve than others three curves because it lies under the tool shoulder and the heat loss starts only when the tool completely passed by that point. At the same time, the bottom surface lost heat due to conduction of the base plate. The heat loss from the top surface is very less compared to the heat loss from the bottom surface due to the base plate. The maximum temperatures of the top and the bottom surface of the point A are 710 K and 699 K while at point B the values are 629 K and 618 K. The temperature contour along the weld line and at the cross-section is shown in Figure 4.9.

4.7 Experimental details

The results of the simulations are validated by performing experiments for 6 mm AA6061 plate. The plate dimensions are taken the same as the simulations. The tool is rotated at 1400 rpm and the welding speed is taken 2.5 mm/s with a tool shoulder diameter 30 mm. A conical pin tool is used with base and tip diameter 6 mm and 3 mm respectively whereas the height of the pin is 5.75 mm. The tool used is fabricated by SS310 alloy. The tool material properties are given in Table 4.3.

Table 4.3: Physical properties of SS310.

Property	Value
Hardness, Brinell	160
Tensile strength, ultimate (MPa)	655
Tensile strength, yield (MPa)	275
Thermal conductivity at 100 $^{\circ}$C (W/m^2 K)	14.2

The K-type thermocouples are used to obtain the thermal profile data with a data acquisition system. Two thermocouples are applied at a distance of 20 mm from the centre line. The thermocouple employed at the centre of the plate is taken to validate the simulation results are shown in Figure 4.10. The peak temperature obtained in the experiment is 576 K while in simulation it is 582 K. The maximum variation obtained 5.53 % between the experimental profile and the simulation profile.

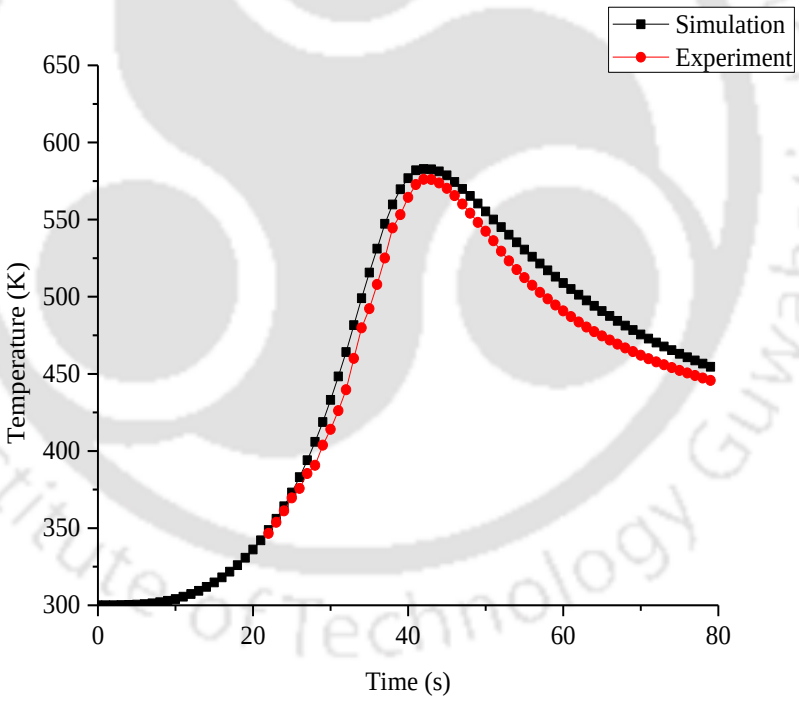

Figure 4.10: Comparison between numerical and experimental results.

4.8 Summary

In this chapter, the thermal transient analysis is performed and effect of rotational speed, traverse speed and tool shoulder diameter has been studied. It is found that the

peak temperature rise with tool rotational speed and tool shoulder diameter, however, it decreases with tool traverse speed. The significance of combined sticking and sliding heat generation is also studied in this chapter. It is found that the dominance of sticking heat generation increases at high tool rotation and traverse speed. The current analysis provides similar temperature distribution on both advancing and retreating side. So for validation, only advancing side temperature profile is taken from the experiments. In the next chapter, different laminar and turbulent material flow models are studied in ANSYS Fluent 14.0 and validated using the experiments.

Chapter 5

Material Flow Behaviour

5.1 Introduction

In the former chapter, the thermal aspect of FSW was studied. The effect of tool rotational, traverse speed and shoulder size was studied on the welding temperature profile of the plate. The significance of the sticking condition was realized in the conducted study. In this study a threaded tool is considered for the analysis and the material used is AA6061. The simulation has been carried out with appropriate boundary conditions. Moreover, thermal analysis has also been carried out along with the material flow. The analysis presented in this chapter shows the importance of material properties with three laminar models and one turbulent model. Temperature-dependent material properties are implemented to obtain the results of simulation which is carried out in ANSYS Fluent 14.0. In order to justify the approximations and boundary conditions employed in simulation, experimental validation of the same has also been carried out.

5.2 Modelling details

In this work, the finite volume model is employed for simulating the material flow behaviour of the FSW process. The tool geometry taken for the analysis is a conical threaded pin with a flat shoulder. The threaded geometry is taken in order to study the detailed material movement in the nugget zone. The threaded tool geometry provides better understanding and comparison of the material flow formed in different models. The plate material used for the analysis is Aluminium alloy 6061. The dimensions of the plate are 200 mm long, 150 mm wide and 6 mm thick i.e. 200 × 150 × 6 mm. A 25 mm diameter tool shoulder has been used in this study as shown in Figure 5.1 (a). The base diameter of the conical threaded pin is 6 mm and the tip diameter is 3 mm. The length of the pin is 5.75 mm having threads with pitch of 1.5 mm. The tool is incorporated into the model as a wall with 0.1 mm depression in the weld plate due to the plunging force during the welding. The weld plate is meshed using tetrahedral

elements. The mesh is refined near the tool pin region which is shown in Figure 5.1 (b). The analysis is performed using this model in ANSYS Fluent 14.0.

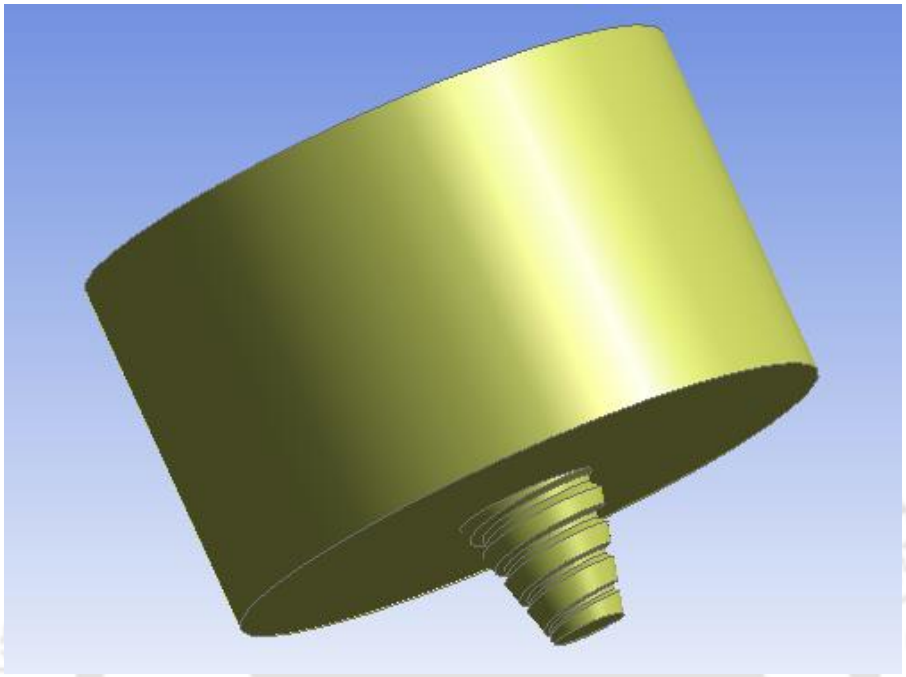

(a)

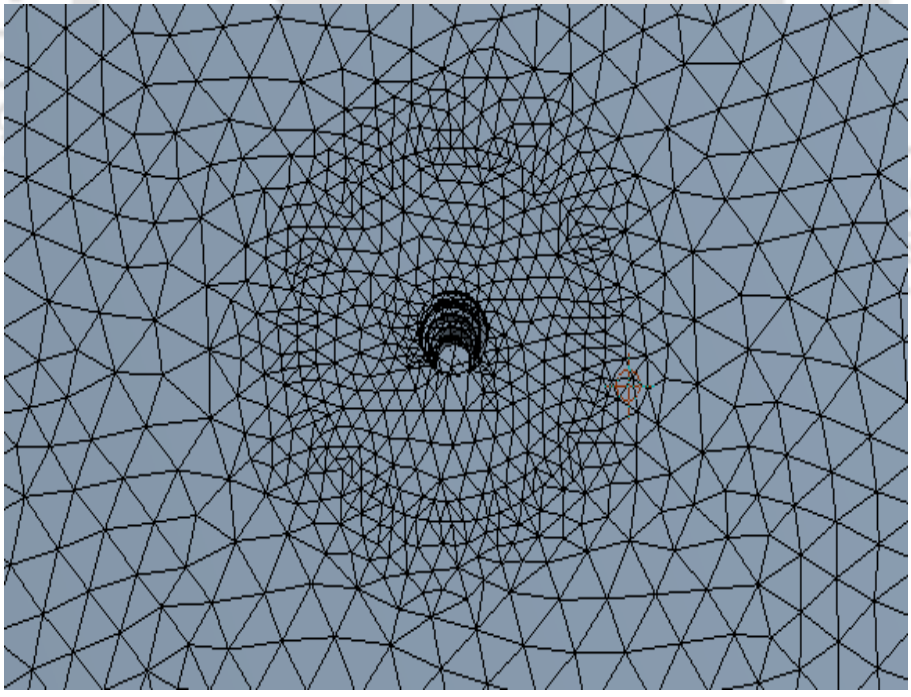

(b)

Figure 5.1: (a) The model of the tool and (b) the meshing and the tool impression in the plate.

5.3 Results and discussion

For the convenience of understanding, five planes have been considered to show the results as depicted in Figure 5.2. The planes 1, 2 and 3 are considered to lie at 0.2 mm, 3 mm and 5.9 mm from the top surface, respectively which are parallel to the top surface. The planes 4 and 5 are taken at the mid-section of the weld plate which is at weld line.

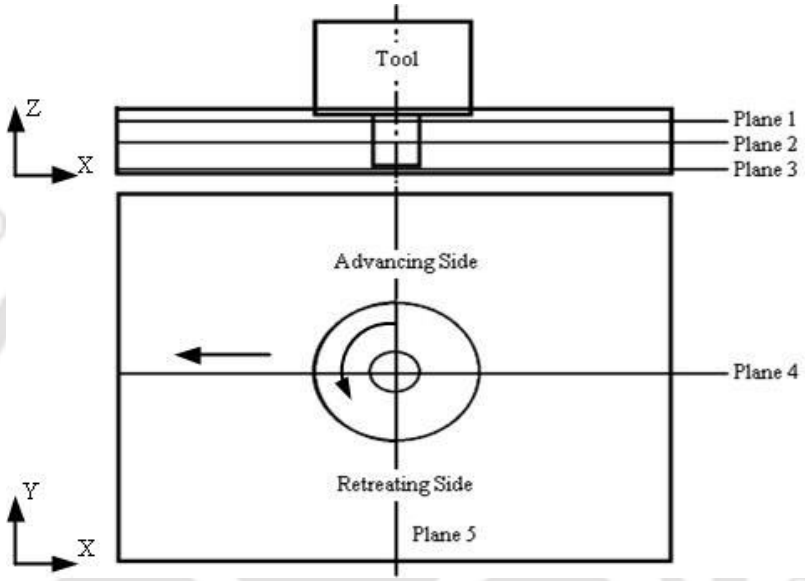

Figure 5.2: Planes location used for analyzing the material flow in the study.

For the initial analysis, the constant material properties have been taken. The specific heat is considered to be around 80% of the melting point temperature which is taken as 1100 J/kg-K. In the same way, the thermal conductivity and the viscosity of the material are considered 220 W/m-K and 1.3 kg/m-s, respectively. The material flow is assumed as laminar and therefore, the model used in the analysis is a laminar model.

At the tool surface, the maximum velocity attained is 1.76 m/s while the maximum velocity at the outer edge of the tool is 1.46 m/s. Figure 5.3 shows the top and front view of the material movement around the tool geometry i.e., plane 1 and 5. The Figure 5.3 (a) doesn't include the tool wall which only shows the workpiece material around the tool. The maximum velocity obtained in the material is 1.46 m/s towards the outer edge of the tool and on the top surface of the material. The Figure 5.3 (b) also shows that a swirl is formed by the movement of the material around the threaded tool pin.

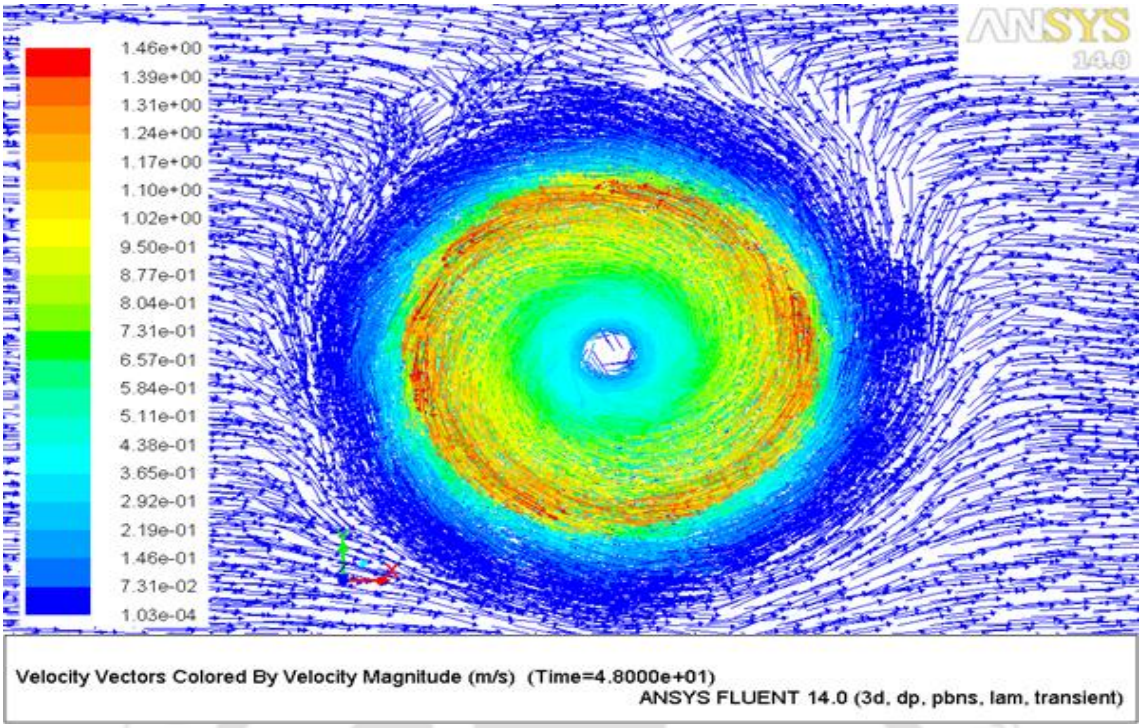

(a)

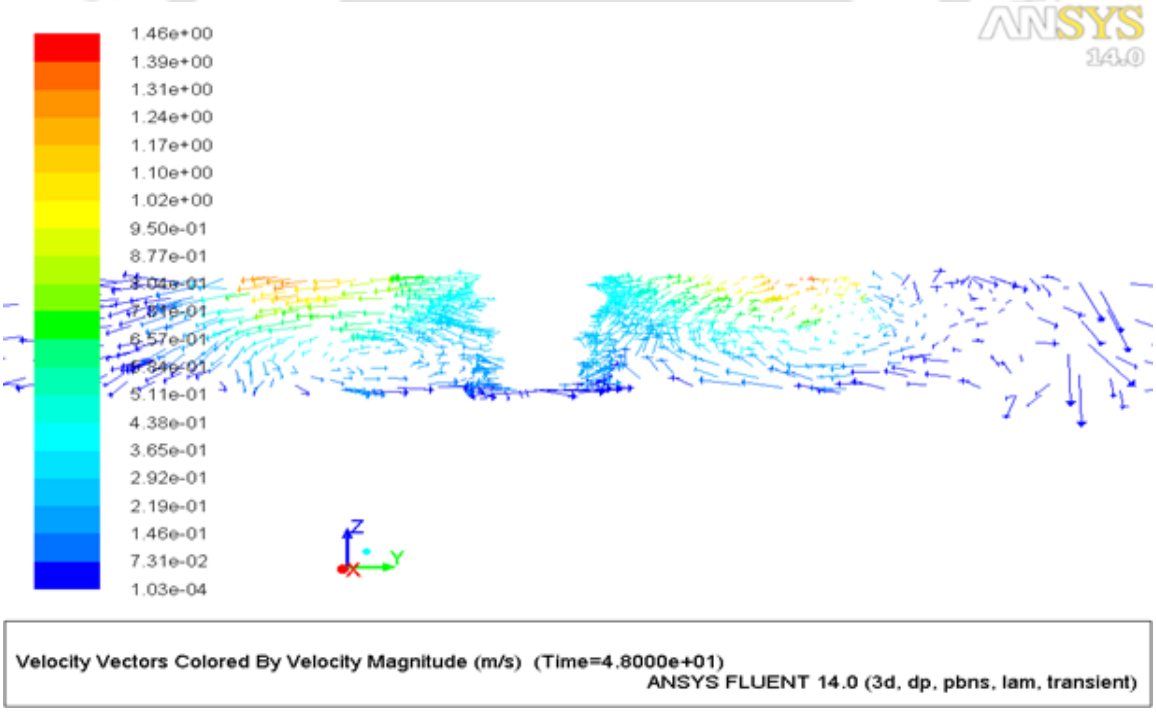

(b)

Figure 5.3: (a) Top view of the velocity vector and (b) cross-sectional view at the central axis of the tool.

The advancing side has this swirl on the top while on the retreating side the swirl is at the bottom end of the material. The swirls movement has very low velocity as compared to the material adjacent to the wall of the tool.

For further analysis, temperature dependent thermal material properties are considered. Consequently, the specific heat and the thermal conductivity are implemented as a function of temperature. The dependency of these thermal properties on temperature is earlier defined in section 3.5.4. Therefore, the Eqs. (3.69) and (3.70) are employed in the analysis. Moreover, the viscosity of the material is again taken as constant (1.3 kg/m-s) for this analysis. It is to note that the temperature dependent properties do not affect the material flow significantly. A similar type of vector plot is obtained for the velocities with a difference in thermal aspect and the temperature distribution in the material. The difference between the two approaches is shown in Figure 5.4 by thermal history of both the cases.

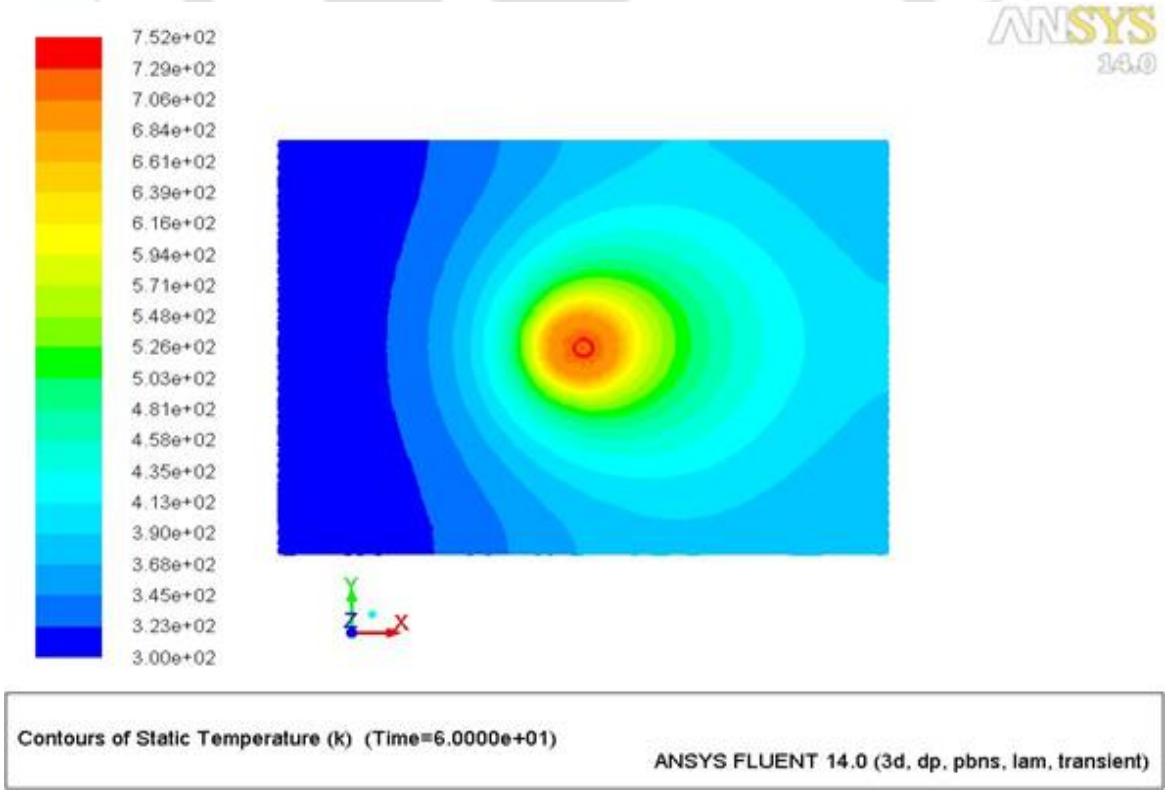

Figure 5.4a: Temperature profile with constant properties

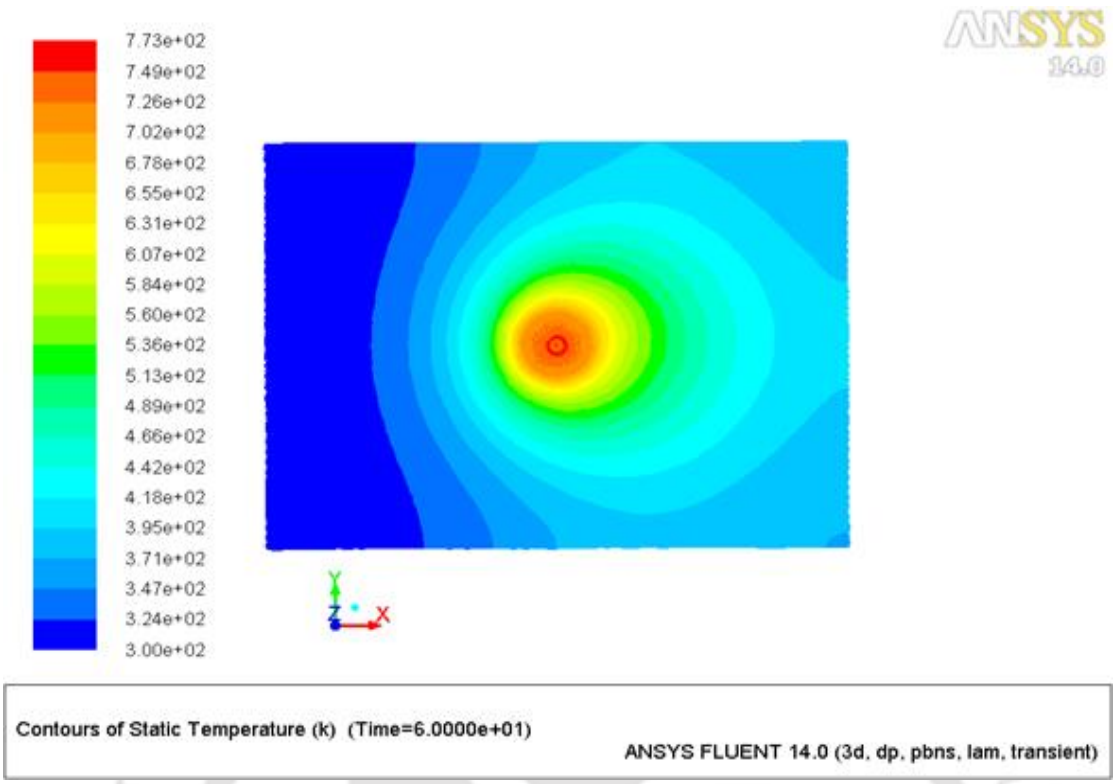

Figure 5.4b: Temperature profile with temperature dependent properties.

The peak temperature obtained with constant material properties is 753 K whereas in temperature-dependent case it is observed to be 773 K. From the above Figure 5.4 (a) and (b) it is observed that during the initial analysis, a lower temperature gradient is obtained in the case of constant material properties. On the other hand, with temperature dependent thermal material properties the temperature contours are more concentrated. The latter case resembles the realistic phenomenon much closely.

For further analysis, all temperature dependent thermal material properties along with viscosity are implemented with the help of a user defined functions (UDF) based on Zener-Hollomon equation given by Eqs. (3.71) and (3.72). The vector profile obtained in this case is different from the previously discussed cases. Since the viscosity is lower at higher temperatures, the regions with higher temperatures show maximum velocity. A maximum velocity of 0.392 m/s is obtained near the pin. The vector plot for this analysis is shown in Figure 5.5.

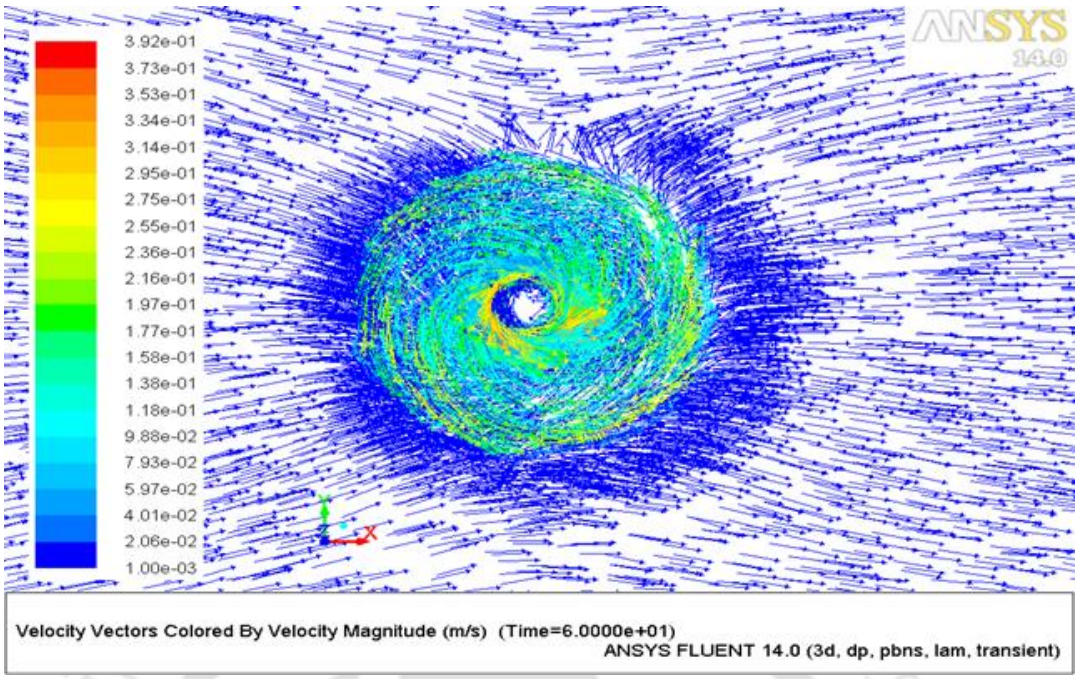

(a)

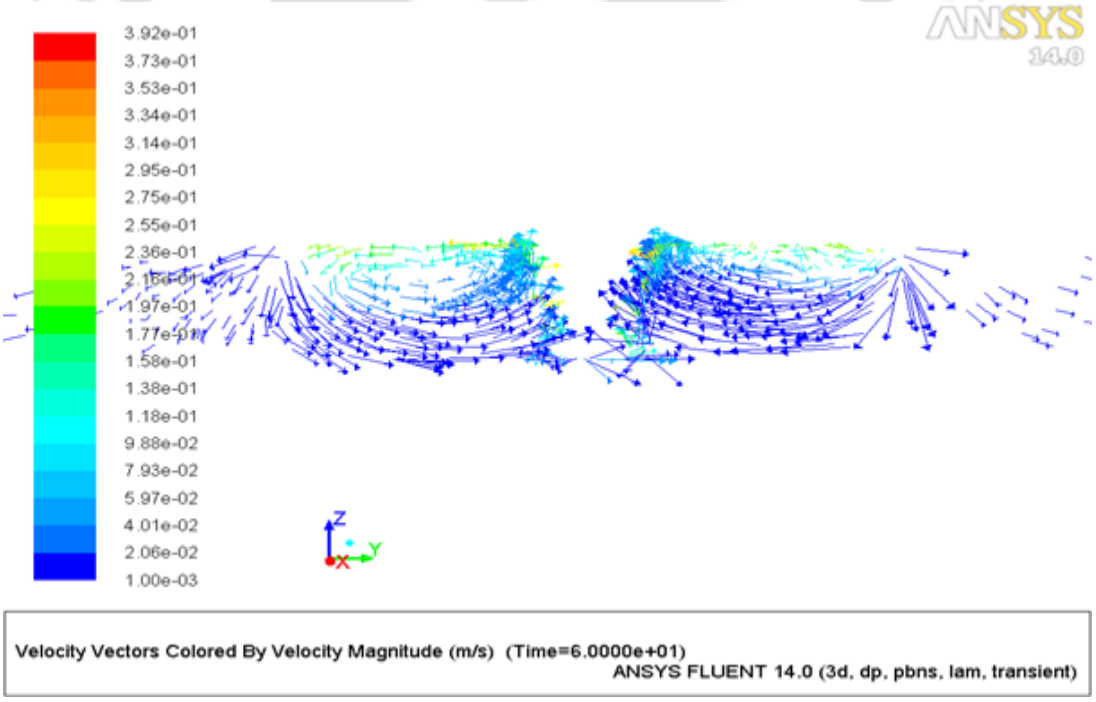

(b)

Figure 5.5: Velocity vectors plots at (a) plane 1 and (b) plane 5 showing top and cross-sectional view.

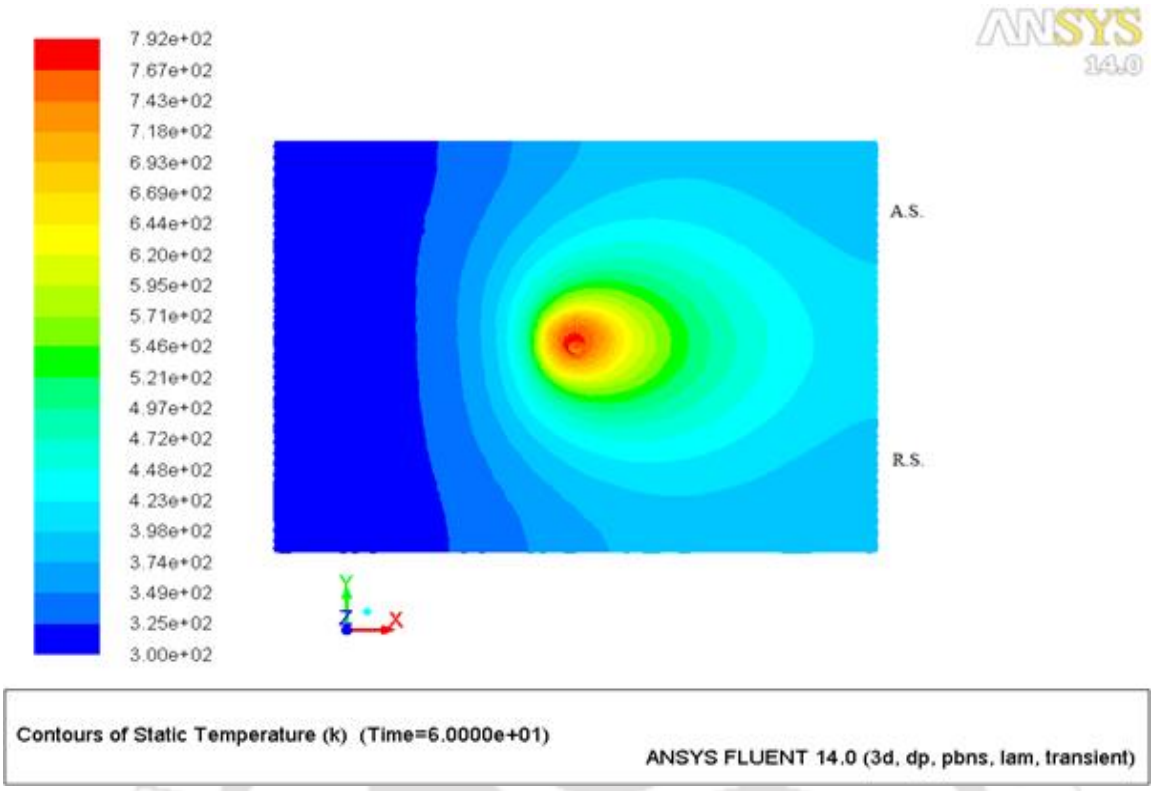

(a)

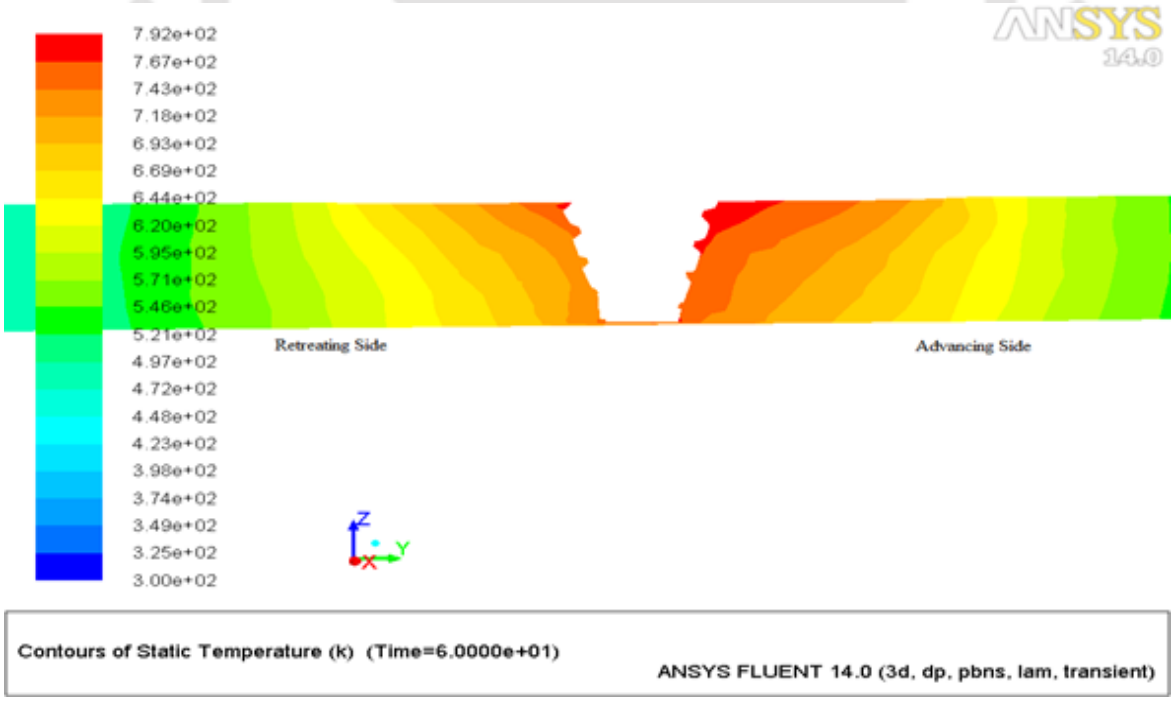

(b)

Figure 5.6: Temperature contour at (a) plane 1 and (b) plane 5.

The maximum temperature obtained in this case increases to 792 K which is 2.5% higher than the previous case. The heat is more concentrated in this analysis as

compared to previous ones. The temperature profile for the same is shown in Figure 5.6. In addition to that, heat generation is more towards the advancing side as compared to the retarding side.

The velocity vector plots at three sections of the material have been shown in Figure 5.7. The three sections are parallel to the top surface at a distance of 0.2 mm, 3 mm and 5.9 mm, respectively. The velocity drastically changes as observed from top to bottom. The first plane is quite near to the tool surface and therefore the material velocity is very high. The second plane lies in the middle of the material. Hence, the material velocity near the pin wall is high and gradually decreases away from the weld line. And the third plane is in between the tool tip and the bottom surface. The material deformation is significantly less in this plane.

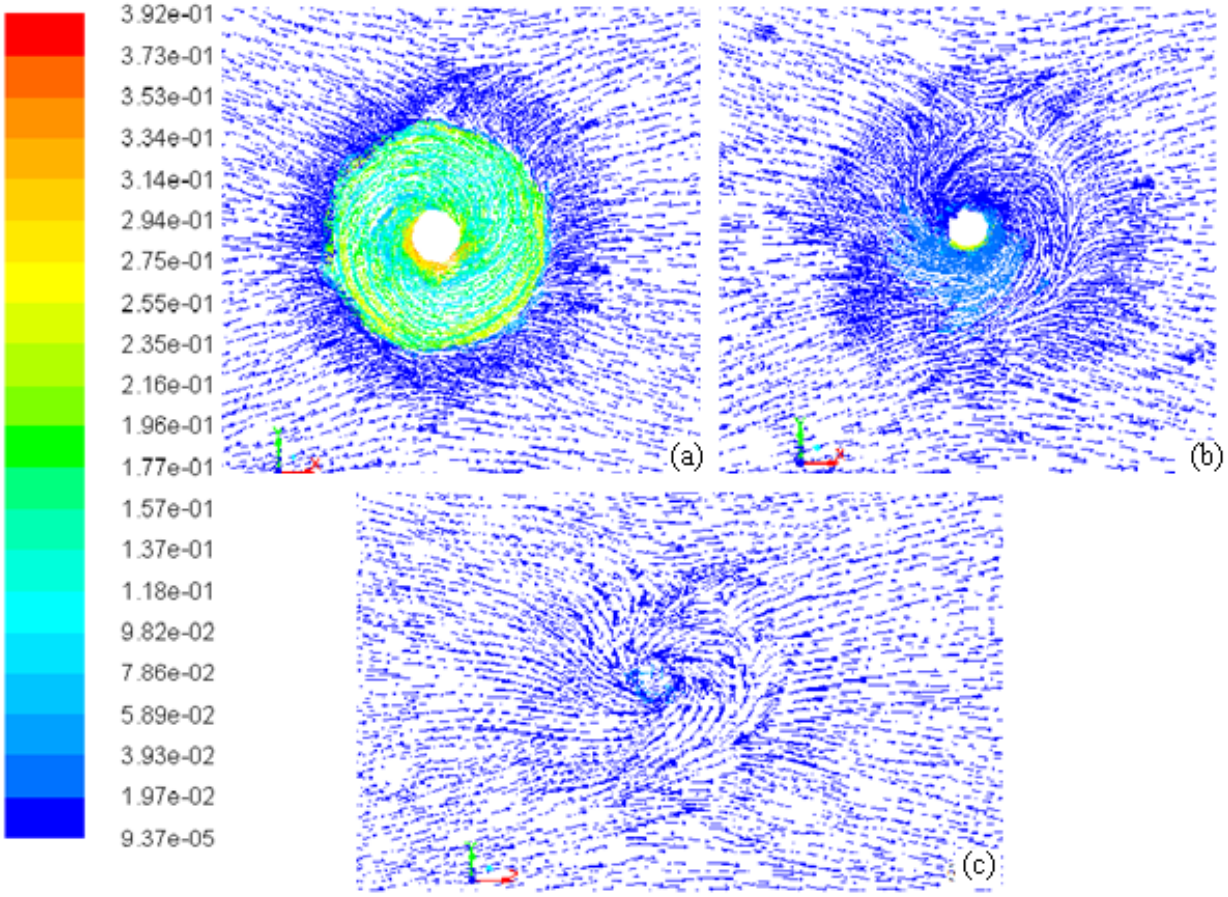

Figure 5.7: Vector plots at (a) 0.2 mm from the top surface (plane 1), (b) 3 mm from the top surface (plane 2) and (c) 5.9 mm from the top surface (plane 3).

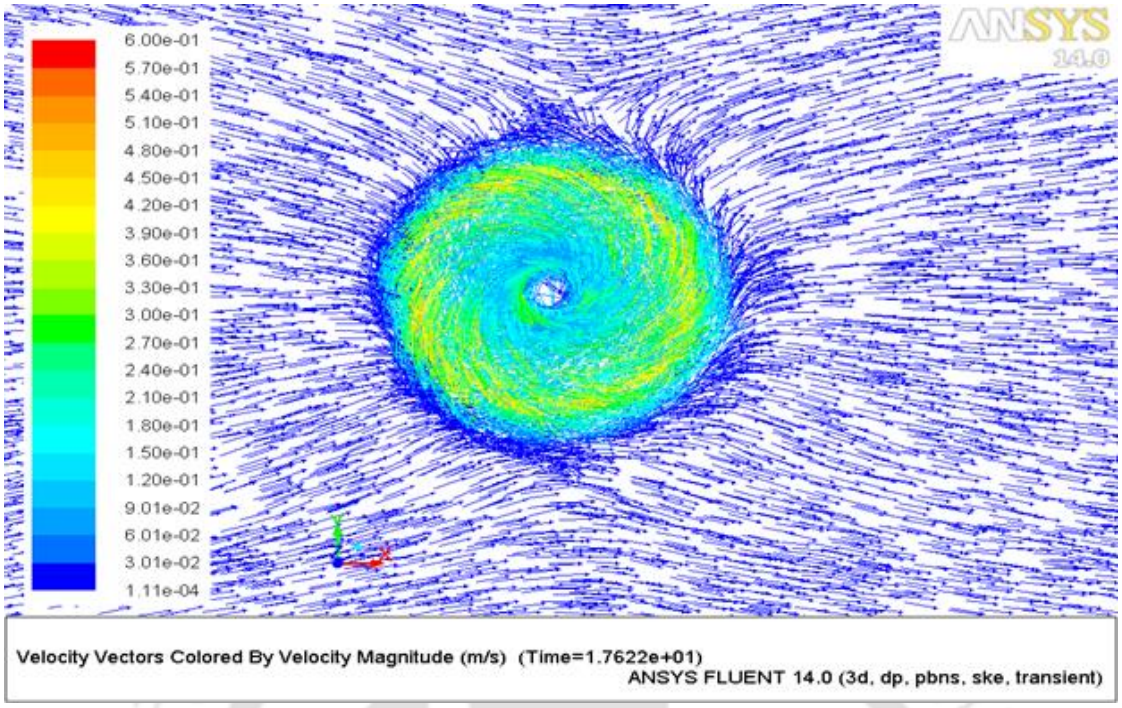

(a)

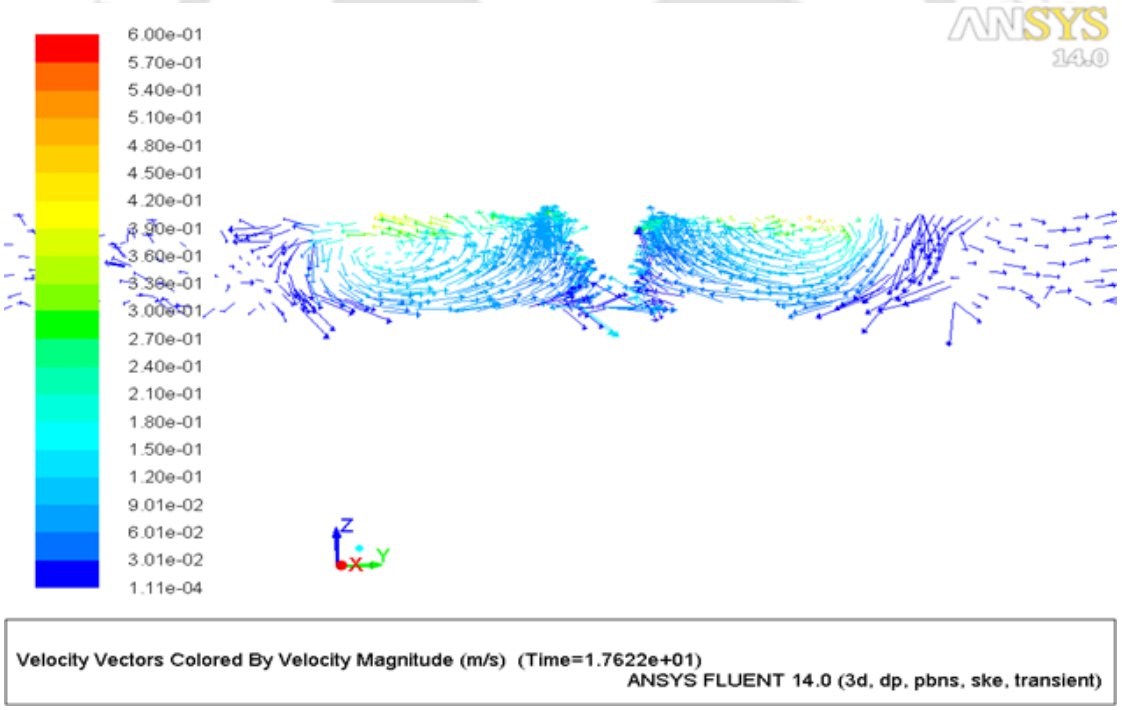

(b)

Figure 5.8: (a) Top view of the velocity vector and (b) mid-section view of the velocity vector using the turbulent model.

For further study, the same analysis has been performed using the turbulent model in contrast to a laminar model. The model used for the analysis is standard K-epsilon model with constants $C_{1\varepsilon} = 1.44$, $C_2 = 1.92$, $\sigma_k = 1.0$ and $\sigma_\varepsilon = 1.2$. The results obtained by this analysis are similar to that of the laminar case but the analysis takes approximately 40 times longer computational time. The maximum velocity obtained in this case is 0.6 m/s at one location in the region adjacent to the tool surface but the movements inside the material follow the same pattern as a laminar model. The turbulent model also shows the swirls around the pin. This movement of the material around the pin is a prominent feature in stirring. Figure 5.8 shows the material flow obtained with the applied turbulent model. The material is forced to move below the tool on the advancing side but on the retreating side, the material is pushed away from the tool.

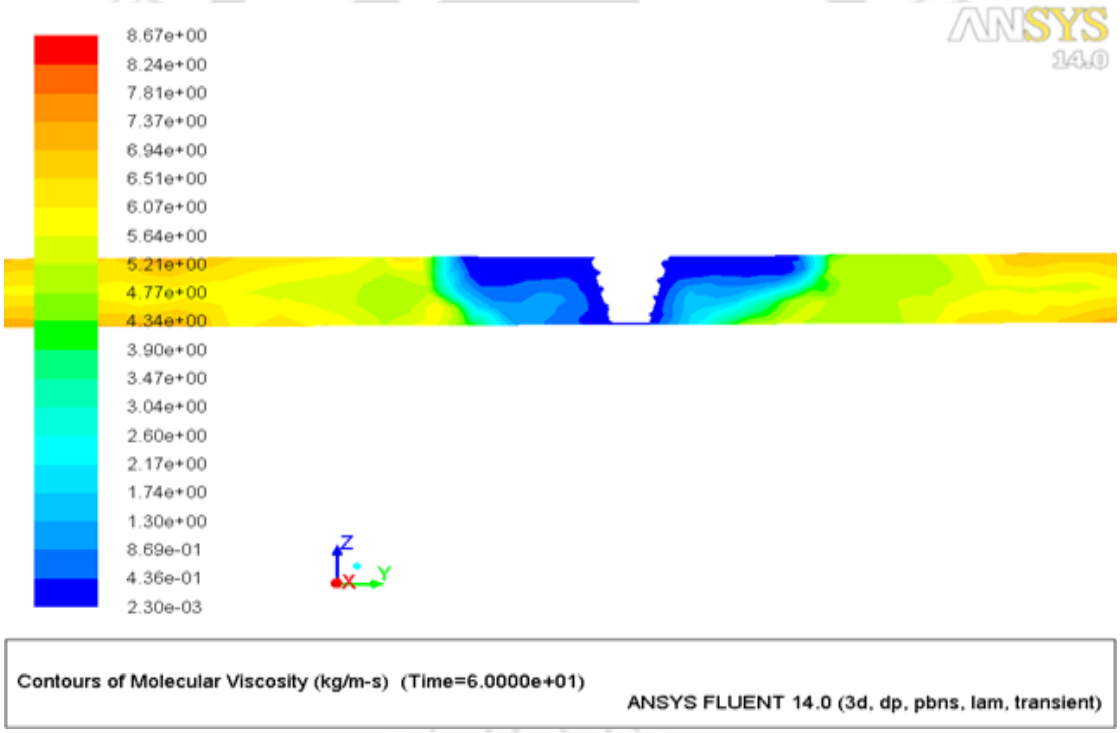

Figure 5.9: Viscosity variation implemented into the material.

The variations of viscosity are also studied and are shown in Figure 5.9. The viscosity is found to be lower near the pin region or towards the centre while it is high on moving outwards. A swirl has been observed in all the vector plots as the high speed rotating tool wall pushes the material outwards. These forces actually drive the low viscosity material to form swirl around the tool pin. The swirl obtained in constant viscosity analysis has got high magnitude and is bigger in size in comparison to

temperature dependent viscosity analysis. The temperature profile also varies with viscosity due to the flow of material. An asymmetry is also noted in the temperature distribution. The peak temperature obtained at the advancing side is 564 K while the maximum temperature obtained at the retreating side is 526 K. Both these reading are taken at a distance of 20 mm from the centerline. The observed variations in temperature with time have been shown in Figure 5.10.

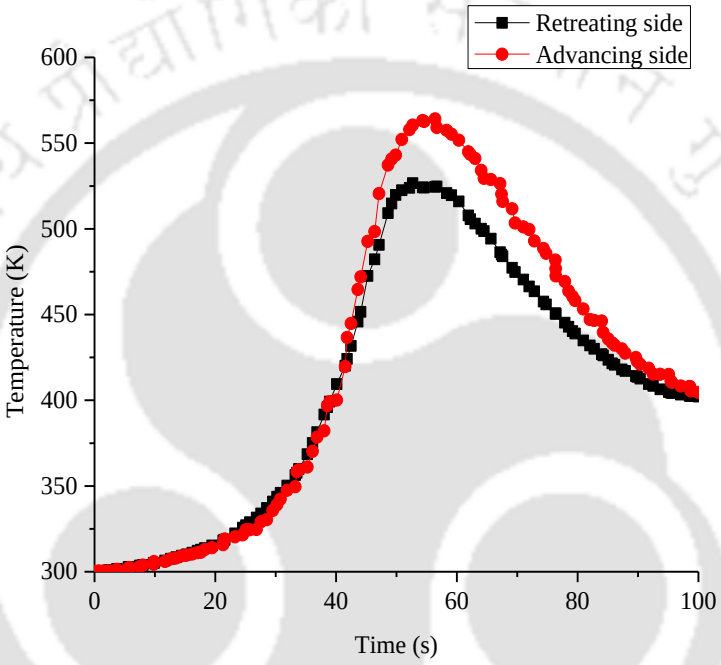

Figure 5.10: Difference in temperature profile for advancing and retreating side at a distance 20 mm away from the centre line.

5.4 Validation of model

For validating the model, experiments are performed to study the thermal history data. This thermal history is then compared with the thermal history obtained from the simulation. The material used for the experiments is 6 mm thick with a surface area of 200 mm long and 150 mm wide. The tool is rotated at 1100 rpm and the welding speed is taken to be 2 mm/s with a tool shoulder diameter of 25 mm with no tilt angle. A flat shoulder and conical pin with base diameter 6 mm and pin tip diameter 3 mm is used. SS310 alloy is used to fabricate the FSW tools. For the measurement of the temperature of the workpieces 1 mm diameter, K-type thermocouples are used. The

thermocouples are connected to the data acquisition system (Agilent-34970A) to record the temperature data. Two thermocouples are employed on both sides of the plate at the centre of the weld. A square butt welding with zero root gap is clamped into the horizontal bed. The milling machine with 7.5 hp capacity is used to perform the square plate butt joining of FSW shown in Chapter 3.

The experimental and simulation thermal profile at a distance 20 mm away from the weld line on the advancing and retreating side is shown in Figure 5.11. The peak temperature obtained in experimental study is 601 K while in case of numerical simulation it is 586 K on the advancing side. However, the maximum temperature obtained by the thermocouple is 558 K whereas, the 550 K is the maximum temperature obtained in the simulation on the retarding side. The temperature difference is observed in the experimental and computed readings, due to the assumptions made in the analysis. The environment temperature in the analysis is assumed to be 300 K in the simulation but during the experiment, it may get varied.

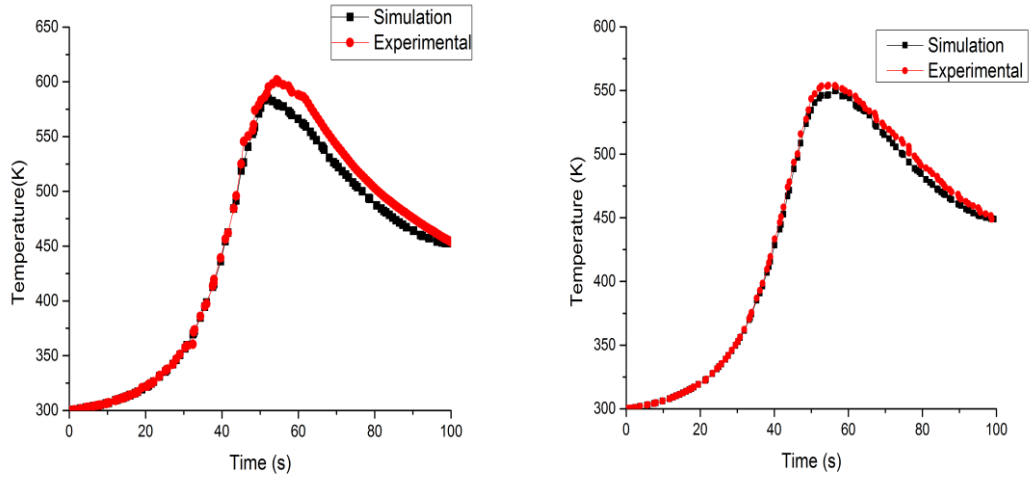

(a) (b)

Figure 5.11: Experiment and Numerical thermal profile comparison of a conical pin tool (a) advancing side and (b) retreating side at 1100 rpm and 2 mm/s welding speed.

5.5 Summary

In this chapter, different laminar and turbulent material flow models are proposed considering constant and temperature dependent thermal material properties. The

comparison of different models is shown in terms of temperature and velocity vector contours. The fastest and most accurate results are obtained from the laminar model with all temperature dependent thermal material properties. The proposed model also provides an accurate thermal profile on both advancing and retreating side. The material flow models provide the information about the way in which the material transports under a high rotating tool in FSW. The velocity vortex is noted on both the side of the welding. The most accurate model is used for further analysis of the influence of tool pin geometry and effect of the process parameter on material flow in the next chapter.

Chapter 6

Material Flow Behaviour for Different Pin Profiles

6.1 Introduction

In the last chapter, different material flow models were proposed for the study of material movement around the pin. The laminar flow model with temperature dependent material properties was the most efficient among the proposed ones, in terms of computational time and experimental matching. So, the same model is used for the further study to analyze the significance of tool geometry. Since every tool moves the material in a different manner so the knowledge of tool geometry effect on the material flow is inevitable. In the current study, seven different types of tool geometries are chosen and their effects on material flow are studied on deformation zone. The appropriate boundary conditions are used in the simulations to meet the real conditions. The analysis is performed on AA6061 in ANSYS Fluent 14.5. Based on that, the thermal temperature distributions, vector plots and the effect of rotation directions of a threaded tool are also studied.

6.2 Modelling details

In this work, Aluminium alloy 6061 plates are used to perform a finite volume model simulation of a butt joint FSW. Different tool geometries are used to weld 200 mm long, 150 mm wide and 6 mm thick plates. Tool shoulder size and pin length are kept constant for all cases i.e. 25 mm shoulder diameter and pin length 5.75 mm. The different pin geometries used in the current analysis is shown in Figure 6.1. The tools are implemented in the form of wall into the material plates that are meshed using the tetrahedral elements with a coarse mesh which are further refined near the tool region as shown in Figure 6.2. The minimum edge length of the element is taken as 0.3 mm in the tool region.

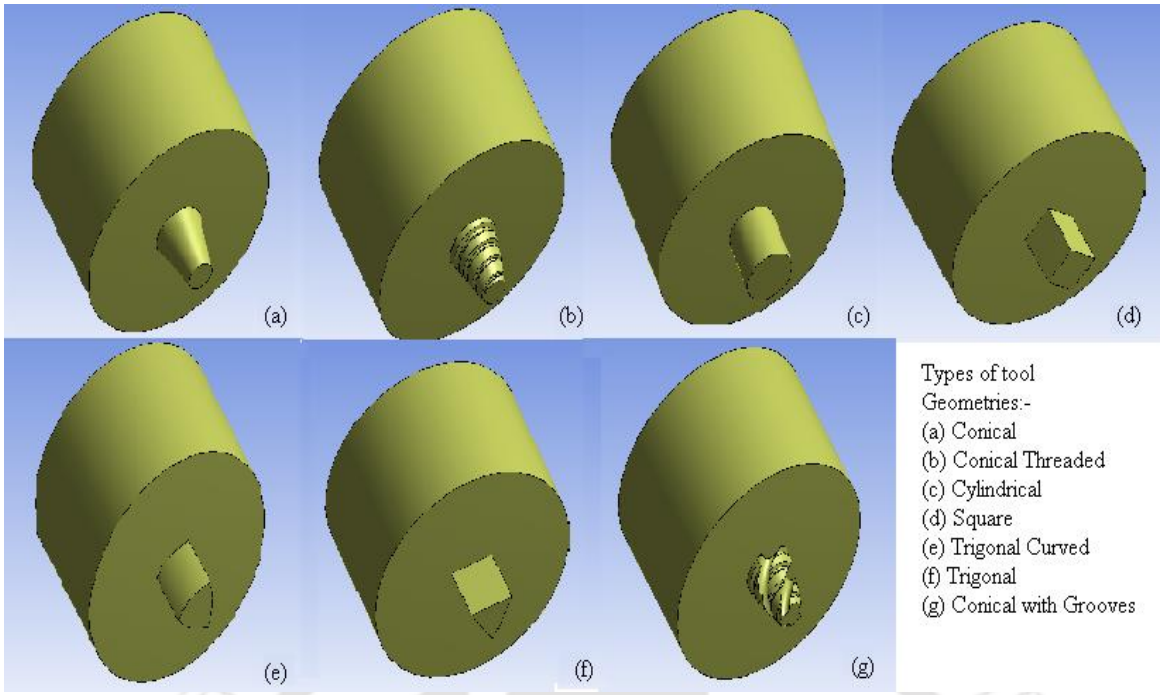

Figure 6.1: Different types of pin profiles used in the analysis.

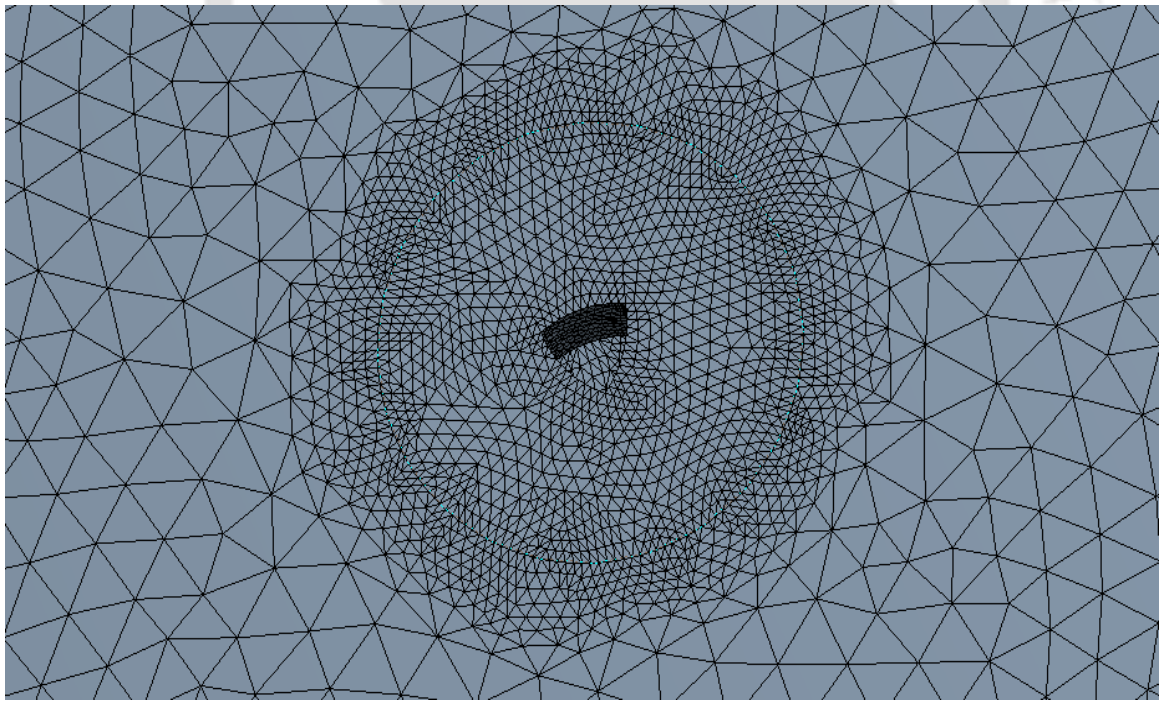

Figure 6.2: An oblique view of the mesh type used for the analysis where the finer tetrahedral elements are used in the tool wall region to capture more information under the tool.

6.3 Results and discussion

The thermal-flow coupled models are used in the current analysis. Seven different tool geometries are considered to find out the effect of tool pin profile on the material flow during the welding. The temperature distribution is achieved by the thermal analysis on the workpieces while the material movements inside the plate are provided by the flow analysis. In the current study, the same process parameters are given in each analysis to achieve a better comparison among all the cases. The welding is performed along X-direction and the advancing side (AS) and retreating side (RS) is on the positive and negative Y-directions respectively. The tool rotation axis is considered as origin with depth of the plate is taken along negative Z-direction as explained in section 3.5.1. All tool geometries are rotated with 1100 rpm and 2 mm/s tool travelling speed.

It is observed that AS has higher temperature than the RS. The peak temperature is obtained on AS which is 35-40 K higher than the RS. The highest peak temperature is obtained from the cylindrical pin geometry while the lowest peak temperature from the conical pin geometry. The peak temperature values are given in Table 6.1.

Table 6.1: The peak temperature obtained during the analysis.

Tool pin profile	Peak Temperature (K)
Conical	779
Conical Threaded	801
Cylindrical	893
Square	830
Trigonal with Curvature	828
Trigonal	794
Conical with Grooves	801

The temperature variation on moving away from the weld line for all seven geometries is shown in Figure 6.3. The temperature variation at a distance 20 mm away from the weld line is shown in Figure 6.4.

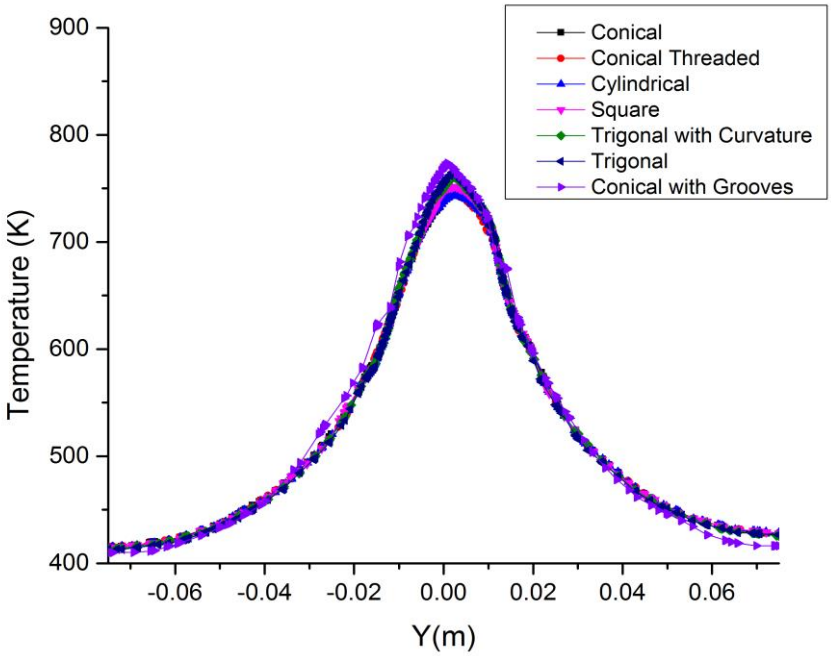

Figure 6.3: The temperature variations at 0.1 mm above the bottom surface of the plate for all cases on AS and RS. The Figure is showing the temperature drop on moving away from the weld zone where the positive and negative values of Y represent the AS and RS respectively.

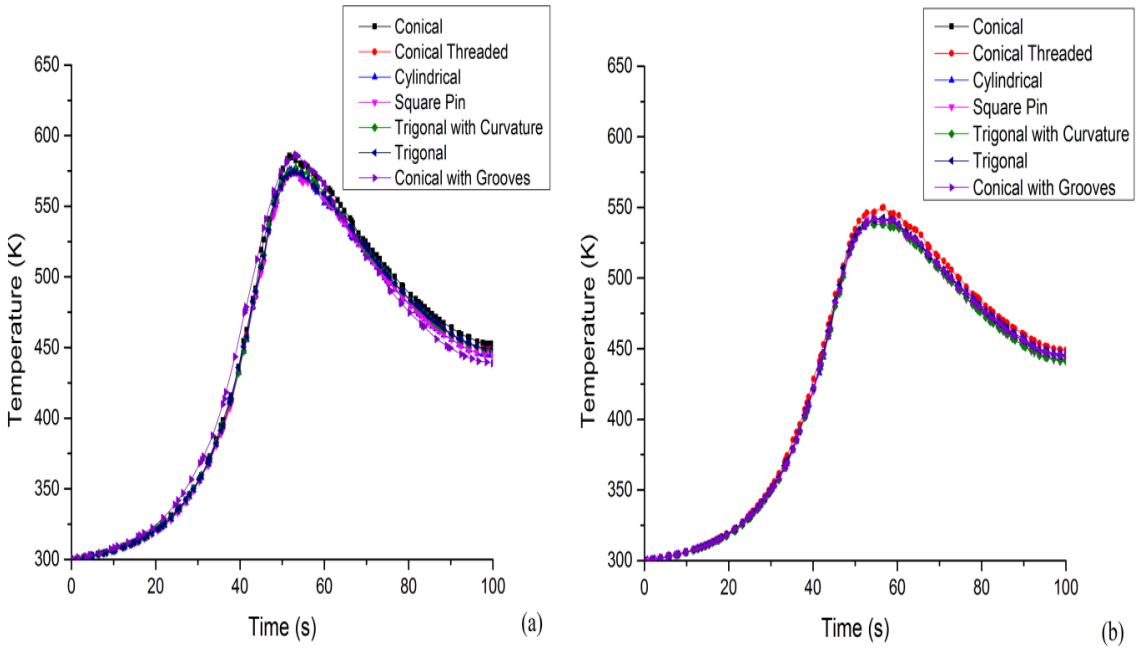

Figure 6.4: Temperature variations with time for all the geometries at 20 mm away from the centre line on (a) advancing side and (b) retarding side.

The temperature data obtained at a distance 20 mm away (AS and RS) from the weld line do not show any significant differences in all the cases as evident from Figure 6.4. The temperature values obtained in this case are extremely close to each other for all tool pin profiles. The temperature values are obtained at the points taken on the top surface of the weld plate over the mid-section of the plate on either side of the weld line. The velocity vector plot on the tool surface is shown in Figure 6.5.

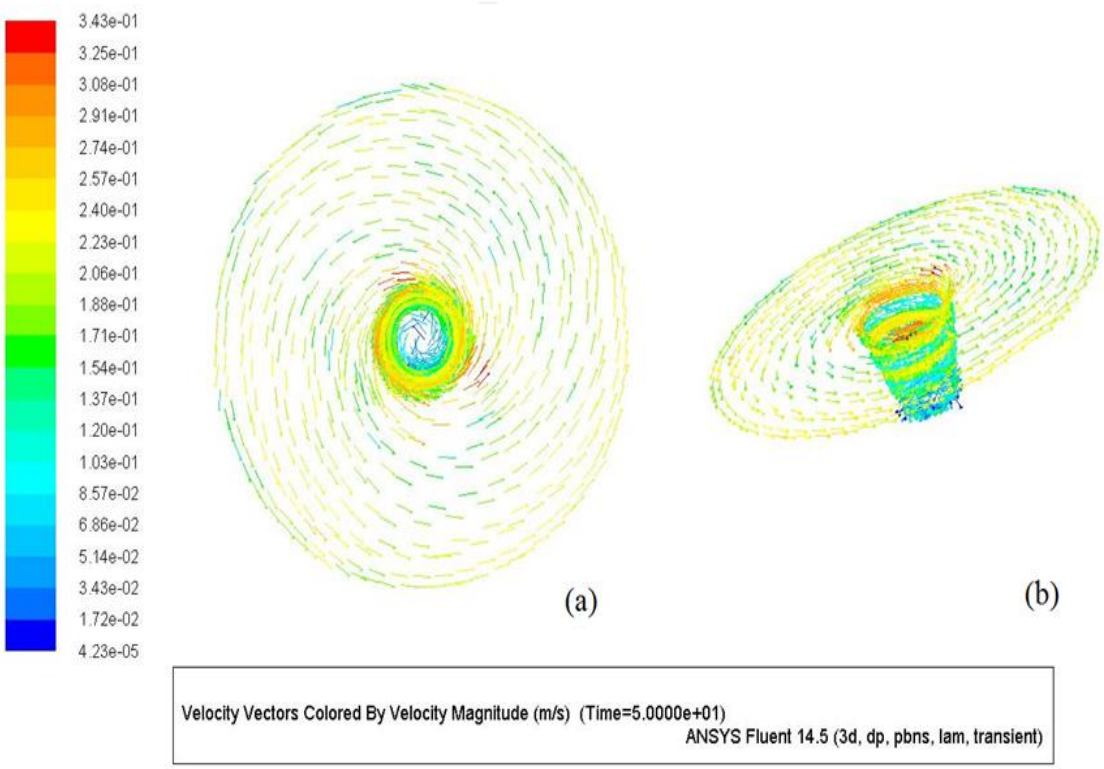

Figure 6.5: The velocity vector plot of the tool wall for conical threaded pin geometry (a) top view and (b) inclined view.

Though the tool shoulder and the pin, both affect the material flow, the material movements influenced by the pin is studied the current analysis and hence, the tool shoulder geometries are taken to be constant for all the cases. The vector plot on the tool shoulder surface of conical threaded pin geometry is shown in Figure 6.5 (b). The material movement caused by the tool shoulder is the same in all the cases which are shown in Figure 6.5 (a).

The maximum material velocity is attained at the pin base as the viscosity of the material decreases due to higher temperature values in that region. The velocity of the material is higher at the outer edges of the shoulder in comparison to the remaining surface of the tool shoulder surface except for the probe base region. The higher velocity values are obtained along the tool surface inside the material. The tool rotation enforces the softer material near the weld line to move radially outwards while the pin guides the material towards the shoulder that leads to helical wave formation inside the deformed material around the tool. The velocity vector profile in all direction around the tool is shown Figure 6.6.

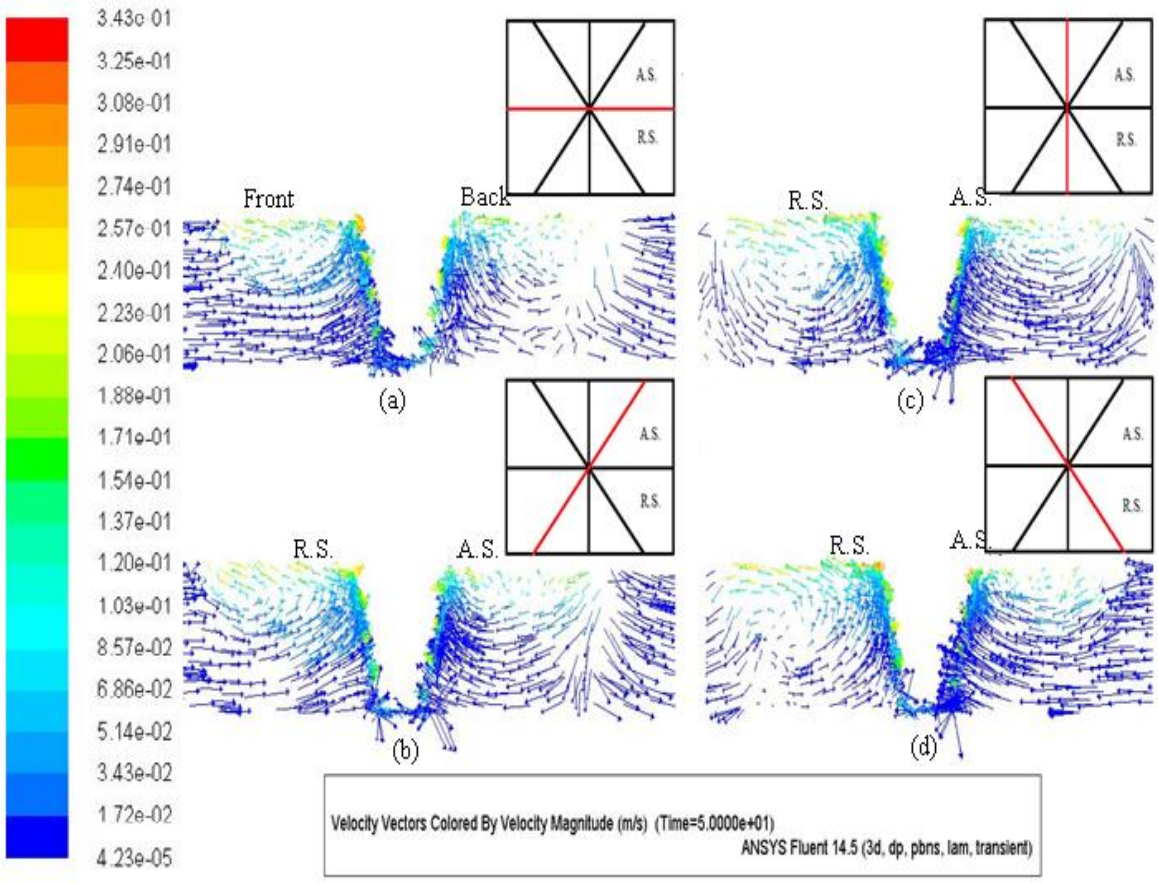

Figure 6.6: Velocity vectors around the pin for conical threaded pin profile at all 8 directions around the pin at 50 s of the welding time.

It is observed that the shoulder controls the lateral movement (i.e. along X and Y direction) whereas pin deals with the upward and downward movements (along Z direction) of the material as evident from Figure 6.6 (a). On moving away from the weld line, the deformation zone decreases and diminishes over the edge of the shoulder. The material deformation zone is small because of the higher viscosity of the material in that region due to the lower temperature values. The deformed material circulates on the front side of the tool as the shoulder rebound the soft material back in –X direction. Whereas, the back side of the tool has more deformation as viscosity of the material is much lower due to high temperature. The front side of the tool is the unwelded portion while the back side is the welded one. The deformation under the tool shoulder increases in the RS as the viewing plane is rotated by 45° in anticlockwise direction as shown in (b). The vector plot perpendicular to the weld line is shown by (c) and the vector plot at an angle 135° anticlockwise to the weld line is shown by (d). More deformation zone is found on RS in comparison to the AS which is influenced by the tool movement and the welding direction. The material on the AS flows in –X direction whereas the material movement direction is +X on the RS. The shape and size of the pin of different tool geometries cause the material to behave differently. The material movement along thickness (along Z direction) for all tool pin geometries is shown in Figure 6.7.

The material movement caused on front and the back side of the tool by all pin geometries along the weld line are shown here. Some similarities are found in the vector plot with the geometries with round pin i.e. in case of (a, b, c, e and g) on the front side of the tool. However, the pin geometries with flat surfaces are acted in a different manner i.e. (d and f). The round pin geometries push the material upward and thus help the soft material to form a circulating movement under the tool shoulder. Whereas, the flat pin geometries has reversed the material flow direction and do not support any circulated movement of the soft material. The flat surface of the tool pin geometry cause material accumulation which may lead to higher force generation on the tool. Whereas, the round pin geometries support the movement caused by the shoulder and hence lead to a smoother flow of the material.

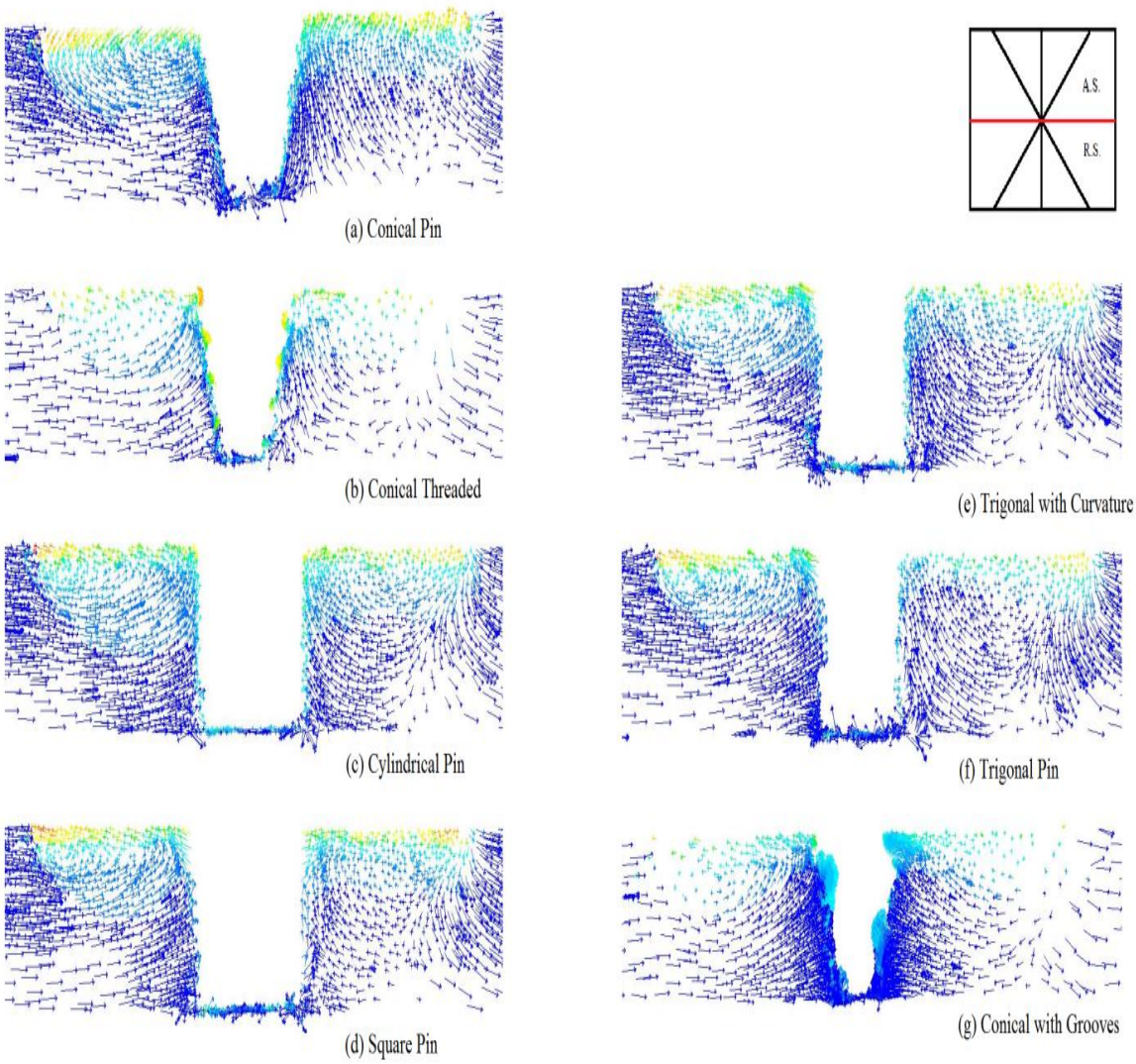

Figure 6.7: The vector plots showing the material movement under the tool shoulder on front and back sides (along X direction) of the tool.

The maximum and minimum velocities in a plane perpendicular to the weld line for all three directions are given in Table 6.2. It is seen that the maximum and minimum X velocity i.e velocity along the weld line do not change with the pin profile but the distribution pattern of velocities, changes with the pin profiles as shown in Figure 6.8. The material movement towards the pin and the shoulder is affected by the pin profile i.e. along the thickness (Z direction) as evident from the Figures 6.9 and 6.10.

Table 6.2: Maximum and minimum velocities perpendicular to weld line.

Tool Pin Profiles	Plane perpendicular to welding direction					
	V_x (m/s)		V_y (m/s)		V_z (m/s)	
	Minimum	Maximum	Minimum	Maximum	Minimum	Maximum
Conical	-1.416	1.415	-0.032	0.028	-0.012	0.023
Conical Threaded	-1.396	1.383	-0.044	0.048	-0.008	0.031
Cylindrical	-1.423	1.398	-0.032	0.026	-0.011	0.030
Square	-1.407	1.405	-0.037	0.036	-0.009	0.022
Trigonal Curved	-1.415	1.415	-0.029	0.033	-0.011	0.019
Trigonal	-1.426	1.415	-0.038	0.030	-0.014	0.012
Conical with grooves	-1.428	1.426	-0.058	0.063	-0.004	0.076

The threaded tool provides more deformation area in the AS in comparison to the plane conical profile as evident from the velocity profile contours shown in Figure 6.8 (a, b). The material movement is faster in case of threaded pin profile while the mechanically affected areas for both the threaded and plane pin profiles (a, b) are same. However, the lateral material movement for the plane conical profile is much lower than the threaded pin profile shown in Figure 6.9 (a, b). The velocities values obtained for upward and downward movement caused by the threaded pin are higher than the plane conical pin and are much nearer to the pin boundary as shown in Figure 6.10 (a, b). The maximum upward velocity magnitude (i.e. V_z) is obtained in the pitch region of the threaded pin geometry.

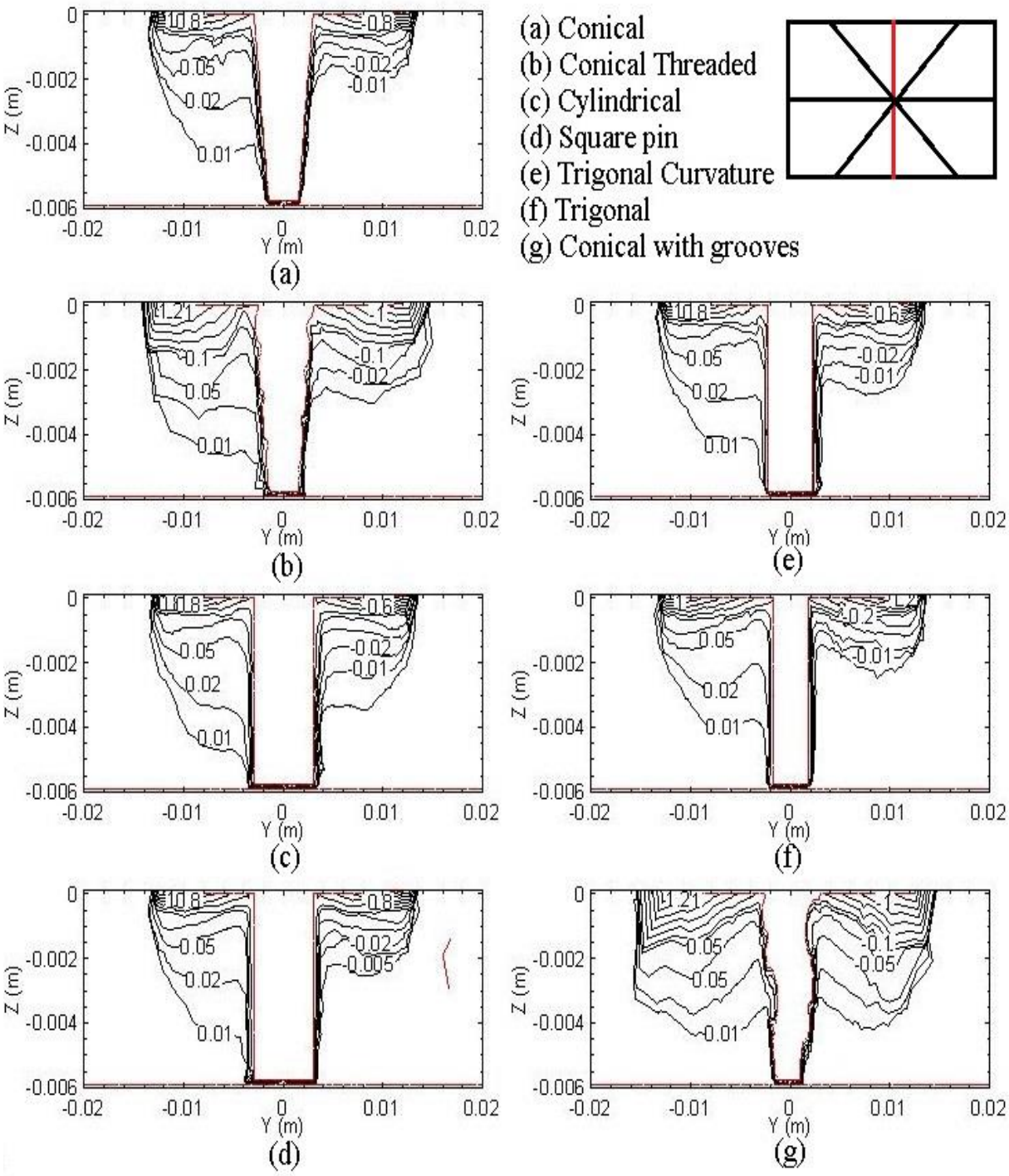

Figure 6.8: Velocity (m/s) profiles in direction of welding i.e. along X direction (V_x) of all seven geometries. The cross-section view shows the RS by -Y whereas, the AS by +Y of the material.

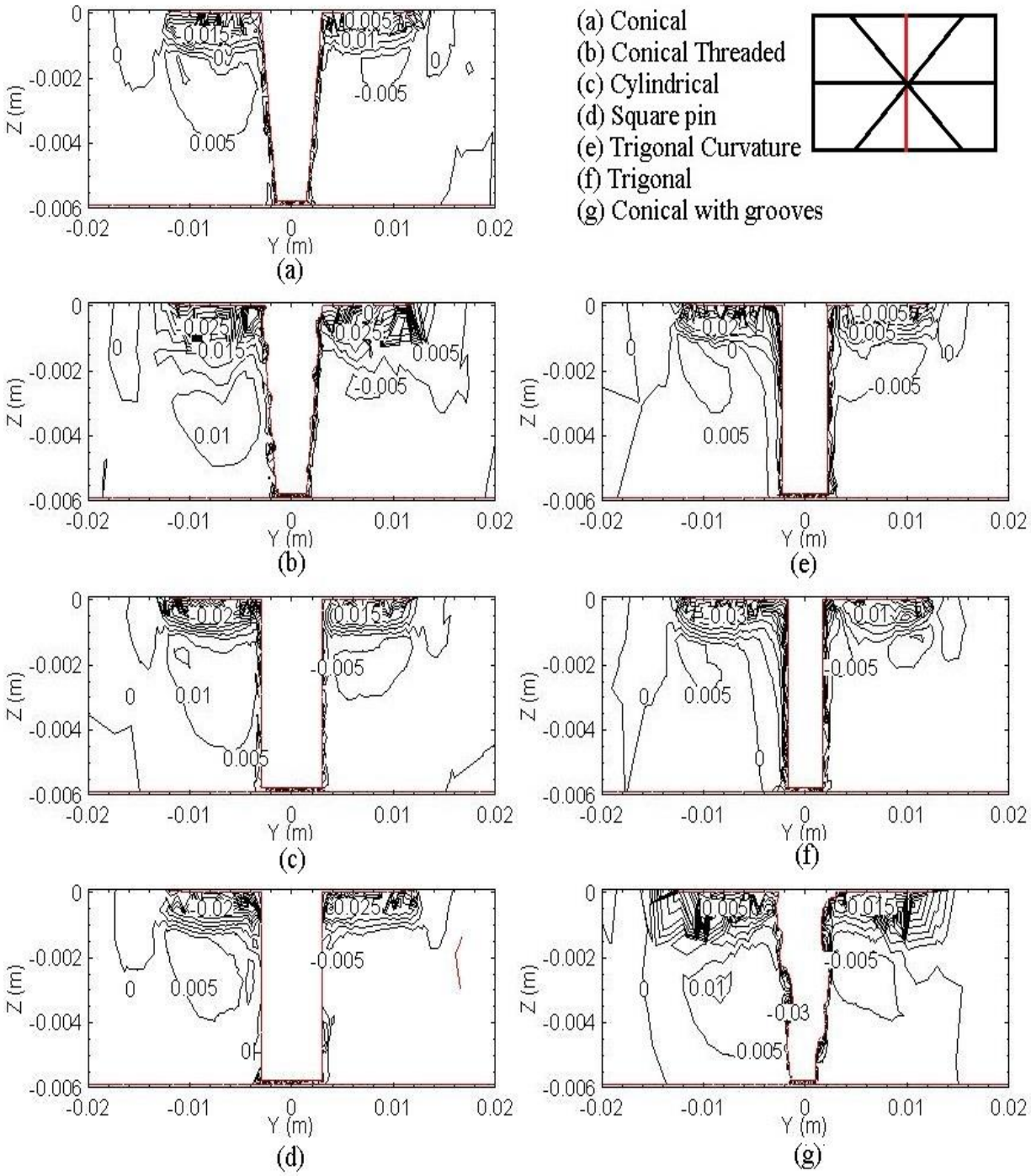

Figure 6.9: Velocity (m/s) profiles of the material movement towards and away from the pin i.e. Y direction velocity component (V_y) for all seven geometries.

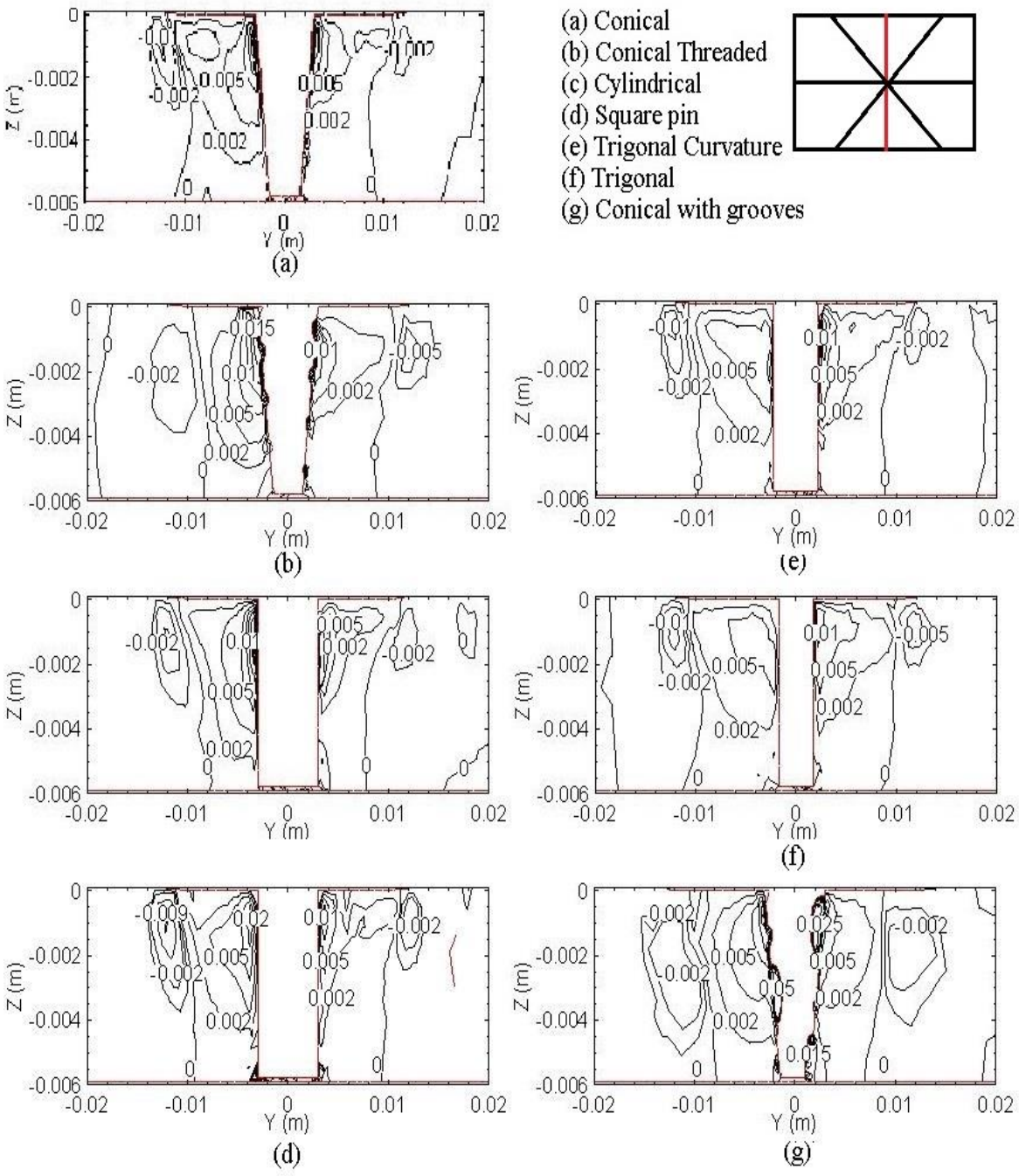

Figure 6.10: Velocity (m/s) profiles for upward and downward material movement along the height pin probe i.e. Z-direction velocity component (V_z) of all seven geometries.

Among the all pin profiles the maximum lateral (V_y) and upside material velocity magnitude (V_z) are provided by the conical with grooves pin profile, which is much higher than the other pin profiles as the viscosity of the material is low inside the groove region due to higher strain and temperature.

The cylindrical pin and conical pin produce identical velocity contour on RS but on the AS the contour is found to be different due to higher deformation caused by the cylindrical pin. Whereas, the flat pin profile i.e. trigonal and square show similar longitudinal velocity (V_x) profiles but the lateral material movement (V_y) is found to be more in square pin profile. For square pin profile, the difference of maximum upward and downward velocity is much higher in comparison to the trigonal pin profile.

For circular pin profile, the mixing of the material is better near the probe base region while the flat surface profiles do not provide lateral and upside material movement. The flat trigonal and the curved trigonal pin tools have a slight difference in the velocity contour profiles. The curved trigonal pin tool has more deformation zones in comparison to the flat surface trigonal pin geometry tool. The material movement on a plane perpendicular to the weld line is shown in the Figure 6.11.

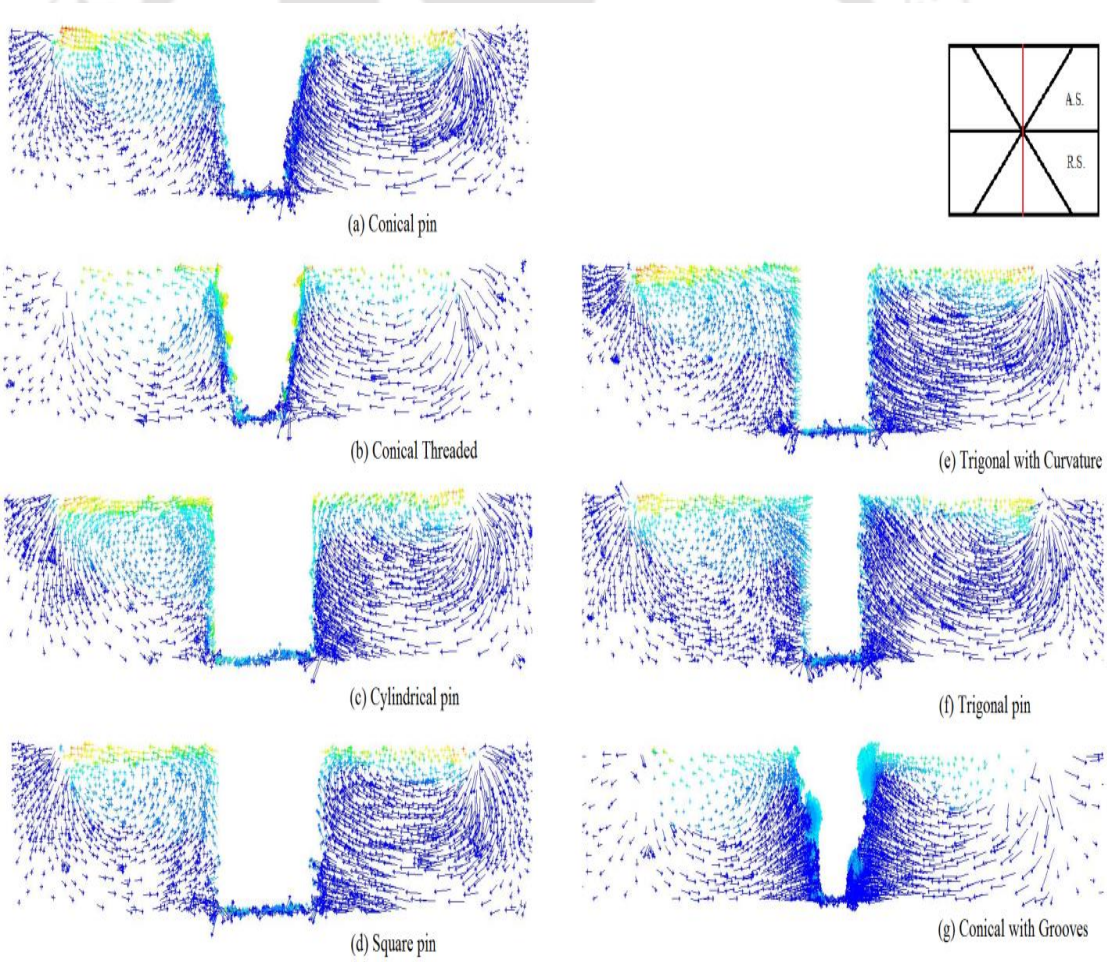

Figure 6.11: The vector plot of material movement perpendicular to the weld line i.e. cross section of the welding at 50s.

The vortex formed by the helical movement of the material is observed on the RS in all the cases but the vortex has different origins for different tool geometries. The vortex form by the conical pin i.e. in Figure 6.11 (a) is just under the extreme edge of the tool shoulder but in case of conical threaded pin i.e. in Figure 6.11 (b), the vortex is closer to pin and well below the tool shoulder surface. However, on the AS, there is no significant difference found in the deformation region in all the cases. In context of total deformation, the maximum deformation zone is formed by the cylindrical pin geometry i.e. in Figure 6.11 (c) while the lowest deformation zone is formed by conical with grooves which are observed in Figure 6.11 (g). In case of threaded tool geometries, it is observed that the maximum material movement took place around the pin only and the pitch of the tool pin is acted as channels for the material movements and thus the major material movement or the deformation takes place in the thread pitch of the pin. In such cases, a better material mixing is obtained near the weld line. The stream contour of the material flow of conical pin geometry at plane 2 is shown in Figure 6.12.

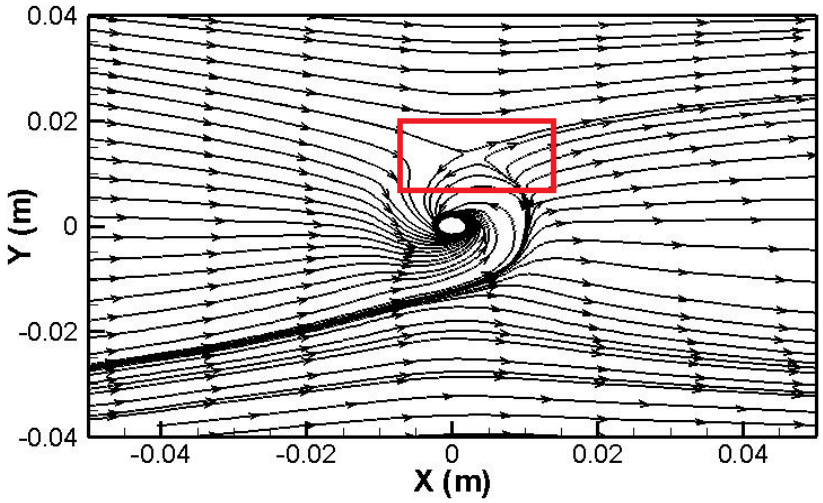

Figure 6.12: Stream traces of conical pin geometry showing the flow separation region on the advancing side of the weld.

The flow separation region is shown in box situated on the advancing side just at the edge of the tool shoulder as shown in Figure 6.12. This region has the maximum probability of defect formation in the welding. For all the tool geometry it lies on the advancing side of the welding.

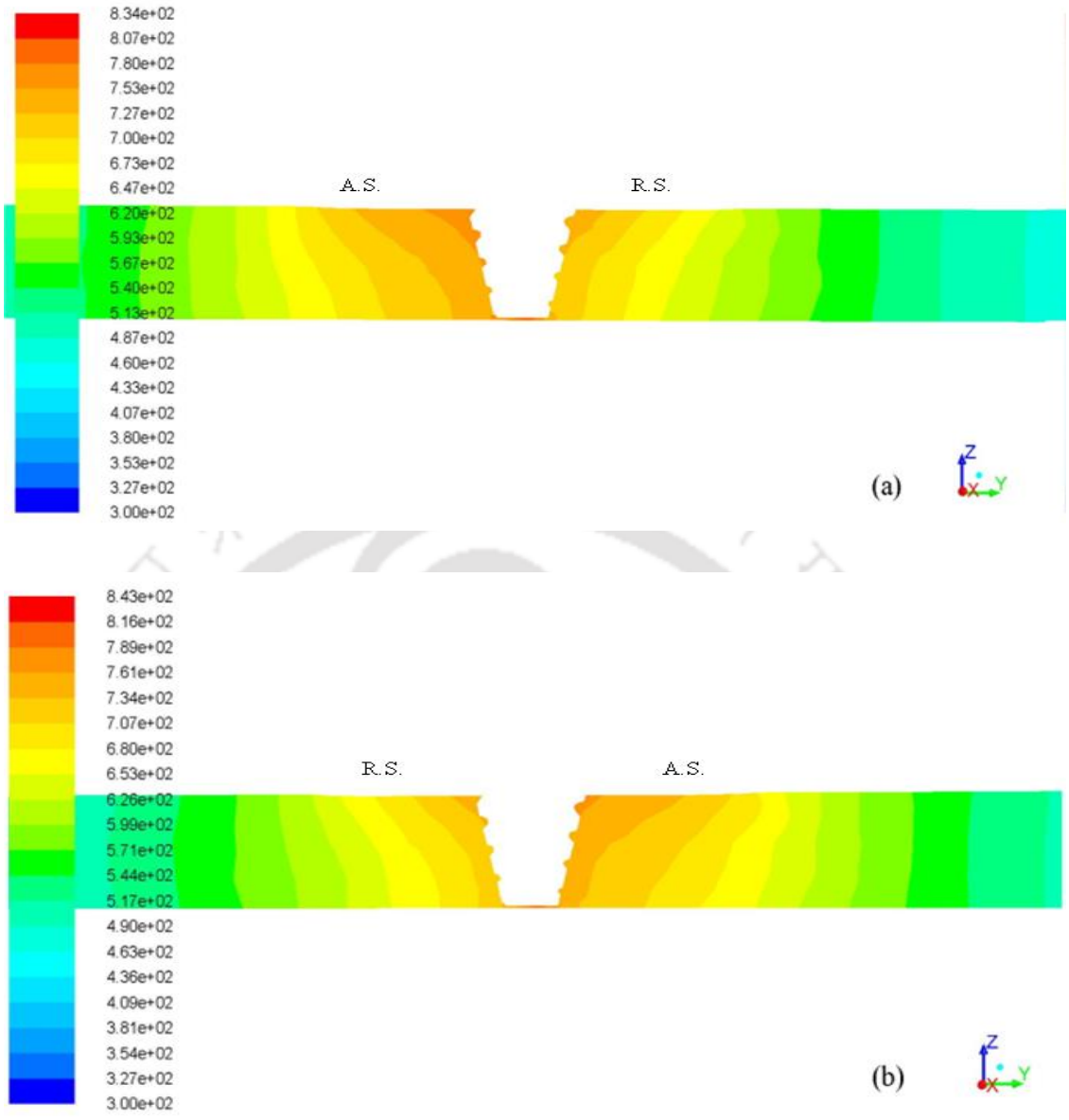

Figure 6.13: Temperature distribution of conical threaded pin profile tool for (a) anti-clockwise and (b) clockwise tool rotation.

In unthreaded tool geometries, it is observed if the tool rotation direction is changed i.e. from clockwise to anticlockwise, the RS becomes AS and vice-versa. In such cases, no significant change in temperature and velocity vector distribution is observed. In threaded tool geometries also, similar trends are observed with small variations in temperature distribution as well as in the vector plot. The temperature distribution on a plane perpendicular to the weld line is shown in Figure 6.13 while the velocity vector distribution is shown in Figure 6.14 on the same plane.

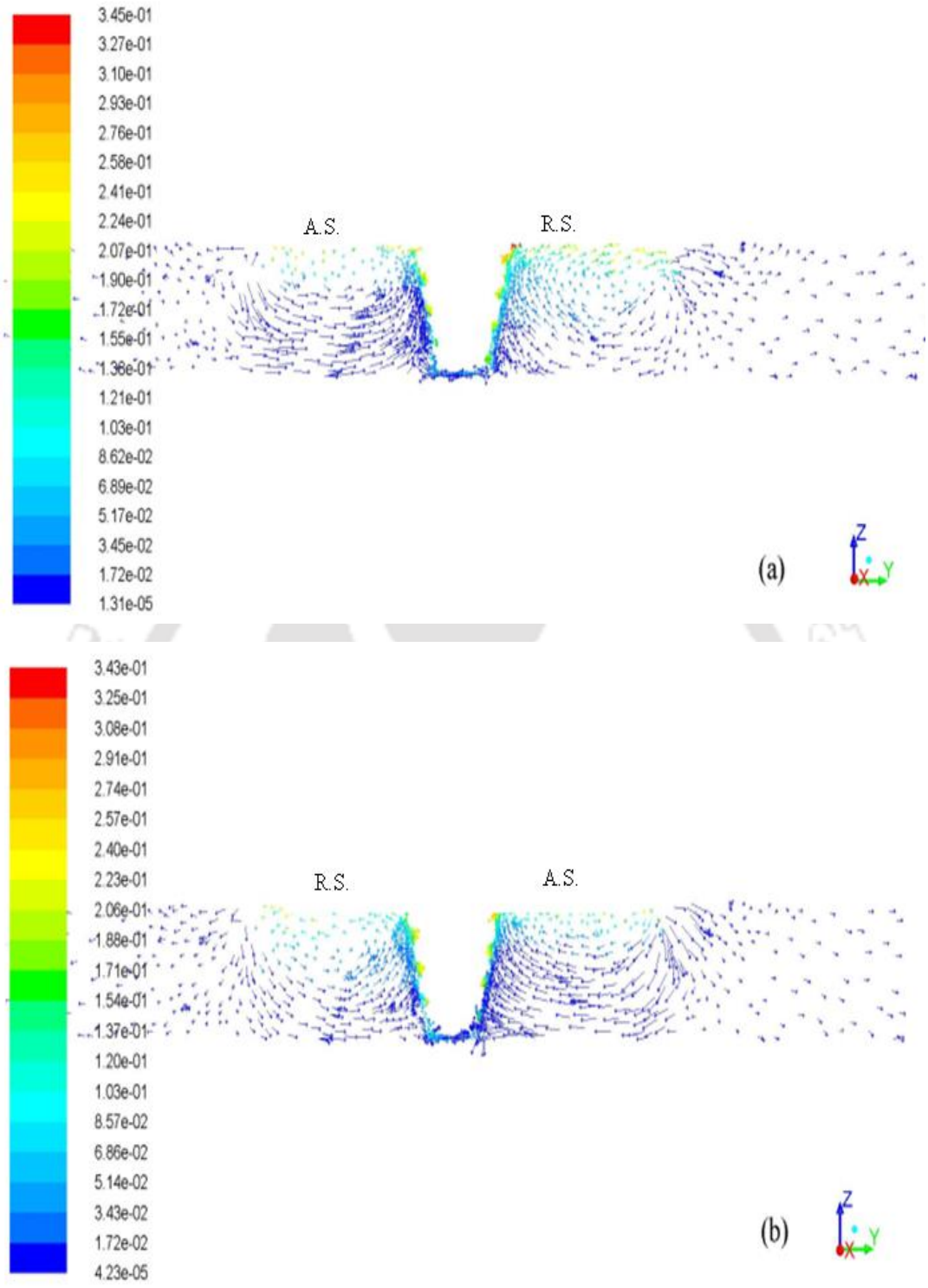

Figure 6.14: Velocity vector plot conical threaded pin profile tool for (a) anti-clockwise and (b) clockwise tool rotation.

The temperature dependent viscosity is considered in all the cases. The viscosity distribution is found to have small variations in each case depending on the temperature and strain rate distribution. The viscosity variation in a plane

perpendicular to the weld line of the conical pin with grooves geometry is shown in Figure 6.15. The viscosity is found to be very low near the pin region and the viscosity increases on moving away from the pin region. Due to this fact, the material deformation is found more near the pin region and very less away from the pin.

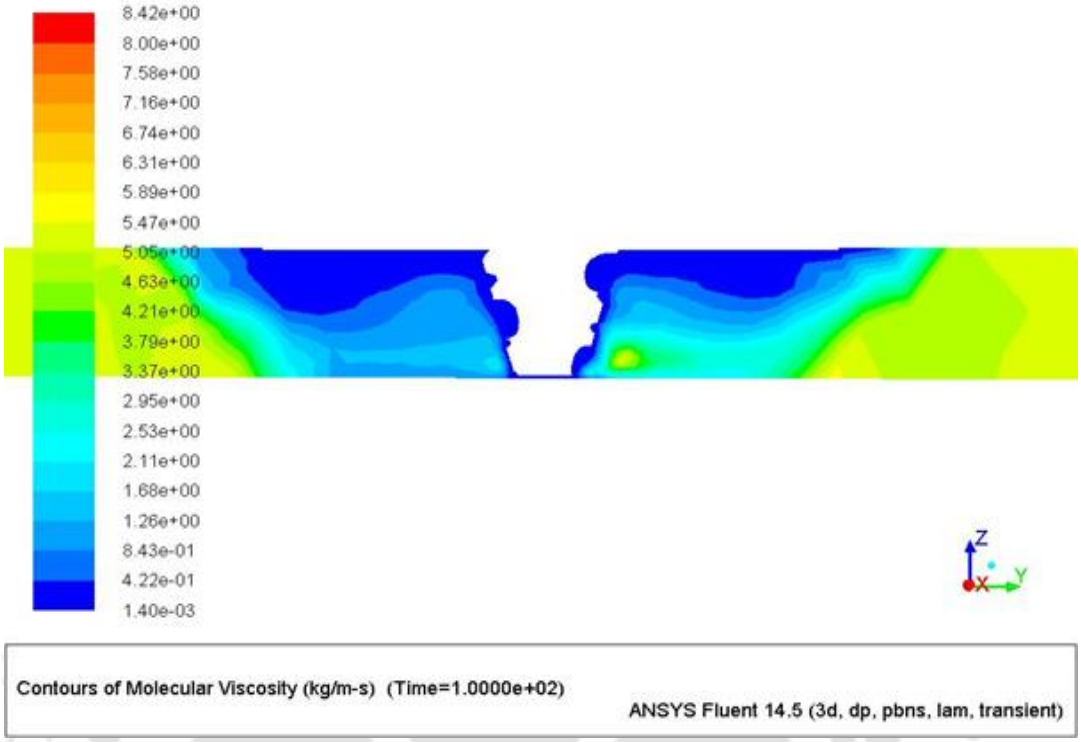

Figure 6.15: A cross-section view of the FSW showing viscosity distribution for a conical with grooves pin profile geometry.

6.3.1 Effect of rotational speed on material flow

In order to analyze the influence of any parameter on material flow, various sections of the weld plates are observed. The tool traverse speed is taken constant as 2 mm/s and the rotational speed is varied as 900 rpm, 1100 rpm and 1300 rpm. The vector plot on a plane 3 mm below the top surface of the material is shown in Figure 6.16.

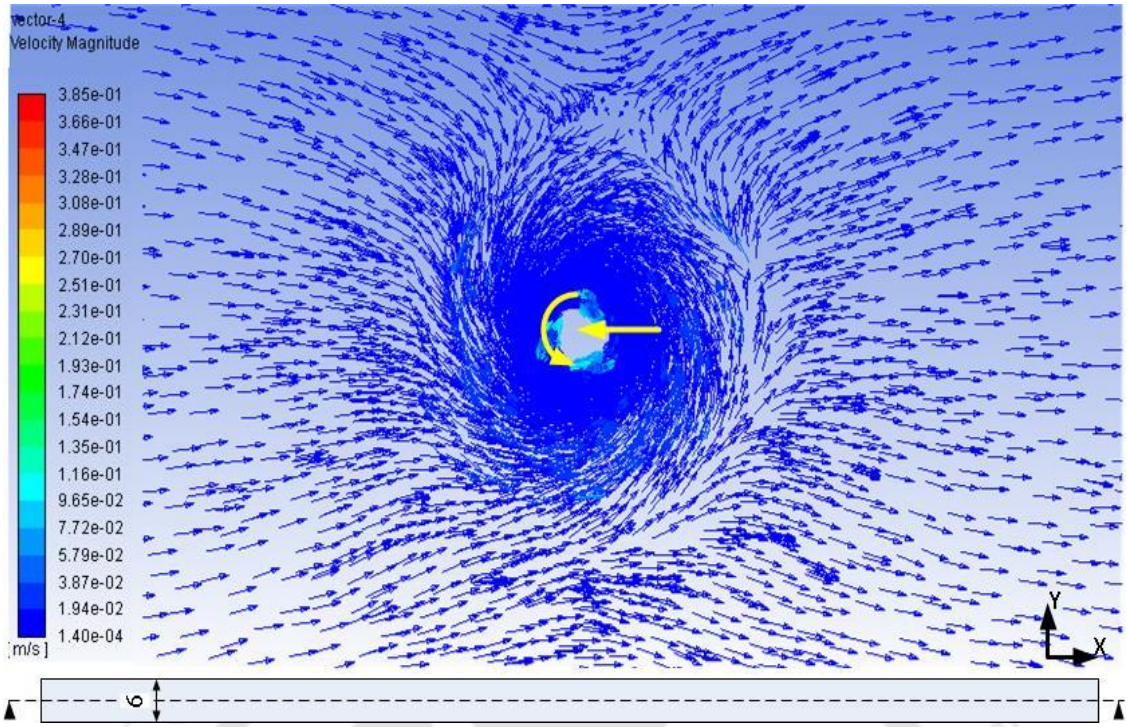

Figure 6.16 (a)

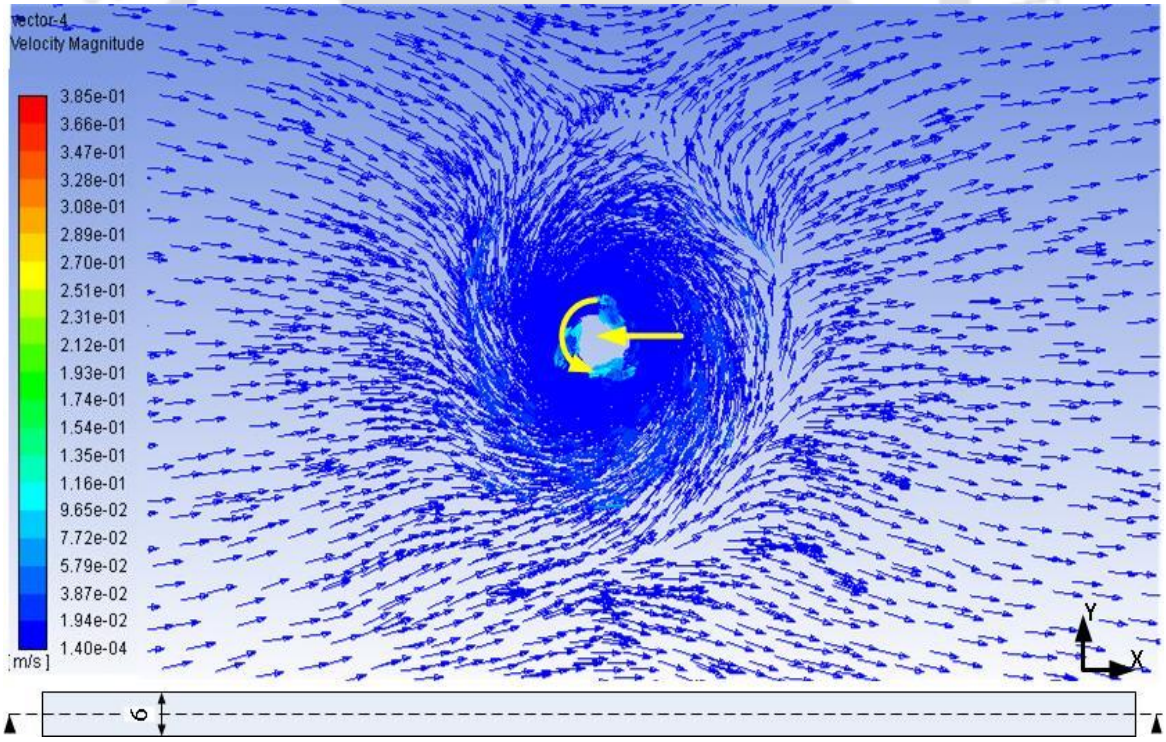

Figure 6.16 (b)

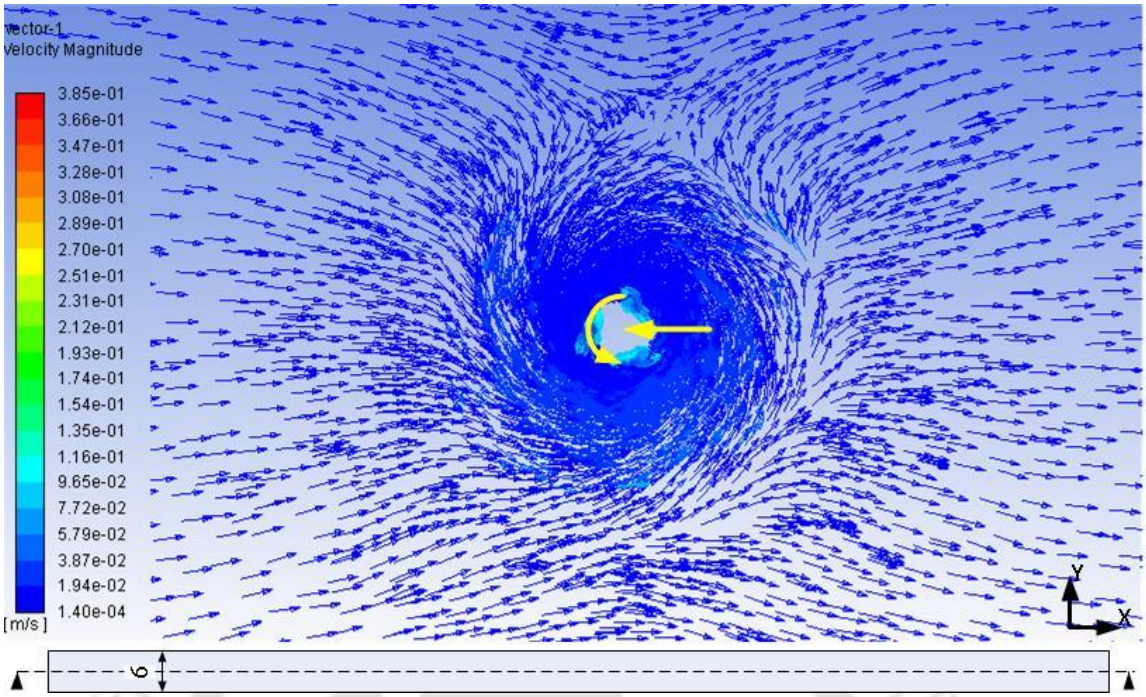

(c)

Figure 6.16: Vector plot variation at (a) 900 rpm, (b) 1100 rpm and (c) 1300 rpm with 2 mm/s welding speed on plane 2.

At all the surfaces, it is noted that materials which are near to the rotating tool has very high speed and the direction of rotation is same as the tool i.e. anti-clockwise in the present case. It is observed that as the rpm of the pin increases, the speed of particles near the tool pin also increase. High rotation velocity generates high deformation of the material near to weld region which ultimately leads to high strain rate values and low viscosity. Moreover, the area of deformation also increases with the increase in tool rpm.

6.3.2 Effect of translational velocity on material flow

For the effects of tool traverse speed on material flow, the tool rotational speed is taken constant as 1200 rpm and the rotational speed is varied as 1.4 mm/s, 2 mm/s and 2.6 mm/s. When material flow velocity vector by magnitude is plotted for all planes, it is found that for each surface the material flow pattern remains same for all the tool traverse speed. Material near the pin has same speed for all the cases as tool rotation speed is constant.

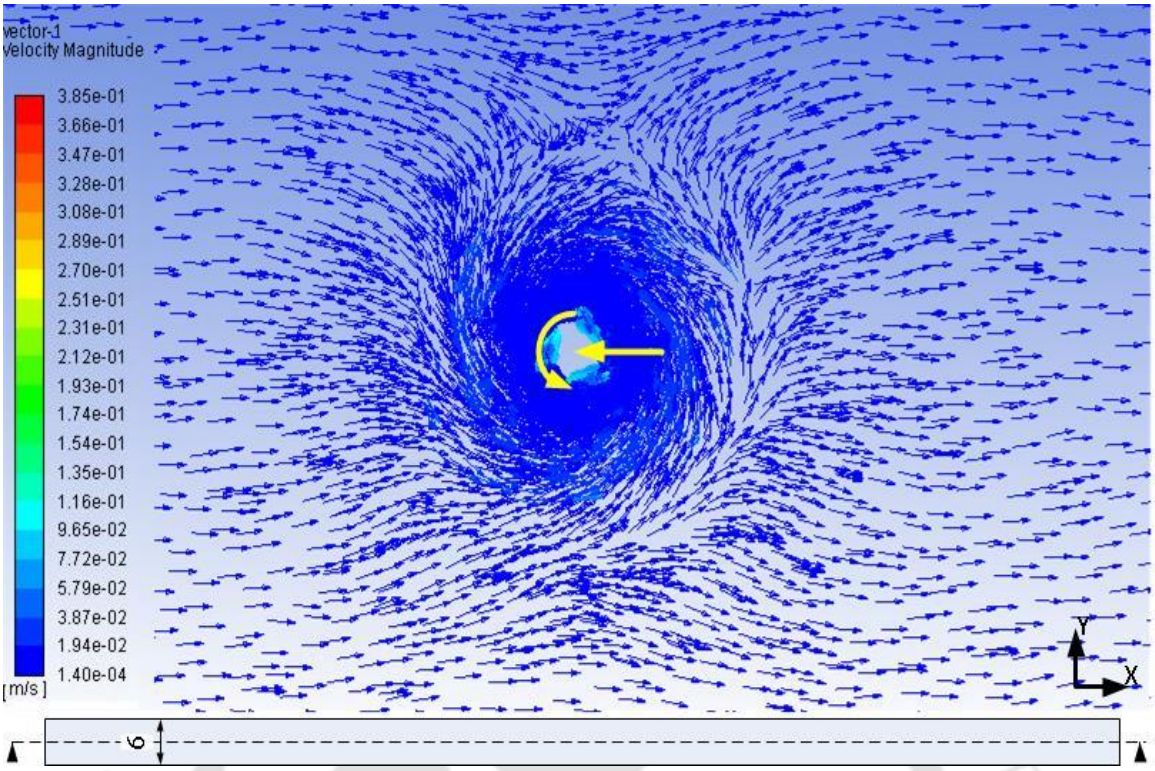

Figure 6.17 (a)

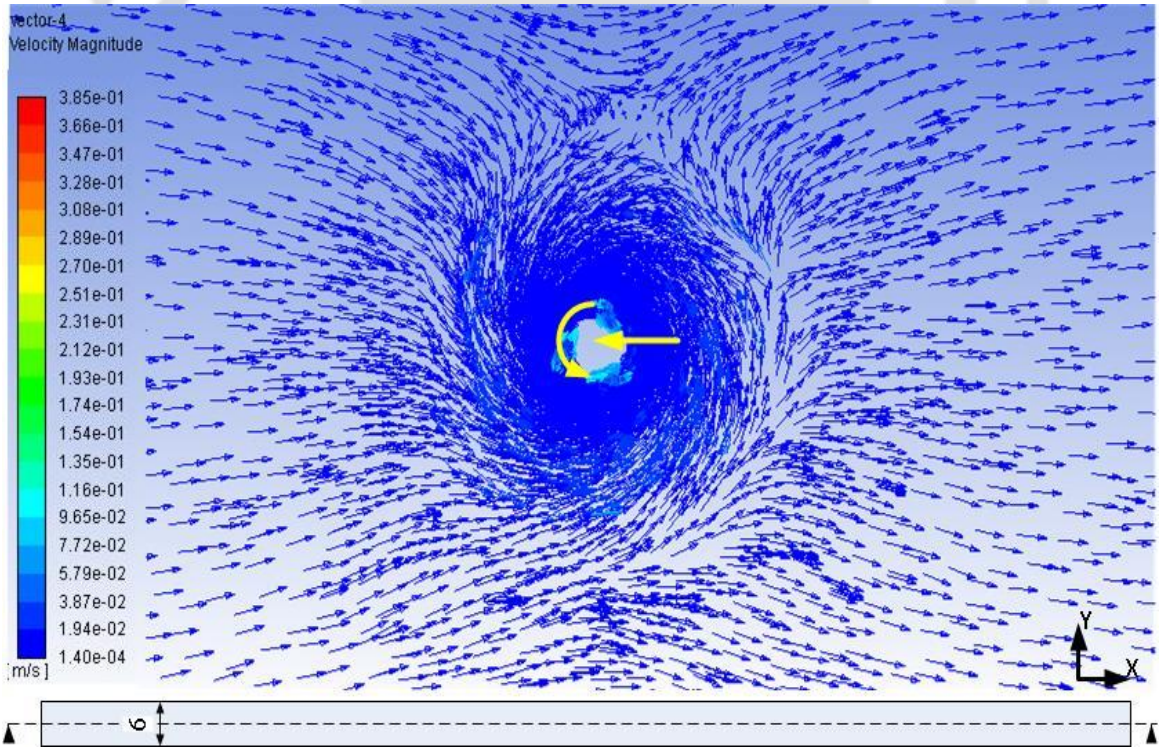

Figure 6.16 (b)

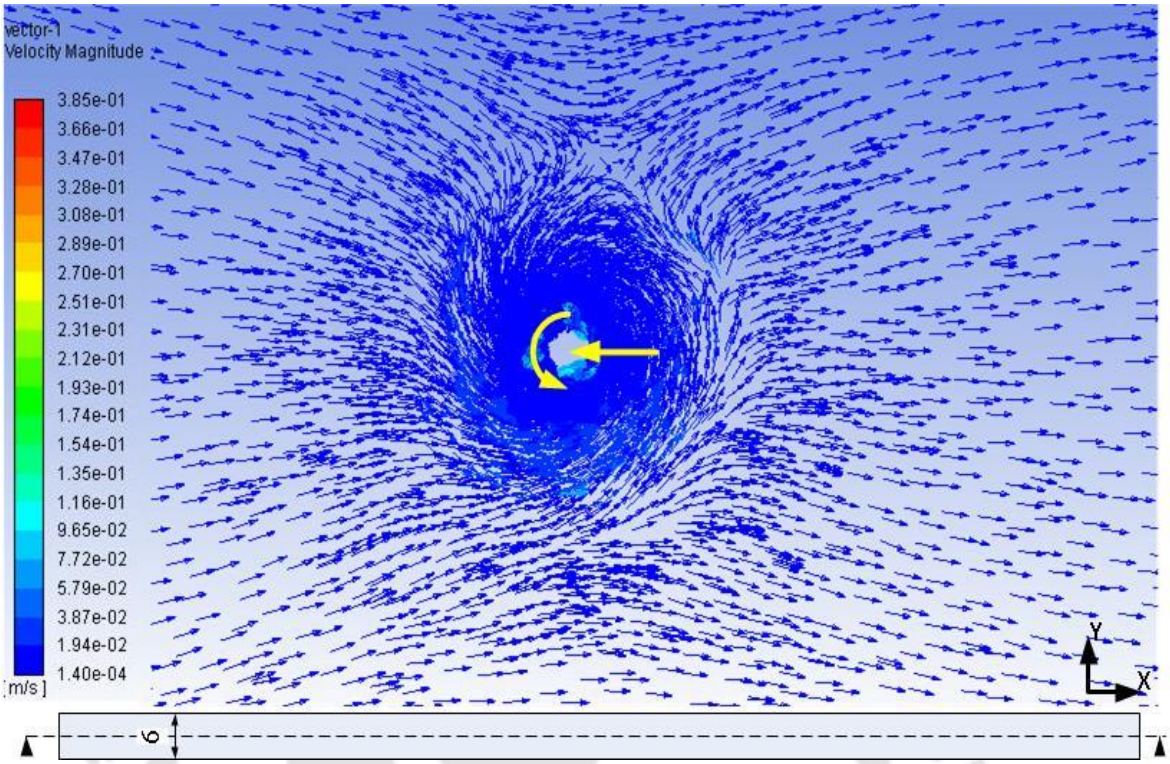

(c)

Figure 6.17: Velocity vector plot at 1100 rpm with (a) 1.4 mm/s, (b) 2 mm/s and (c) 2.6 mm/s tool traverse speed at plane 2.

The material flow width decreases as tool speed increases so less amount of material is stirred as shown in Figure 6.17. Near the top surface, the mixing of stirred material at the retreating side is found be good at 2 mm/s speed but not at the other two speed of tool so to avoid defects optimum tool travel speed should be used.

6.4 Summary

In this chapter, the effect of tool pin geometry on the material flow is studied using a laminar model. Seven different tool pin geometries are considered which provide different material flow behaviours. The cylindrical geometries provided a uniform thermal distribution, thus larger area of nugget zone whereas the threaded pin geometries provided the smaller area with the higher rotation of material movement. Due to this higher movement of material, the better material mixing characteristics are obtained in the case of grooved and threaded pin geometries. The conical pin geometries sometimes lack to move material from the bottom side of the plate due to incapability to transfer heat to the bottom section of the workpiece. The material vortex is observed in all tool geometries but the location is different for each case. The

material flow separation zone is observed on the advancing side of the welding where the chances of the defects are very high. In the next chapter, the material flow behaviour of dissimilar FSW is studied. A volume of fluid (VOF) approach is used to study the mixing of Aluminium and Copper alloys fluids.

Chapter 7

Material Flow Behaviour of Dissimilar FSW

7.1 Introduction

In the former chapter, the effect of tool pin geometry was studied on the material movement. The complete analysis was carried on a single material. The material flow behaviour of Al-Cu FSW is studied in the current chapter. The proposed model uses the volume of fluid (VOF) approach for the mixing of two fluids which is carried out in the commercial finite volume methods (FVM) package ANSYS Fluent 14.5. Experiments are conducted to justify the results obtained from the numerical simulations. AA6061 and B370 Copper plates are used for conducting the dissimilar FSW analysis. A cylindrical flat shoulder threaded tool is used to perform the welding. Furthermore, the effect of tool rotation and welding speed on the material movement are studied.

7.2 Modelling details

The FSW of Aluminium alloy 6061 and Copper B370 (Cu) plates are performed in a numerical finite volume model. The Al and Cu plates dimensions used in the model is same as the experiments i.e. the length of 200 mm, 100 mm width and a thickness of 6 mm. The dimensions of the tool used in the model remain same as experiment with right helix thread (RHT) as shown in Figure 7.1. Likewise, the Copper plates are kept on the retreating side (RS) whereas on advancing side (AS) Aluminium alloy plates are placed with 1 mm eccentricity of the tool towards Aluminium side. The tool geometry is introduced as a wall in the plates which are meshed with tetrahedral and brick elements. A finer mesh is provided near the pin region to capture all features of the pin as shown in Figure 7.2. The welding is performed along X-axis in the model. The model used for the analysis is the volume of fluid model (VOF) to determine the material mixing in the weld region. The complete model details are provided in Section 3.6.

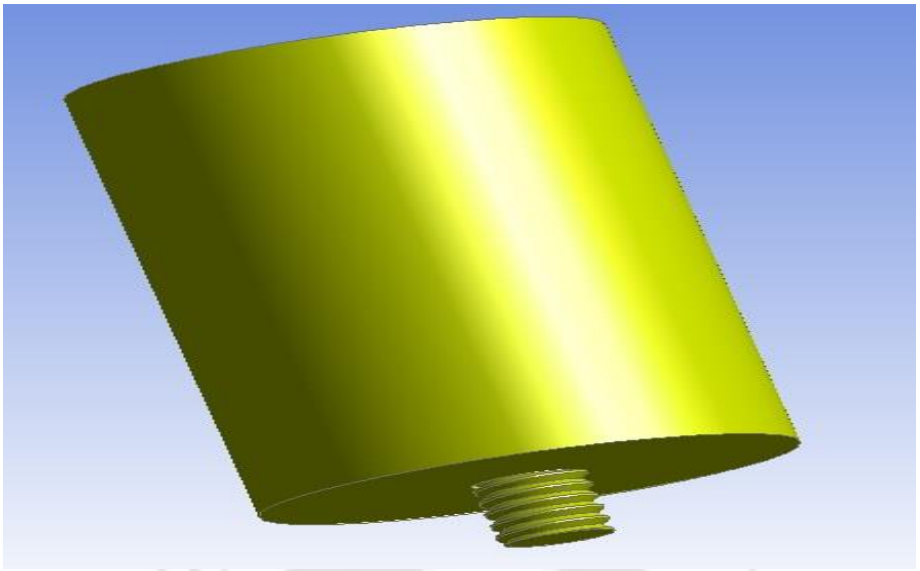

Figure 7.1: The pin profiles used in the analysis.

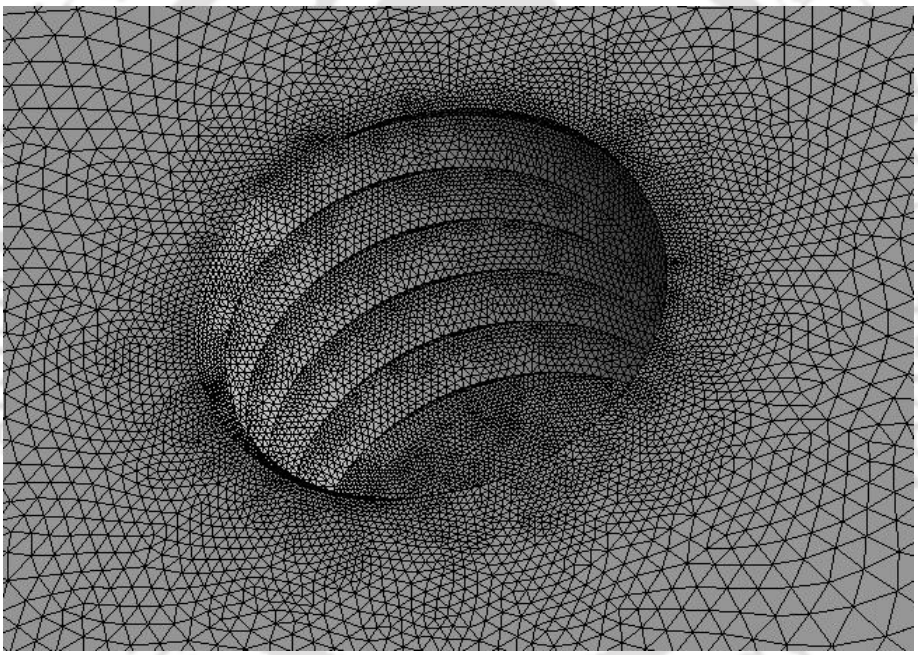

Figure 7.2: Mesh view of the cylindrical threaded pin wall embedded in the plates.

7.3 Results and discussion

The numerical analysis provides the real-time material flow of Aluminium and Copper alloy FSW. The effect of tool rotation and welding speed on material flow is also studied. All temperature dependent material properties are provided in the analysis as mentioned in the earlier section. The coupled thermo-material flow model provides the temperature and material velocity distribution of the Al-Cu FSW.

The top view of the weld plate for temperature distribution of the welding performed at 1100 rpm, 2 mm/s welding speed with 1 mm eccentricity toward Aluminium side is shown in Figure 7.3. However, the temperature variation along the thickness of the plate is shown in Figure 7.4. The variation of temperature is found to be different on the advancing and the retarding sides. The heat dissipation on the Cu side is much faster than the Al side. Therefore, the isotherm contours obtained on the Cu side are much larger than the Al side.

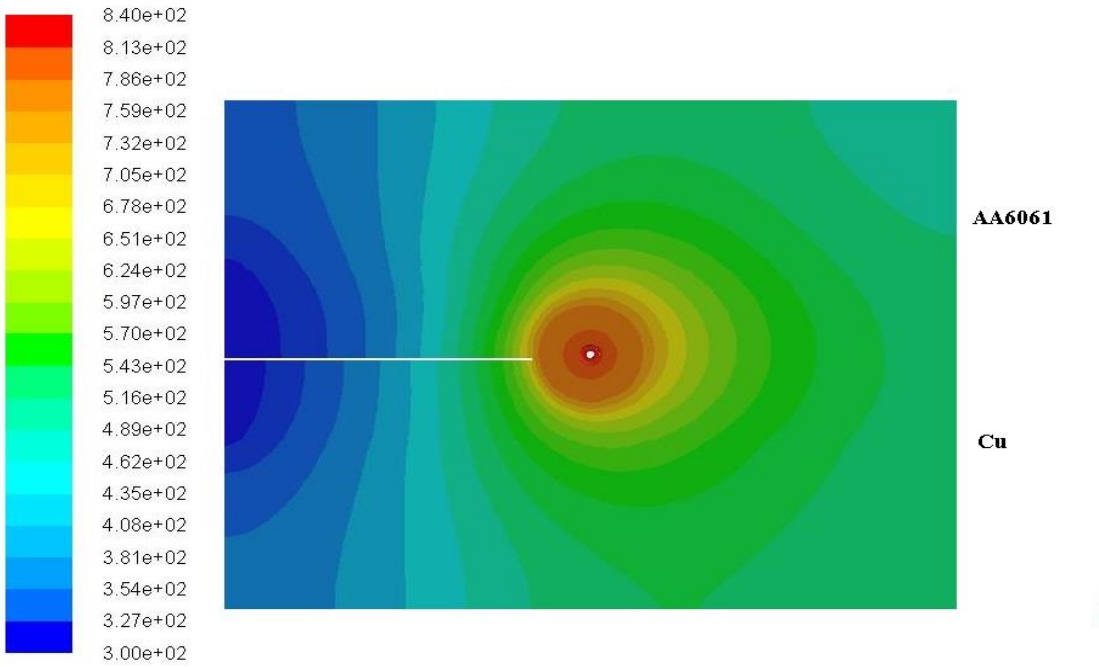

Figure 7.3: Top surface temperature distribution contour of Al and Cu plate FSW. The Al plate is on advancing side while Cu is on the retarding side. The front part shows the unwelded region whereas the back side is the welded region.

The velocity around the pin region along the X direction (V_x) is shown in Figure 7.5. The maximum value of V_x is attained just at the edge of the tool shoulder for 1300 rpm tool rotation. However, the maximum value of V_x for tool rotation, 900 and 1100 rpm is lower than 1300 rpm. Higher values of the X velocity component directly affect the surface finish of the weld zone. Increase in V_x can lead to the tool sliding above the soft material plates along the weld direction. The velocity along the Y (V_y) and Z (V_z) direction around the tool are shown in Figures 7.6 and 7.7. The V_y and V_z components of the material flow velocities are responsible for material flashing out beside the weld bead.

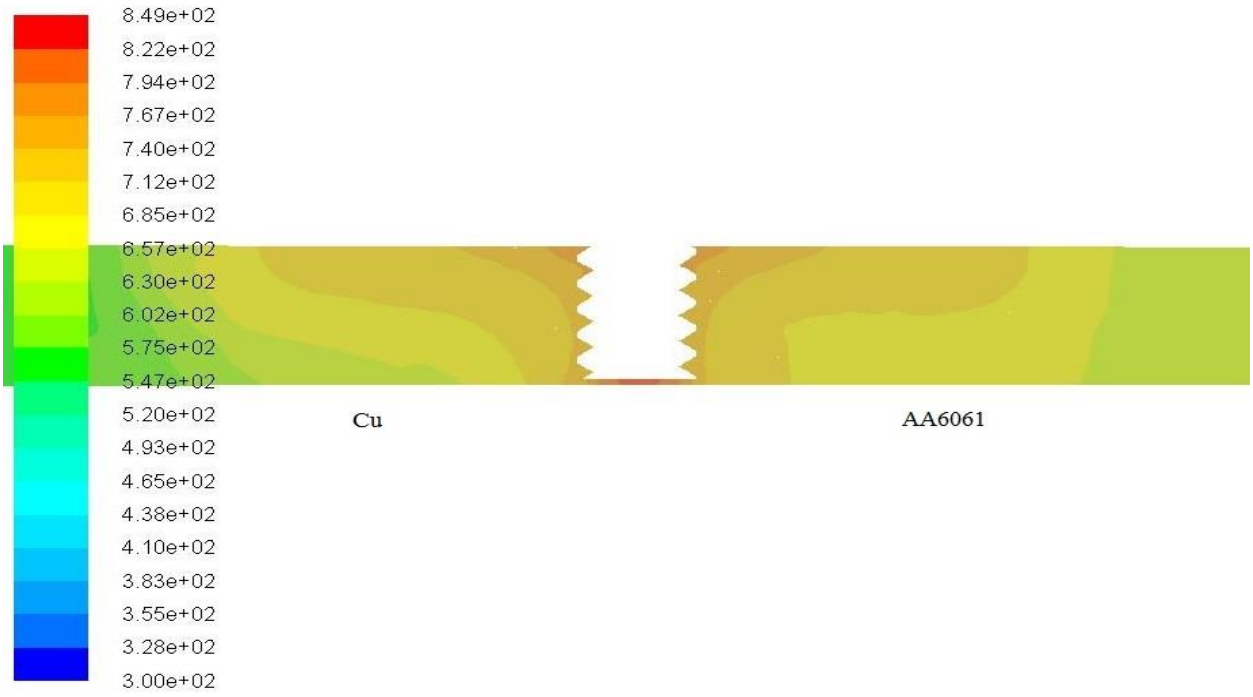

Figure 7.4: The temperature distribution along the cross-section at the mid-region of the plate placing Al and Cu on the advancing and retarding side respectively.

The values and patterns of V_x remain same in Figure 7.5 (a) and (b) which follow a smooth curve throughout. However, notches are observed near the tool shoulder region in V_x velocity contour of Figure 7.5 (c) i.e. 1300 rpm tool rotation because of a significant increase in Y component of velocity near the tool shoulder surface. The V_y velocity is much higher in case of 1300 rpm in comparison to 900 rpm tool rotation as evident from the Figure 7.6 (c). Among all the three velocity components, V_x is the most dominant component but at higher rotational speed the V_y and V_z also affect the flow of plasticized material along the welding direction. The higher values of V_y are obtained on the RS in comparison to the AS of the weld. A jump off 33% in the maximum V_y is observed with an increase of 200 rpm in tool rotational speed. However, the V_z values are doubled at 1300 rpm in comparison to 900 rpm tool rotation speed. The V_z is responsible for the vertical movement of the plasticized material. So, a higher rate of vertical movement of material is observed for higher tool rotation speeds.

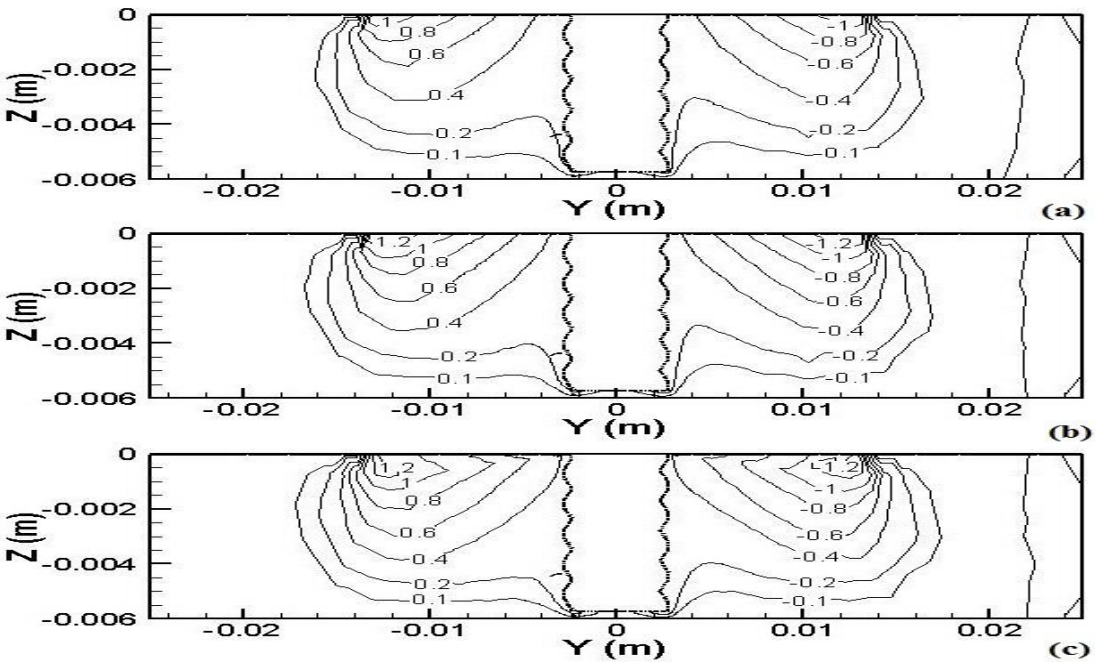

Figure 7.5: The X-direction velocity (V_x) in the cross-section from the mid-section of the plate for (a) 900 rpm, (b) 1100 rpm and (c) 1300 rpm. It is the rate and amount of material movement along the weld line.

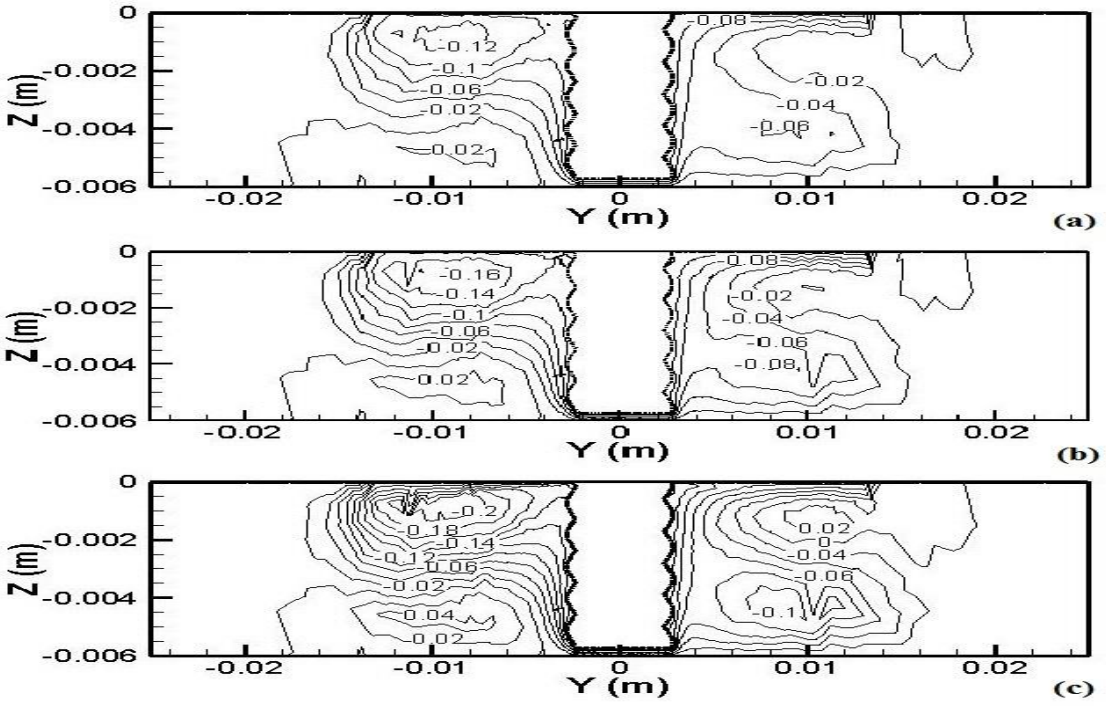

Figure 7.6: The Y-direction velocity (V_y) in the cross-section from the mid-section of the plate for (a) 900 rpm, (b) 1100 rpm and (c) 1300 rpm. It is the rate and amount of material movement forced away and attracted towards the tool pin.

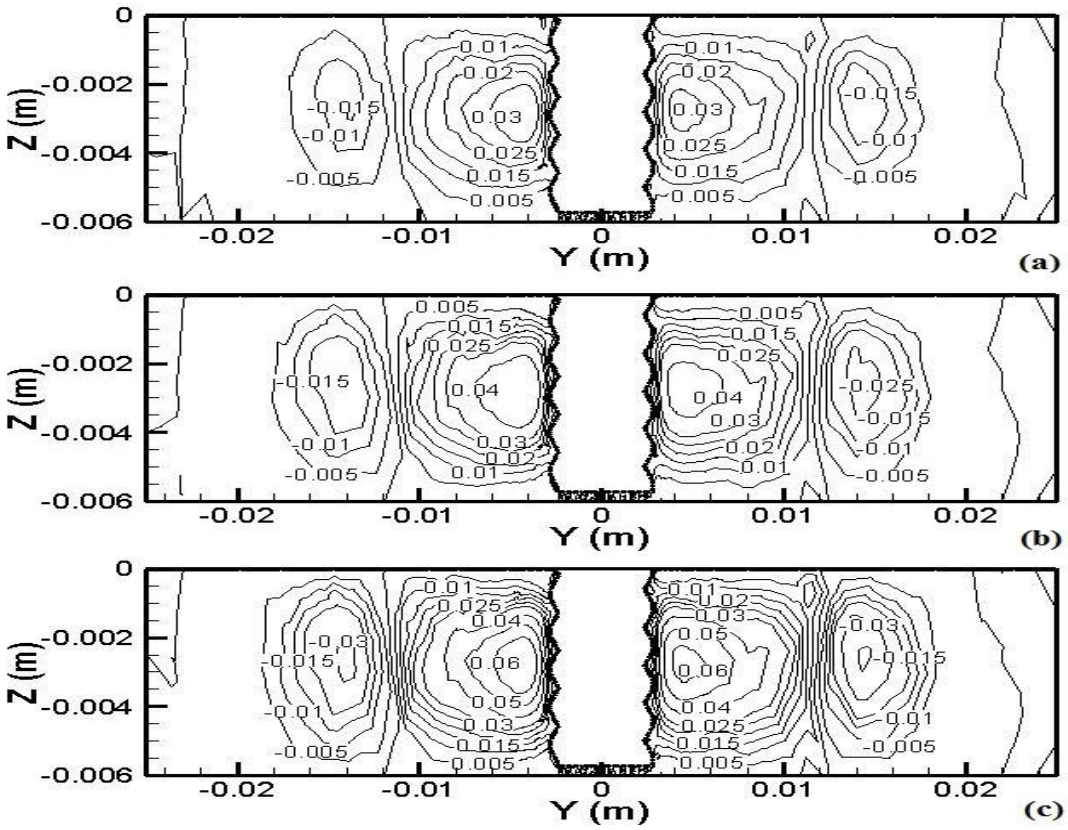

Figure 7.7: The Z-direction velocity (V_z) in the cross-section from the mid-section of the plate for (a) 900 rpm, (b) 1100 rpm and (c) 1300 rpm. It is the rate and amount of material movement along the thickness of the plate around the tool surface.

The lower rates of material movement contours (i.e. 0.2 and 0.1 m/s) are pushed away from the tool surface while the higher rate material movement contours (0.4, 0.8 and 1 m/s) are pulled closer to the tool pin surface at higher rpm which is observed from Figure 7.5. The flattening of lower magnitude contour at higher tool rotation suggests that the nugget zone size increases significantly with increase in tool rotation speed. The amount of upward moving plasticized material is increased with the tool rotation, shown by 0.03 m/s contour area in Figure 7.7.

The velocity in X, Y and Z – direction with welding speed 1.8, 2.0 and 2.2 mm/s is shown in Figures 7.8 to 7.10. The peak V_x remains same in all the cases. However, the differences are observed in the contours such as 0.2 m/s contour moves closer to the tool pin. The shrinkage of contour determines that the amount of plasticized material movement along the weld line decreases with the increase in welding speed.

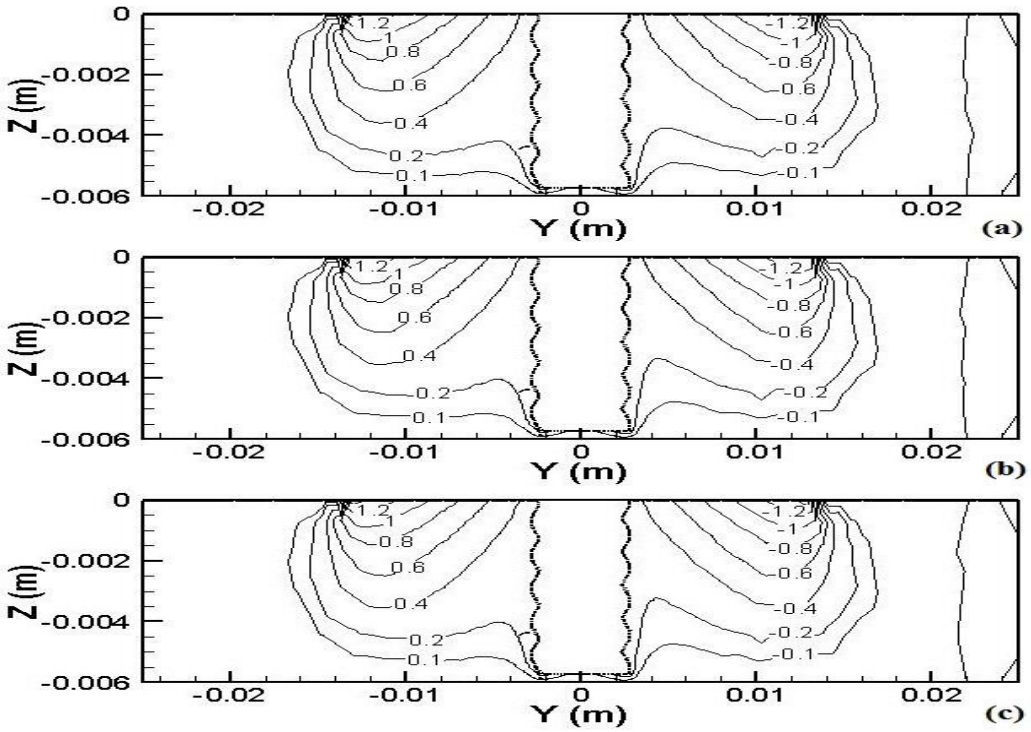

Figure 7.8: The X-direction velocity (V_x) in the cross-section from the mid-section of the plate for (a) 1.8 mm/s, (b) 2.0 mm/s and (c) 2.2 mm/s welding speed.

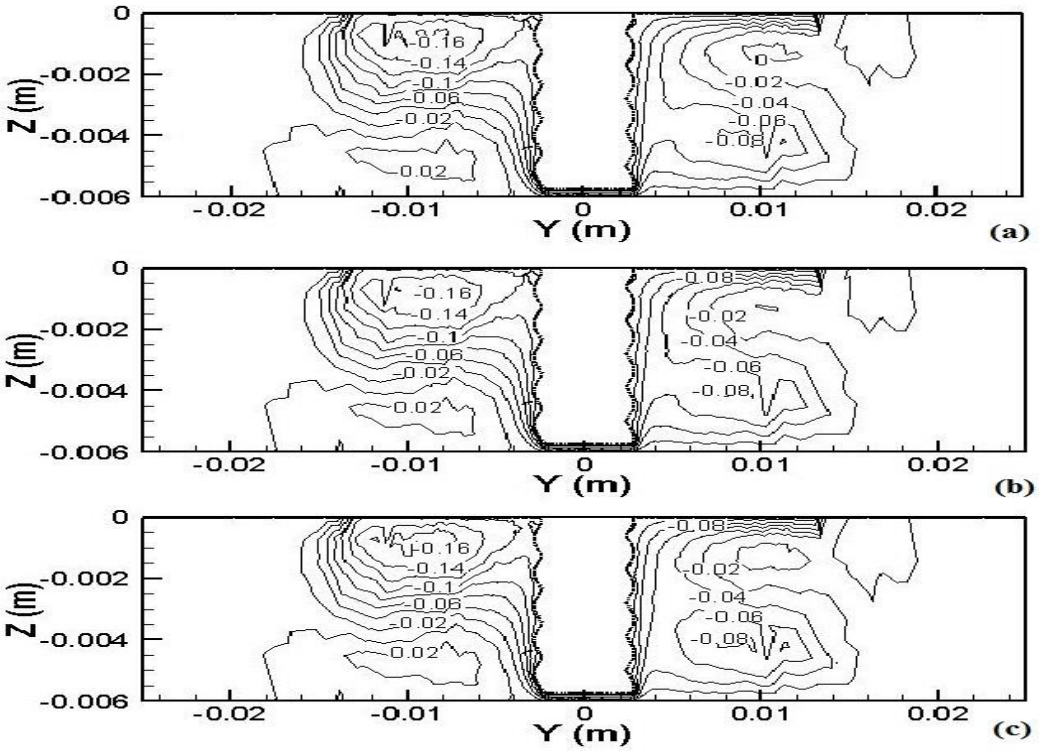

Figure 7.9: The Y-direction velocity (V_y) in the cross-section from the mid-section of the plate for (a) 1.8 mm/s, (b) 2.0 mm/s and (c) 2.2 mm/s welding speed.

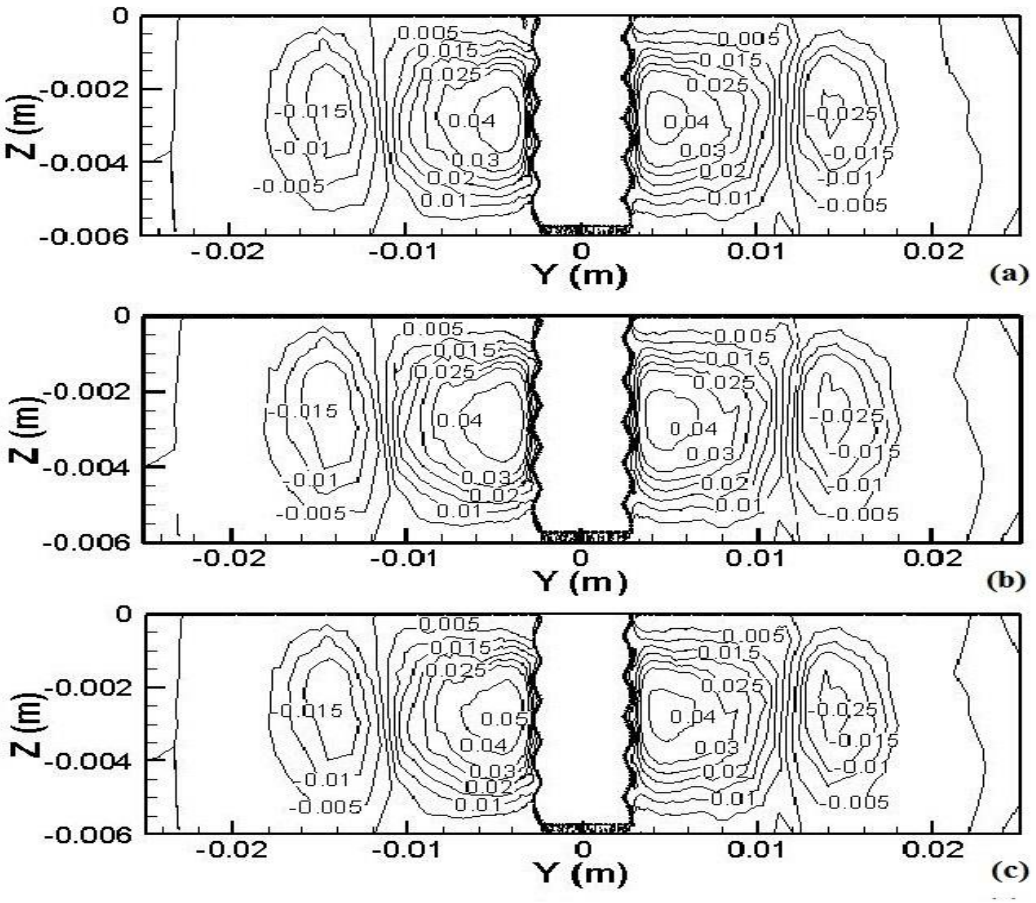

Figure 7.10: The Z-direction velocity (V_z) in the cross-section from the mid-section of the plate for (a) 1.8 mm/s, (b) 2.0 mm/s and (c) 2.2 mm/s welding speed.

The V_y in Figure 7.9 follows the same trend i.e. higher velocity material movement contour shrinkage is observed with increase in welding speed. The maximum and the minimum velocity (V_y) of the materials remain constant for all the three cases. However, the maximum velocity along the thickness (V_z) increases with increase in welding speed. The maximum value is found to be 0.05 m/s for 2.2 mm/s welding speed as shown in Figure 7.10.

The viscosity distribution on the AS and the RS is shown in Figure 7.11. The viscosity calculated in the model is based on the strain rate and the temperature values as explained in the earlier section 3.6.1. The higher viscosity region is found on the AS due to the Cu particles movement on the Aluminium side whereas lower viscosity on the Cu side is mainly due to the high Aluminium movement towards the retarding side (Cu).

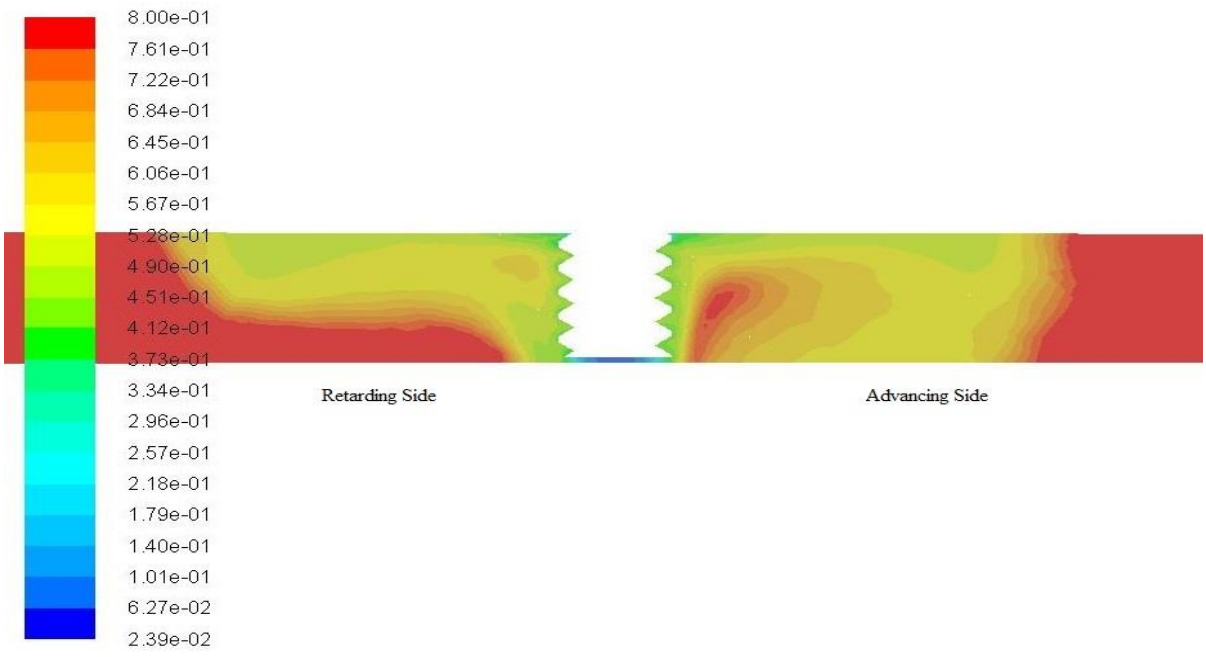

Figure 7.11: The viscosity variation below the tool on the advancing and retarding side along the cross-section plane perpendicular to the welding direction.

7.4 Experimental procedure

The commercial Aluminium alloy (AA6061) and Copper (Cu) B370 plates of 200 mm length, 100 mm breadth and 6 mm thickness are used to perform by friction stir butt welding. The Copper plates are kept on the RS whereas on AS Aluminium alloy plates are placed. The tools are fabricated for the experiments using D3 Tool steel i.e. right helix threaded tool (RHT) with flat cylindrical shoulder with 28 mm shoulder diameter, and cylindrical pin with 6 mm pin diameter, 5.7 mm pin height and 1.1 mm pitch of threads, shown in Figure 7.12.

A vertical milling machine of 7.5 hp motor capacity is modified and used as an FSW machine. The edges of the workpieces are grind and cleaned with the methanol thereafter wiped with the clean cloth to remove oxide films, oil and grease before performing the experiments. Tool pins are placed such that it is 2 mm in Copper plates and 4 mm in Aluminium alloy plates. To prevent the abutting of joint faces, the workpieces are clamped rigidly on a cast iron backing plate.

Figure 7.12: Tool used for performing the experiments.

7.5 Experimental results

Experiments are performed in order to study the effect of tool rotation and welding speed on the material mixing and joint efficiency. The experiments are done, firstly keeping the welding speed constant at 2 mm/s and rotation speed are varied from 900-1300 rpm then keeping the rotational speed constant at 1100 rpm and varying the welding velocity 1.8-2.2 mm/s. The tensile test has been conducted by making ASTM E8 standard samples from the welded plates. Instron-8801 tensile testing machine is used to conduct tensile test with a maximum load capacity of 100 kN shown in Figure 7.13. The tensile test specimens are taken perpendicular to the weld line. The tensile tests are conducted at a constant displacement rate of 1 mm/min.

The tensile test results of all the experiments are shown in Table 7.1. The joint efficiency is the ratio of the maximum tensile strength of the sample to the maximum strength of the weaker base metal element which is Aluminium in this case which has a tensile strength of 110 MPa. The maximum efficiency of the joint is obtained for 1100 rpm and 2 mm/s welding speed. The microstructure of the base material and the welded nugget zone is studied to understand the quality of the weld.

Figure 7.13: Instron-8801 tensile testing machine with AA6061- Cu B370 weld sample.

Table 7.1: The process parameter and the welding efficiency of joints formed during the welding.

Tool Rotation (rpm)	Welding speed (mm/s)	Ultimate tensile strength (MPa)	Efficiency of the joint (%)	Welding region	Observations
900	2	53.7	48.84		Inadequate mixing in weld zone
1100	2	82.8	75.3		Defect free weld, failure outside weld zone
1300	2	61.7	56.15		Defect free weld, failure outside weld zone
1100	1.8	78.2	71.15		Tunnel defect at slow traverse speed
1100	2.2	52.5	48.07		Defect free weld, failure outside weld zone

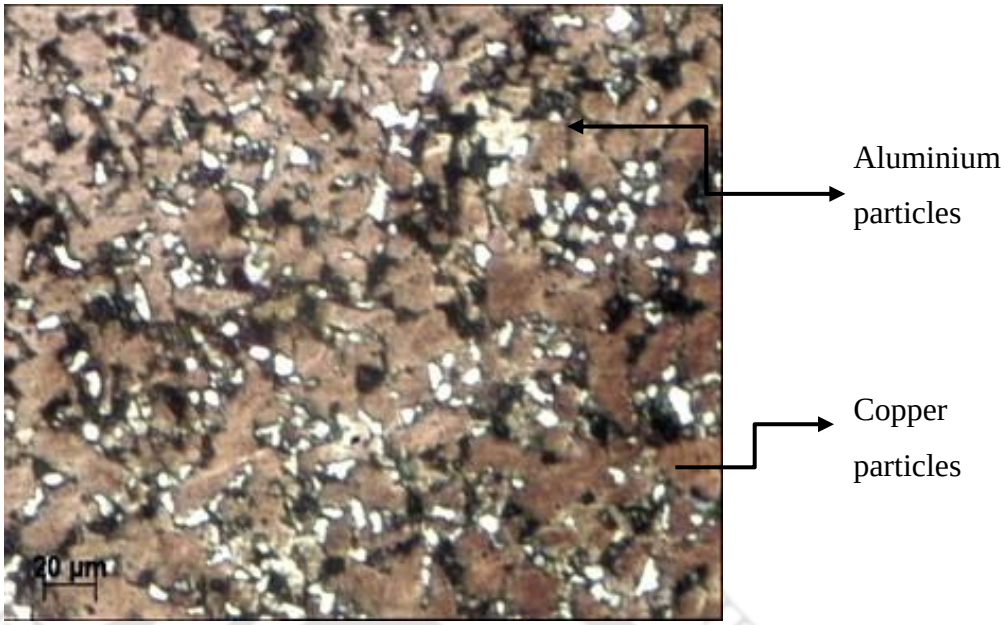

Figure 7.14: Microstructure of the weld nugget zone.

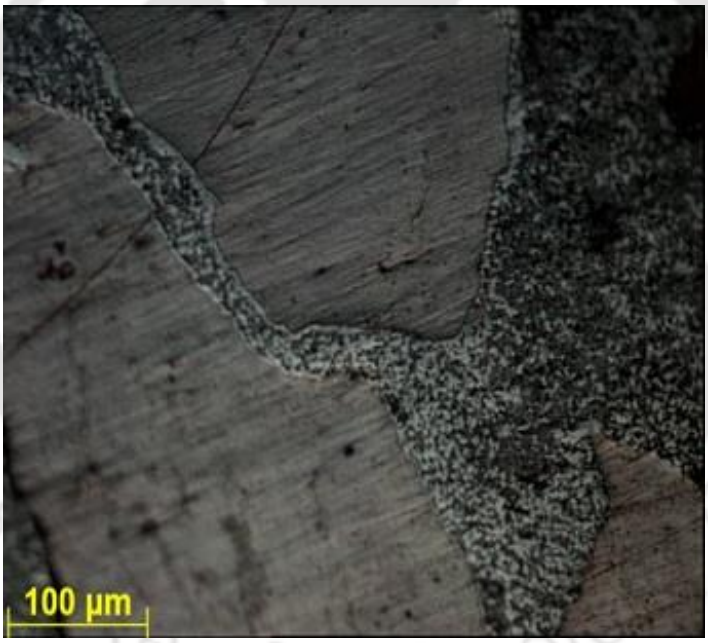

Figure 7.15: The Cu chunks move towards the Al side is visible here.

The sample is taken from the mid-section of the plate and went through mounting, coarse grinding, fine grinding, and polishing, etching and microscopic examination to get the microstructure. The wet grit paper (P400 to P2000) on double-disc grinding machines is used with the grinder followed by the velvet cloth polish with braso and silvo combination to reveal the microstructure on the sample surface.

The micrographs reveal parent material distribution in the nugget zone shown in Figures 7.14 and 7.15. The sample for SEM is taken from the defect free weld formed by 1100 rpm tool rotation and 2 mm/s welding speed. The movement of Cu towards the Al side along with Al-Cu mixing in the Nugget zone is observed in the micrographs. The viscosity distribution in the previous section suggested the same.

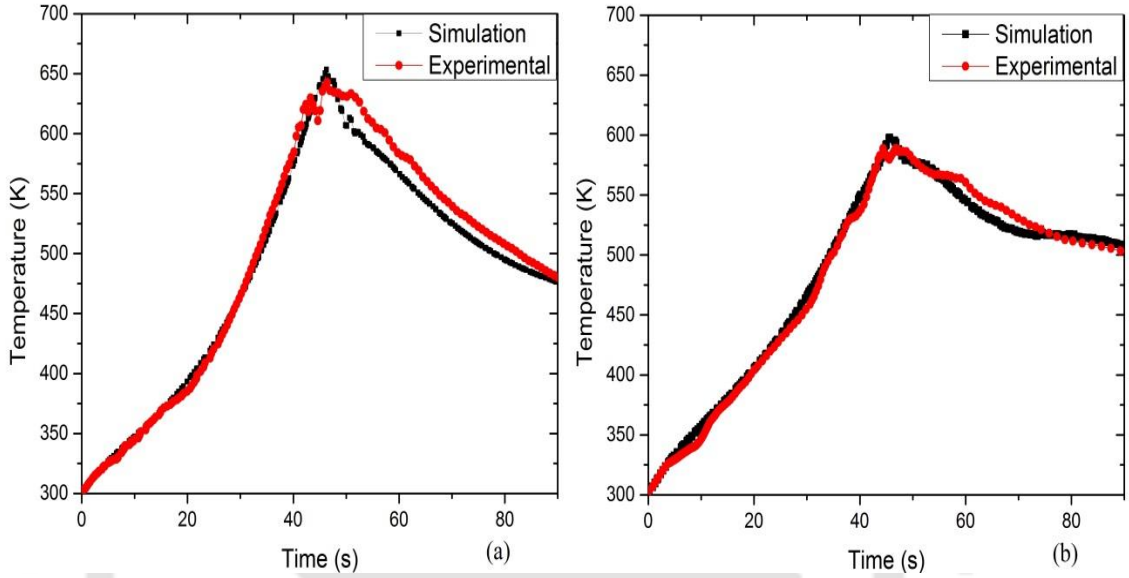

Figure 7.16: The temperature profile at 20 mm from the weld line (a) advancing side and (b) retarding side.

The temperature profiles of the experimental and simulation model are compared in Figure 7.16. The temperature data is taken at 20 mm away on both the sides of the plates. The points are selected such that temperature rise and fall can be recorded. Therefore, the points are taken at the mid-section of the welding direction. The temperature readings are taken with 1 mm diameter K-type thermocouples (chromel and alumel wires). The thermocouples are connected to the data acquisition system (Agilent-34970A) to record the temperature data. The tool rotation speed is 1100 rpm, 2 mm/s welding speed and 1 mm eccentricity towards the Al side. The maximum temperature obtained in the simulation at 20 mm away from the weld centre line is 653 K and 597 K on the advancing side and retreating side respectively. However, for the experiments, it is found to be 642 K and 588 K on the advancing side and retreating side respectively.

7.6 Summary

In this chapter, the material flow of dissimilar FSW is studied. The flow model used in this analysis is a laminar model. The effect of the process parameter is also studied on the material flow. It is found that the tool rotational and traverse speed affect the nugget zone size. The model is well validated with the experiments. A tunnel defect is formed during the experiments which are measured and modelled in geometry. In the next chapter, a comparative study is conducted between the defected and a healthy geometry. The study is based on the velocity response obtained along the weld line.

Chapter 8

Material Flow Behaviour for Defected Geometry

8.1 Introduction

In the former chapter, the material flow behaviour of dissimilar FSW was studied. The effect of tool rotation and tool travel speed on material flow was studied on Al-Cu butt welding joint. It was observed some set of parameters lead to defected weldment formation. One of the common defects observed in such cases is the tunnel defect. In this work, this tunnel defect is measured in detail with the experiments and implemented in the material flow model. The comparative study has been performed for a defected and undefected plate based on the velocity response during the welding. The velocity response clearly shows the flow difference between the two plates.

8.1 Modelling details

A tunnel defect is found in the joining of AA6061 and Copper B370. The dimension and the location are taken from the sample and the same is implemented in the material flow model as shown in Figure 8.1. The Figure 8.2 shows the tool pin geometry along with the defect size and shape that is used in the current analysis. The defect is an oval-shaped cavity formed in the welded plate with the dimension of 1.4 mm length and 0.8 mm breadth. The setup for the simulation is taken the same as the previous analysis as shown in Figure 8.3. The tool is also taken same as 28 mm shoulder diameter with a threaded pin length of 5.75 mm and 6 mm tool pin diameter. The tool rotation is provided as 1100 rpm and 1.8 mm/s tool travel speed. The Aluminium alloy is placed on the advancing side and the Copper alloy is placed on the retreating side with 1 mm eccentricity towards the Aluminium alloy plate. In terms of the co-ordinate system, the tool rotation axis is along the Z direction and the material flow is along the X direction. The plate dimensions are also taken same as the experiment and the previous simulation that is 200 × 150 × 6 mm. The outer region of the plate is taken as solid while the central region is taken as fluid from 25 mm to -25 mm in Y direction which is shown in Figure 8.3. The two fluids walls are used to input

the Aluminium and Copper fluid which are separated through a fine slit. The front side of the tool is unwelded while the back side of the tool is welded. Therefore, the two fluids are separated till the tool region then are allowed to mix under the tool due to the rotation.

To compare the defected and undefected (healthy) weldments, 5 points are taken on X-axis where the Y and Z coordinates are taken as 0 and -3 respectively. Four Points are taken under the tool shoulder region i.e. from 5 to 12 mm and one point is taken outside the tool shoulder region which is at 16 mm from the centre of the tool along welding direction (X-axis) as shown in Figure 8.4.

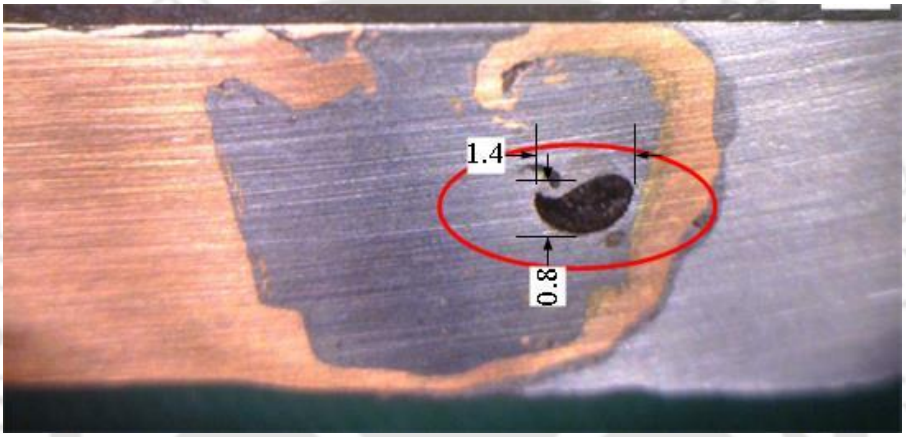

Figure 8.1: Measurement of tunnel defect formed during the welding.

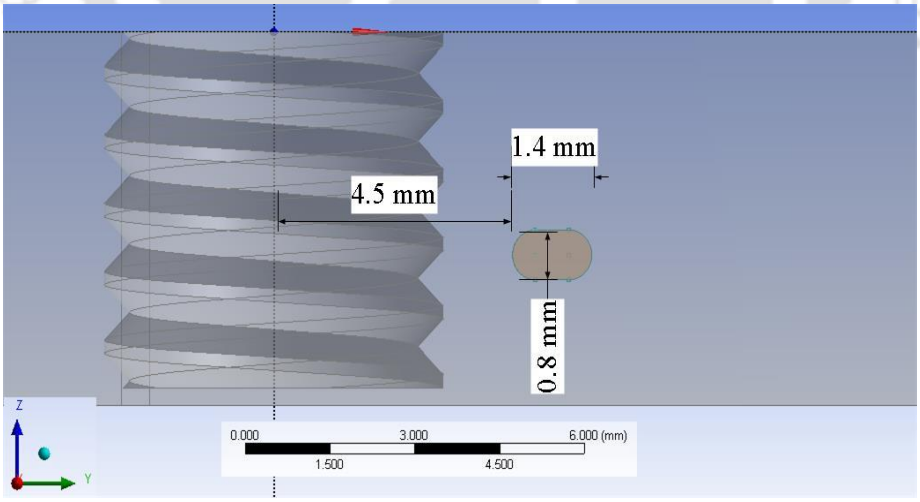

Figure 8.2: Defect measurement made 3.5 mm below the top surface in geometry of the material flow model.

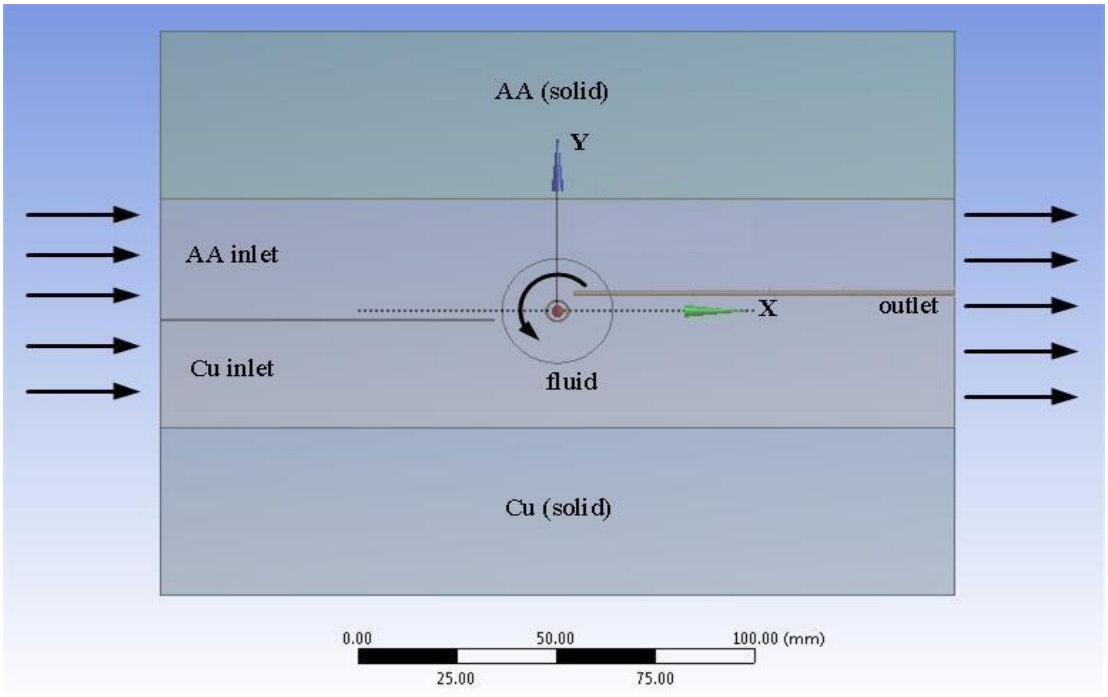

Figure 8.3: The model setup with all the walls and the material region used in the analysis.

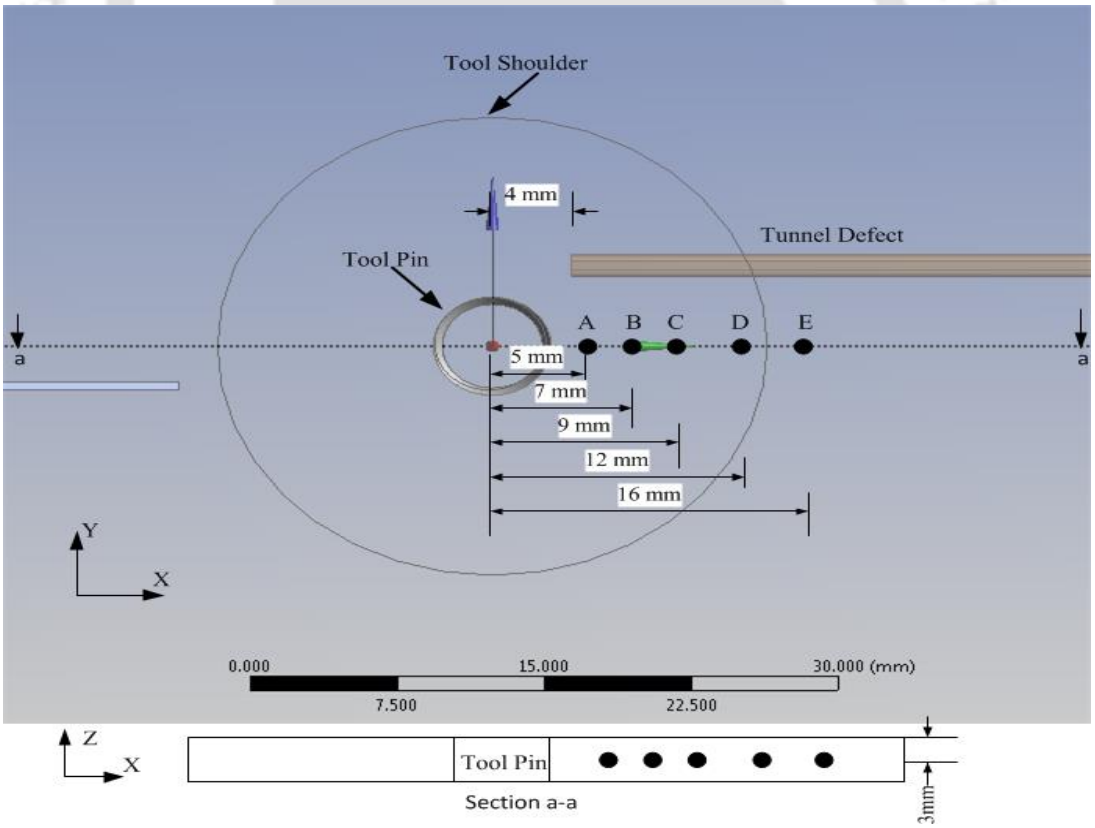

Figure 8.4: Observatory point situated at the middle of plate thickness just behind the pin. Four points are under the shoulder while one point is outside the shoulder region.

8.2 Results and discussion

The velocity response has been studied on a defected and undefected plate with the help of the velocity-time graphs. The velocity response of point A is shown in Figure 8.5. The figure compares the overall material velocity of defected and undefected weld material along with all three components i.e V_x, V_y and V_z.

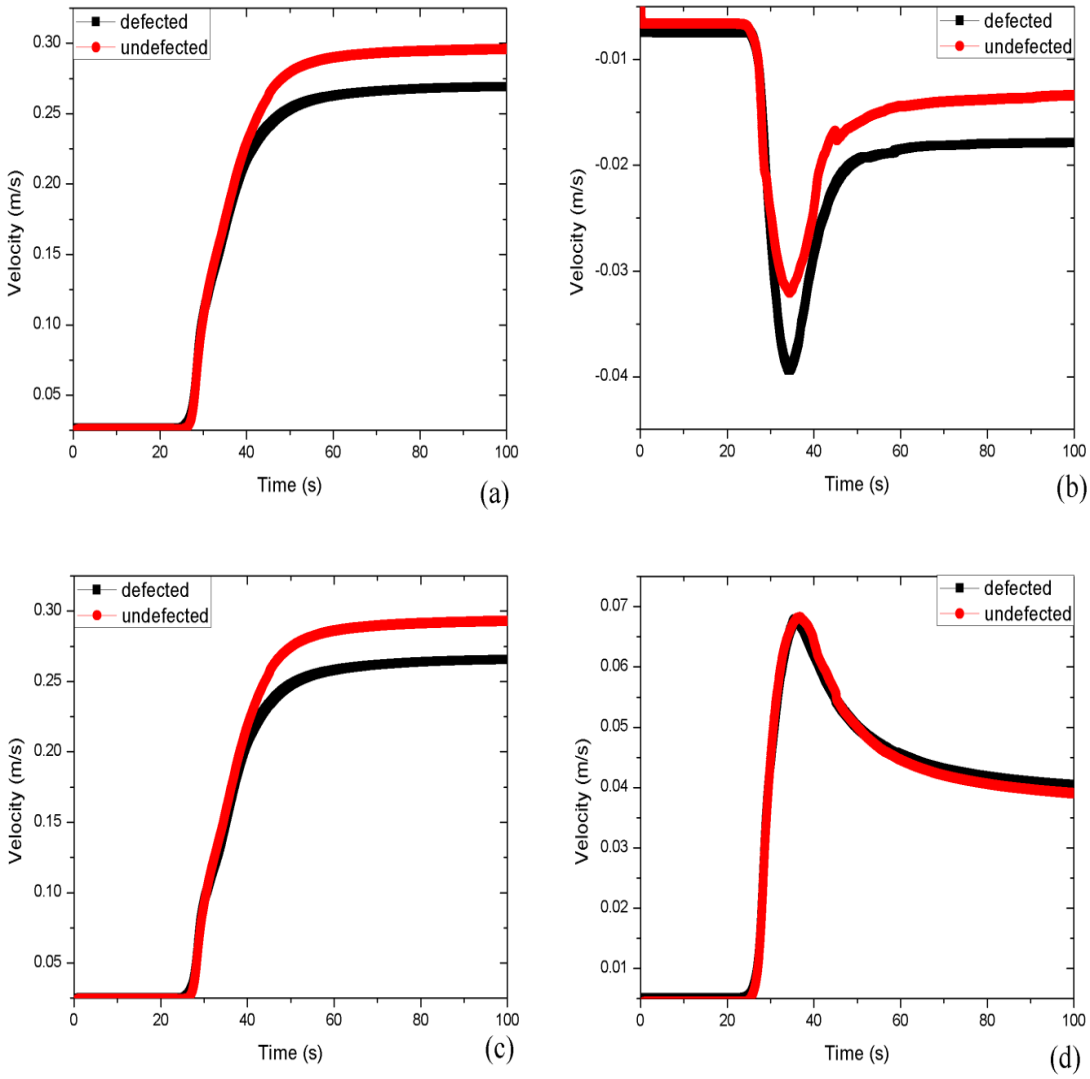

Figure 8.5: The comparison of velocity response obtained for defected and undefected model in terms of (a) Resultant velocity magnitude (V), (b) X-component velocity (V_x), (c) Y- component velocity (V_y) and (d) Z-component velocity (V_z) at point A.

The Figure 8.5 suggests that the most dominating velocity component is V_y in comparison to V_x and V_z. Thus, the resultant velocity follows the same pattern as V_y. However, V_z has the least effect on the resultant velocity due to lower magnitude. The

observatory points are just behind the tool pin and in the high influence of the tool shoulder rotation which has a tangential velocity along Y-direction of the plate. Therefore the magnitude of V_y is much higher than the other two components. The same pattern is observed in the velocity response of point B as shown in Figure 8.6.

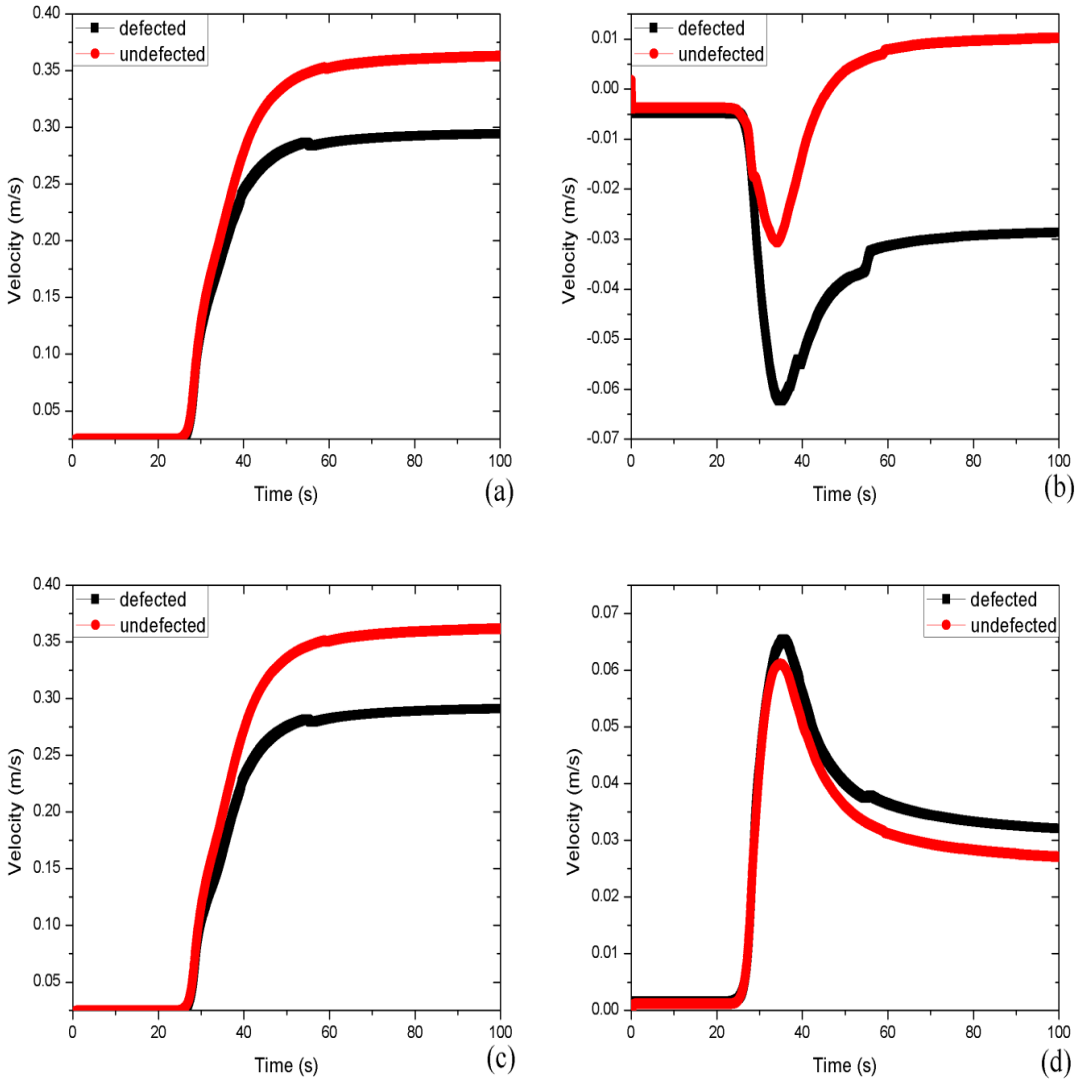

Figure 8.6: The comparison of velocity response obtained for defected and undefected model in terms of (a) Resultant velocity magnitude(V), (b) X-component velocity (V_x), (c) Y- component velocity (V_y) and (d) Z-component velocity (V_z) at point B.

On moving from point A to B, i.e away from the tool pin, the velocity magnitude in the mid-thickness of the undefected plate increases from 0.29 to 0.36 m/s. A similar trend is observed in the defected plate, the mid-thickness velocity increases from 0.24 to 0.29 m/s which is slightly less than the undefected plate. So, material velocity near the tool pin region is higher for the undefected plate in comparison to the defected one.

However, it is found that V_x changes significantly on moving away from the tool pin which is observed from Figure 8.5 (b) and Figure 8.6 (b). For a healthy or undefected weld plate, at point A, the V_x is negative which means the material movement is towards the tool pin region, however, at point B, the V_x is positive which means the material is going away from the tool pin. In case of the defected plate, the V_x has negative values on both the points (A and B) which mean higher amount of material is moving towards the tool pin as the negative velocity region is bigger. It is also noted that the magnitude of V_x for a defected plate is three times higher than the velocity obtained for the undefected plate. At point A, V_z shows similar trend and magnitude for both defected and undefected geometries but starts deviating away from point B onwards.

The point A, B, C, D, and E are oriented in such a way that the negative V_x velocity signifies the material movement towards the tool rotation while positive value gives the movement of the material away from the tool rotation axis. The comparison of V_x of defected and undefected plate on all five points is shown in Figure 8.7. Among these 5 points, the maximum difference in V_x magnitude between the two geometries is found in C which is 9 mm away from the rotation axis of the tool. The defected geometry maintains a negative value on points A, B, and C while a positive value is obtained for D and E. Therefore, the material tends to move towards the tool pin till point C and move away from the tool axis near the tool shoulder edge. The point D is much closer to the edge of the tool geometry but lies inside the tool periphery. At this point, the V_x profile for both the geometries behaves very differently. The defected geometry has an abrupt change in V_x of the material movement i.e. the direction of material flow gets reversed with four times higher magnitude compared to undefected geometry material flow. On moving from point C to D, the V_x value changes from -0.03 to 0.04 m/s in defected plate geometry in comparison to 0.01 to -0.01 m/s in undefected plate geometry. However, from point D to E, the magnitude of the velocity decreases to 0.02 m/s without any change in direction but in case undefected geometry the direction of material flow again change with a small change in velocity magnitude.

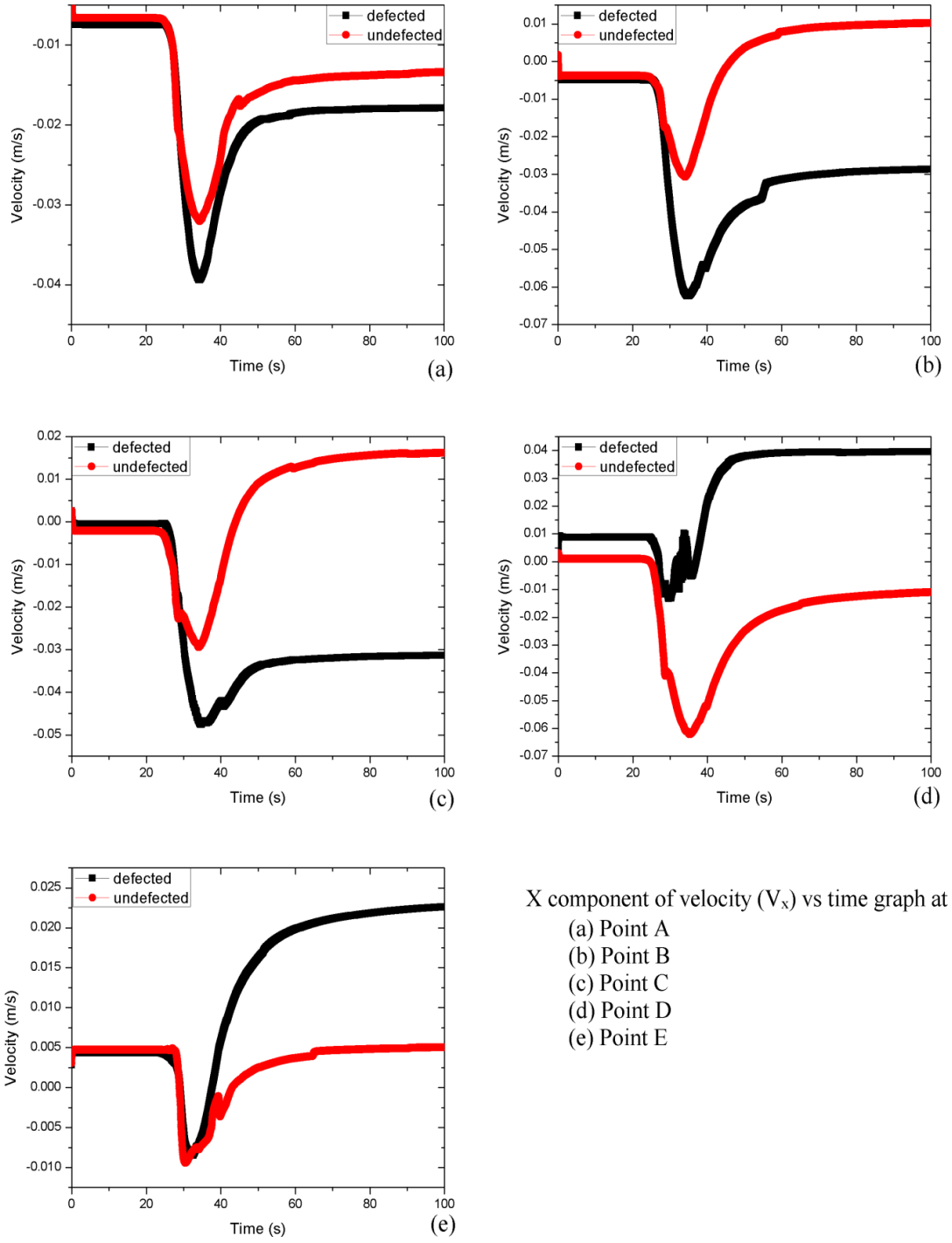

X component of velocity (V_x) vs time graph at
(a) Point A
(b) Point B
(c) Point C
(d) Point D
(e) Point E

Figure 8.7: The X-velocity (V_x) components of defected and undefected weld geometry at all five points. The velocity is along the welding direction.

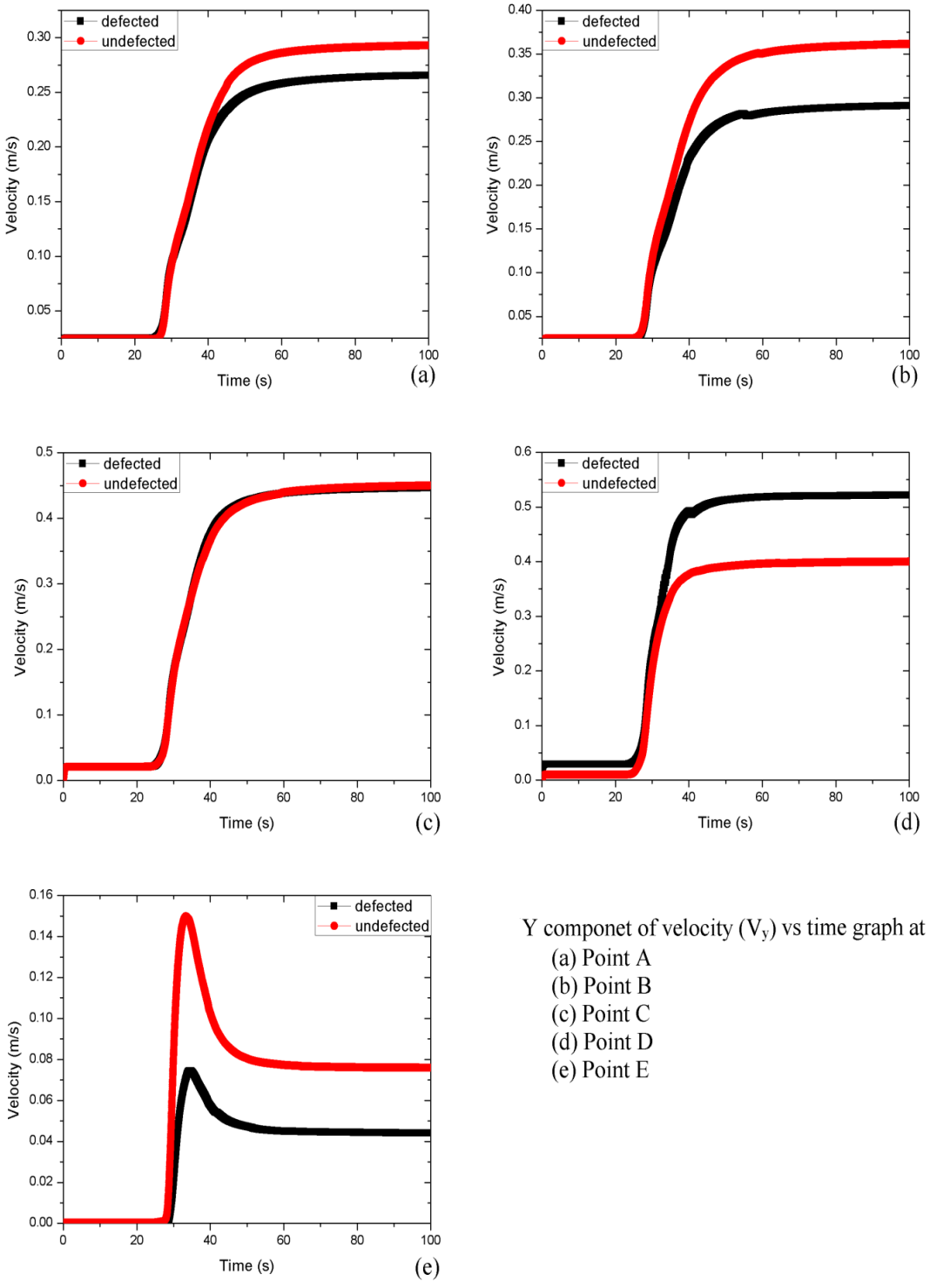

Y componet of velocity (V_y) vs time graph at
(a) Point A
(b) Point B
(c) Point C
(d) Point D
(e) Point E

Figure 8.8: The Y-velocity (V_y) components of defected and undefected weld geometry at all five points. The graph shows the variation of Y-component of velocity with time.

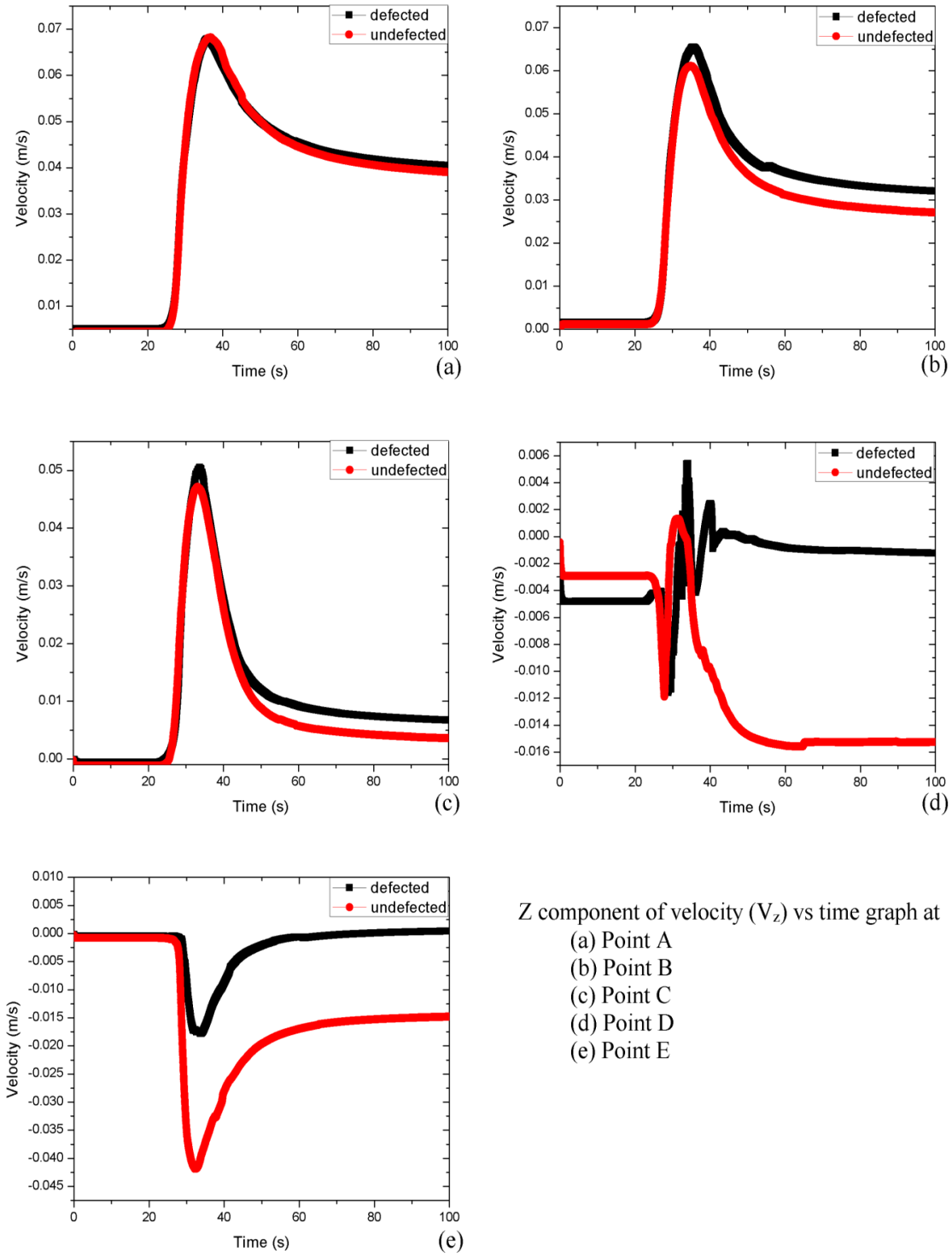

Figure 8.9: The Z-velocity (V_z) components of defected and undefected weld geometry at all five points. The graph shows the variation of Z-component of velocity with time.

The V_y component is the velocity which is perpendicular to the weld line. The V_y component of velocity of material flow on all five points is shown in Figure 8.8.

Among these 5 points, the maximum V_y value is obtained in point D for defected geometry while the maximum value of Vy is observed at Point C for undefected geometry. This suggests that the influence of tool shoulder is more in case of defected geometries. The maximum and minimum value of Vy for defected geometry is 0.5 and 0.042 m/s at point D and E respectively. However, in the case of undefected plate geometry shows 0.45 and 0.076 m/s as the maximum and minimum value at C and E points. This suggests that the undefected plate geometry has smoother velocity profile on moving away from the tool rotation axis. Since the V_y is the most dominant velocity component; the resultant velocity also follows the same trend and magnitude value as discussed previously for point A and B.

The V_z velocity component is responsible for material movement along the thickness of the plate. The positive value shows the material movement towards the shoulder (upward) and the negative value shows the material movement towards the base plate (downward). The V_z component of velocity of material flow on all five points is shown in Figure 8.9. The V_z component at point A, B, C shows no significant change between defected and undefected plates. But a huge difference in the velocity of the two geometries is obtained near the edge of the shoulder. The defected geometry shows the upward movement of the material near the edge (Point D and E) but in case of healthy or undefected weld, a downward movement of material is obtained near the edge. These positive to negative values of V_z on moving away from the rotational axis indicate a circular motion of material along the thickness of the plate for the undefected geometry.

However, in the case of defected geometry, the V_z component values are positive on all five points which indicate there is no downward movement of the material along the thickness of the material. Therefore no circulation movement of the material is obtained along the thickness of the material in case of defected geometry.

8.3 Summary

In this chapter, the velocity response of the defected and undefected plate material flow is studied keeping same welding process parameters. The analysis is carried out using a laminar material flow which was validated and detailed in previous chapter. The velocity components of both the plates are studied separately at five points along

the weld line. The results reveal that the influence of tool shoulder on the material flow velocity is more in case of defected geometry. However, a smoother variation of velocity component of material flow is observed in case of undefected plate.

Chapter 9

Conclusions and Future Scope

9.1 Conclusions

From this research work, the following conclusions can be drawn.

- A 3-D FE model has been successfully developed considering the heat generation due to both sticking and sliding conditions with 5.53 % error in peak temperature. At higher tool rotational speed, the sticking condition dominates over the sliding condition.
- In case of material flow model, an asymmetry is found in the temperature distribution on the AS and RS which is similar to the experimentally obtained results.
- No significant change in material velocity and temperature distribution is observed between turbulent and laminar material flow models. A significant reduction in analysis time is observed in the laminar model in comparison to the turbulent model i.e. laminar analysis is 40 times faster than the turbulent model.
- A helical movement of the material is formed which moves around the pin in FSW process both for clockwise and anti-clockwise rotation of the tool.
- On the advancing side, the swirling movement is observed during the welding near the top surface of the material and on the other hand at retreating side, this movement is towards the bottom surface of the workpiece.
- The tool pin profile has a significant effect in the nugget zone while it has a negligible effect on the material flow behaviour away from the nugget zone.
- The top surface material movement is governed by the tool shoulder but the lateral and upward material movement inside the plate is governed by the pin profile.

- The swirling movement is found in all seven types of tool pin geometries but the origin of the swirl and its size is different in each case. The swirl zone size becomes more compact near to the pin in case threaded pin geometry which is desirable.
- In case cylindrical pin profile, the heating and deformation regions are more uniform thus a uniform viscosity profile is obtained throughout the tool pin height. This uniformity in viscosity profile decreases the probability of defect formation. So, a threaded cylindrical tool pin profile is preferable to obtain a defect free weld.
- The probability of defect formation like worm or tunnel defect is more in advancing side due to the presence of flow separation zone on the advancing side.
- For dissimilar materials FSW, on the Copper side, the heat dissipation is much faster than the Aluminium side, thus the isotherms obtained on the Cu side are much larger than the Al side.
- In the material flow analysis, the peak magnitude of each component of velocity is higher in case defected weld in the comparison with undefected weld.
- The undefected geometry provided much smoother variation in velocity component of material flow in comparison to the defected geometry. A steep rise and fall in velocity magnitude of X component are observed on moving away from the tool rotation axis along the weld line.
- A good circulation of material is observed for healthy weld geometry along the thickness of the plate. However, no circulation of material is observed along the thickness of the weld plate for a defected geometry.

9.2 Future scope

The current study is focused on the field of the material flow behaviour of the FSW process. The study can be extended to the following future work.

- The study can be used to understand the material flow behaviour of a hybrid FSW process.
- The current study can be used to find the material flow behaviour in case of different defect formation in the FSW process.
- The study can be utilised for any other combination of materials for similar as well as dissimilar material.
- The study can be further extended to thermo-mechanical analysis for residual stresses and fatigue life prediction.

Bibliography

[1] E. Nicholas, "Developments in the friction-stir welding of metals," in *ICAA-6, 6th International Conference on Aluminium Alloys.* , Toyohashi, Japan, 1998.

[2] E. D. N. W.M. Thomas, J.C. Needham, M.G. Murch, P. Temple-Smith, C.J. Dawes, "Friction-stir butt welding," 9125978.8, 1991.

[3] F. Stodolsky, A. Vyas, R. Cuenca, and L. Gaines, "Life-Cycle Energy Savings Potential from Aluminum-Intensive Vehicles," 1995.

[4] L. Marretta, R. Di Lorenzo, F. Micari, J. Arinez, and D. Dornfeld, "Material Substitution for Automotive Applications: A Comparative Life Cycle Analysis," in *Leveraging Technology for a Sustainable World: Proceedings of the 19th CIRP Conference on Life Cycle Engineering, University of California at Berkeley, Berkeley, USA, May 23 - 25, 2012*, D. A. Dornfeld and B. S. Linke, Eds., ed Berlin, Heidelberg: Springer Berlin Heidelberg, 2012, pp. 61-66.

[5] H. Mahadevan and T. R. Ramachandran, "Recent trends in alumina and aluminium production technology," *Bulletin of Materials Science,* vol. 19, pp. 905-920, 1996.

[6] G. Mathers, *The welding of aluminium and its alloys*: Woodhead publishing, 2002.

[7] E. Nicholas, "Developments in the friction stir welding of metals," in *ICAA-6: 6 th International Conference on Aluminium Alloys, Toyohashi, Japan, 5-10 Japan 1998*, 1998, pp. 139-151.

[8] W. J. Arbegast, "Friction stir welding after a decade of development," *Welding Journal,* vol. 85, pp. 28-35, 2006.

[9] P. T. Houldcroft, Feng, Fim, and Fweldi, "Welding process developments and future trends," *Materials & Design,* vol. 7, pp. 162-169, 1986.

[10] R. W. Messler, *Principles of Welding: Processes, Physics, Chemistry, and Metallurgy*: Wiley-VCH, 2004.

[11] D. Hattingh, T. Van Niekerk, C. Blignault, G. Kruger, and M. James, "Analysis of the FSW force footprint and its relationship with process parameters to optimise weld performance and tool design," *Welding in the World,* vol. 48, pp. 50-58, 2004.

[12] L. Murr, G. Liu, and J. McClure, "Dynamic recrystallization in friction-stir welding of aluminium alloy 1100," *Journal of materials science letters,* vol. 16, pp. 1801-1803, 1997.

[13] S. Gopalakrishnan and N. Murugan, "Prediction of tensile strength of friction stir welded aluminium matrix TiC p particulate reinforced composite," *Materials & Design,* vol. 32, pp. 462-467, 2011.

[14] Z. Chen, T. Pasang, and Y. Qi, "Shear flow and formation of Nugget zone during friction stir welding of aluminium alloy 5083-O," *Materials Science and Engineering: A,* vol. 474, pp. 312-316, 2008.

[15] T. Hirata, T. Oguri, H. Hagino, T. Tanaka, S. W. Chung, Y. Takigawa, *et al.*, "Influence of friction stir welding parameters on grain size and formability in 5083 aluminum alloy," *Materials Science and Engineering: A,* vol. 456, pp. 344-349, 2007.

[16] K. Elangovan and V. Balasubramanian, "Influences of pin profile and rotational speed of the tool on the formation of friction stir processing zone in AA2219 aluminium alloy," *Materials Science and Engineering: A*, vol. 459, pp. 7-18, 2007.
[17] S. Chionopoulos, C. Sarafoglou, D. Pantelis, and V. Papazoglou, "Effect of tool pin and welding parameters on Friction Stir Welded (FSW) marine aluminium alloys," in *Proceedings of the 3rd International Conference on Manufacturing Engineering (ICMEN)*, 2008, pp. 1-3.
[18] J. R. Davis, *Aluminum and aluminum alloys*: ASM international, 1993.
[19] M. B. D. Ellis and M. Strangwood, "Welding of rapidly solidified alloy 8009 (Al-8.5Fe-1.7Si-1.3V): preliminary study," *Materials Science and Technology*, vol. 12, pp. 970-7, 1996.
[20] L. E. Murr, G. Liu, and J. C. McClure, "Dynamic recrystallization in friction-stir welding of aluminium alloy 1100," *Journal of Materials Science Letters*, vol. 16, pp. 1801-3, 1997.
[21] O. V. Flores, C. Kennedy, L. E. Murr, D. Brown, S. Pappu, B. M. Nowak, *et al.*, "Microstructural issues in a friction-stir-welded aluminum alloy," *Scripta Materialia*, vol. 38, pp. 703-8, 1998.
[22] L. E. Murr, G. Liu, and J. C. McClure, "A TEM study of precipitation and related microstructures in friction-stir-welded 6061 aluminium," *Journal of Materials Science*, vol. 33, pp. 1243-51, 1998.
[23] Y. S. Sato, H. Kokawa, M. Enomoto, and S. Jogan, "Microstructural evolution of 6063 aluminum during friction-stir welding," *Metallurgical and Materials Transactions A (Physical Metallurgy and Materials Science)*, vol. 30A, pp. 2429-37, 1999.
[24] M. W. Mahoney, C. G. Rhodes, J. G. Flintoff, R. A. Spuriing, and W. H. Bingel, "Properties of friction-stir-welded 7075 T651 aluminum," *Metallurgical and Materials Transactions A (Physical Metallurgy and Materials Science)*, vol. 29A, pp. 1955-64, 1998.
[25] S. Benavides, Y. Li, L. E. Murr, D. Brown, and J. C. McClure, "Low-temperature friction-stir welding of 2024 aluminum," *Scripta Materialia*, vol. 41, pp. 809-815, 1999.
[26] E. Schofer, "Friction stir welding-joining of aluminium with low heat input," *Materialwissenschaft und Werkstofftechnik*, vol. 30, pp. 693-6, 1999.
[27] L. E. Murr, R. D. Flores, O. V. Flores, J. C. McClure, G. Liu, and D. Brown, "Friction-stir welding: microstructural characterization," *Materials Research Innovations*, vol. 1, pp. 211-23, 1998.
[28] M. Peel, A. Steuwer, M. Preuss, and P. J. Withers, "Microstructure, mechanical properties and residual stresses as a function of welding speed in aluminium AA5083 friction stir welds," *Acta Materialia*, vol. 51, pp. 4791-4801, 2003.
[29] K. Elangovan and V. Balasubramanian, "Influences of tool pin profile and welding speed on the formation of friction stir processing zone in AA2219 aluminium alloy," *Journal of Materials Processing Technology*, vol. 200, pp. 163-175, 2008.
[30] H. J. Liu, H. J. Zhang, and L. Yu, "Effect of welding speed on microstructures and mechanical properties of underwater friction stir welded 2219 aluminum alloy," *Materials & Design*, vol. 32, pp. 1548-1553, 2011.
[31] T. Sakthivel, G. S. Sengar, and J. Mukhopadhyay, "Effect of welding speed on microstructure and mechanical properties of friction-stir-welded aluminum," *The*

International Journal of Advanced Manufacturing Technology, vol. 43, pp. 468-473, 2009.

[32] P. Cavaliere, G. Campanile, F. Panella, and A. Squillace, "Effect of welding parameters on mechanical and microstructural properties of AA6056 joints produced by Friction Stir Welding," *Journal of Materials Processing Technology*, vol. 180, pp. 263-270, 2006.

[33] Y. G. Kim, H. Fujii, T. Tsumura, T. Komazaki, and K. Nakata, "Effect of welding parameters on microstructure in the stir zone of FSW joints of aluminum die casting alloy," *Materials Letters*, vol. 60, pp. 3830-3837, 2006.

[34] P. Cavaliere, A. Squillace, and F. Panella, "Effect of welding parameters on mechanical and microstructural properties of AA6082 joints produced by friction stir welding," *Journal of Materials Processing Technology*, vol. 200, pp. 364-372, 2008.

[35] H. Lombard, D. G. Hattingh, A. Steuwer, and M. N. James, "Optimising FSW process parameters to minimise defects and maximise fatigue life in 5083-H321 aluminium alloy," *Engineering Fracture Mechanics*, vol. 75, pp. 341-354, 2008.

[36] V. Balasubramanian, "Relationship between base metal properties and friction stir welding process parameters," *Materials Science and Engineering: A*, vol. 480, pp. 397-403, 2008.

[37] M. Jariyaboon, A. Davenport, R. Ambat, B. Connolly, S. Williams, and D. Price, "The effect of welding parameters on the corrosion behaviour of friction stir welded AA2024–T351," *Corrosion Science*, vol. 49, pp. 877-909, 2007.

[38] M. Ericsson and R. Sandström, "Influence of welding speed on the fatigue of friction stir welds, and comparison with MIG and TIG," *International Journal of Fatigue*, vol. 25, pp. 1379-1387, 2003.

[39] K. Yong-Jai, S. Seong-Beom, and P. Dong-Hwan, "Friction stir welding of 5052 aluminum alloy plates," *Transactions of Nonferrous Metals Society of China*, vol. 19, pp. s23-s27, 2009.

[40] C. H. K. Krasnowski, S. Dymek, "Influence of the tool shape and weld configuration on microstructure and mechanical properties of the Al 6082 alloy FSW joints," *archives of civil and mechanical engineering*, pp. 133-141, 2015.

[41] P. A. C. H. R. Shercliff, "Development of Trivex friction stir welding tool Part 2 – three-dimensional flow modelling," *Science and Technology of Welding and Joining*, vol. 4, pp. 352-361, 2004.

[42] Y. Tozaki, Y. Uematsu, and K. Tokaji, "A newly developed tool without probe for friction stir spot welding and its performance," *Journal of Materials Processing Technology*, vol. 210, pp. 844-851, 2010.

[43] A. Arora, A. De, and T. DebRoy, "Toward optimum friction stir welding tool shoulder diameter," *Scripta Materialia*, vol. 64, pp. 9-12, 2011.

[44] H. Fujii, L. Cui, M. Maeda, and K. Nogi, "Effect of tool shape on mechanical properties and microstructure of friction stir welded aluminum alloys," *Materials Science and Engineering: A*, vol. 419, pp. 25-31, 2006.

[45] C. B. D. G. Hattingh, T.I. van Niekerk, M.N. James, "Characterization of the influences of FSW tool geometry on welding forces and weld tensile strength using an instrumented tool," *Journal of materials processing technology*, pp. 46-57, 2005.

[46] D. Rodrigues, A. Loureiro, C. Leitao, R. Leal, B. Chaparro, and P. Vilaça, "Influence of friction stir welding parameters on the microstructural and mechanical properties of AA 6016-T4 thin welds," *Materials & Design*, vol. 30, pp. 1913-1921, 2009.

[47] R. Rai, A. De, H. K. D. H. Bhadeshia, and T. DebRoy, "Review: friction stir welding tools," *Science and Technology of Welding and Joining,* vol. 16, pp. 325-342, 2011.
[48] D. Bakavos and P. Prangnell, "Effect of reduced or zero pin length and anvil insulation on friction stir spot welding thin gauge 6111 automotive sheet," *Science and Technology of Welding and Joining,* vol. 14, pp. 443-456, 2009.
[49] P. A. Colegrove and H. Shercliff, "Development of Trivex friction stir welding tool Part 2–three-dimensional flow modelling," *Science and Technology of Welding and Joining,* vol. 9, pp. 352-361, 2004.
[50] P. Colegrove and H. Shercliff, "Experimental and numerical analysis of aluminium alloy 7075-T7351 friction stir welds," *Science and Technology of Welding and Joining,* vol. 8, pp. 360-368, 2003.
[51] K. Kumar, S. V. Kailas, and T. S. Srivatsan, "Influence of tool geometry in friction stir welding," *Materials and Manufacturing Processes,* vol. 23, pp. 188-194, 2008.
[52] A. Scialpi, L. De Filippis, and P. Cavaliere, "Influence of shoulder geometry on microstructure and mechanical properties of friction stir welded 6082 aluminium alloy," *Materials & Design,* vol. 28, pp. 1124-1129, 2007.
[53] H. Atharifar, D. Lin, and R. Kovacevic, "Numerical and experimental investigations on the loads carried by the tool during friction stir welding," *Journal of Materials Engineering and Performance,* vol. 18, pp. 339-350, 2009.
[54] H. Badarinarayan, Y. Shi, X. Li, and K. Okamoto, "Effect of tool geometry on hook formation and static strength of friction stir spot welded aluminum 5754-O sheets," *International Journal of Machine Tools and Manufacture,* vol. 49, pp. 814-823, 2009.
[55] N. Rodriguez, E. Almanza, C. Alvarez, and L. Murr, "Study of friction stir welded A319 and A413 aluminum casting alloys," *Journal of materials science,* vol. 40, pp. 4307-4312, 2005.
[56] O. Lorrain, V. Favier, H. Zahrouni, and D. Lawrjaniec, "Understanding the material flow path of friction stir welding process using unthreaded tools," *Journal of Materials Processing Technology,* vol. 210, pp. 603-609, 2010.
[57] C. D. Sorensen and A. L. Stahl, "Experimental measurements of load distributions on friction stir weld pin tools," *Metallurgical and Materials Transactions B,* vol. 38, pp. 451-459, 2007.
[58] M. Simoncini and A. Forcellese, "Effect of the welding parameters and tool configuration on micro- and macro-mechanical properties of similar and dissimilar FSWed joints in AA5754 and AZ31 thin sheets," *Materials & Design,* vol. 41, pp. 50-60, 2012.
[59] A. L. Lafly, D. Alléhaux, F. Marie, C. Dalle Donne, and G. Biallas, "Microstructure and Mechanical Properties of the Aluminium Alloy 6056 Welded by Friction Stir Welding Techniques," *Welding in the World,* vol. 50, pp. 98-106, 2006.
[60] H. Zhang, M. Wang, X. Zhang, and G. Yang, "Microstructural characteristics and mechanical properties of bobbin tool friction stir welded 2A14-T6 aluminum alloy," *Materials & Design (1980-2015),* vol. 65, pp. 559-566, 2015.
[61] T. Azimzadegan and S. Serajzadeh, "An Investigation into Microstructures and Mechanical Properties of AA7075-T6 during Friction Stir Welding at Relatively High Rotational Speeds," *Journal of Materials Engineering and Performance,* vol. 19, pp. 1256-1263, 2010.

[62] P. B. Prangnell and C. P. Heason, "Grain structure formation during friction stir welding observed by the 'stop action technique'," *Acta Materialia,* vol. 53, pp. 3179-3192, 2005.
[63] M. Esmaily, N. Mortazavi, W. Osikowicz, H. Hindsefelt, J. E. Svensson, M. Halvarsson, *et al.*, "Bobbin and conventional friction stir welding of thick extruded AA6005-T6 profiles," *Materials & Design,* vol. 108, pp. 114-125, 2016.
[64] H. Uzun, "Friction stir welding of SiC particulate reinforced AA2124 aluminium alloy matrix composite," *Materials & Design,* vol. 28, pp. 1440-1446, 2007.
[65] L. Marzoli, A. Strombeck, J. Dos Santos, C. Gambaro, and L. Volpone, "Friction stir welding of an AA6061/Al2O3/20p reinforced alloy," *Composites Science and Technology,* vol. 66, pp. 363-371, 2006.
[66] P. Cavaliere, R. Nobile, F. Panella, and A. Squillace, "Mechanical and microstructural behaviour of 2024–7075 aluminium alloy sheets joined by friction stir welding," *International Journal of Machine Tools and Manufacture,* vol. 46, pp. 588-594, 2006.
[67] P. Cavaliere, A. De Santis, F. Panella, and A. Squillace, "Effect of welding parameters on mechanical and microstructural properties of dissimilar AA6082–AA2024 joints produced by friction stir welding," *Materials & Design,* vol. 30, pp. 609-616, 2009.
[68] C. Shen, J. Zhang, and J. Ge, "Microstructures and electrochemical behaviors of the friction stir welding dissimilar weld," *Journal of environmental sciences,* vol. 23, pp. S32-S35, 2011.
[69] L. E. Murr, Y. Li, R. D. Flores, E. A. Trillo, and J. C. McClure, "Intercalation vortices and related microstructural features in the friction-stir welding of dissimilar metals," *Materials Research Innovations,* vol. 2, pp. 150-63, 1998.
[70] L. Ying, L. E. Murr, and J. C. McClure, "Solid-state flow visualization in the friction-stir welding of 2024 Al to 6061 Al," *Scripta Materialia,* vol. 40, pp. 1041-6, 1999.
[71] A. P. Reynolds, W. D. Lockwood, and T. U. Seidel, "Processing-property correlation in friction stir welds," *Materials Science Forum,* vol. 331-337, pp. 1719-24, 2000.
[72] R. S. Mishra and M. W. Mahoney, "Friction stir processing: a new grain refinement technique to achieve high strain rate superplasticity in commercial alloys," in *Materials Science Forum*, 2001, pp. 507-514.
[73] P. B. Berbon, W. H. Bingel, R. S. Mishra, C. C. Bampton, and M. W. Mahoney, "Friction stir processing: a tool to homogenize nanocomposite aluminum alloys," *Scripta Materialia,* vol. 44, pp. 61-66, 2001.
[74] B. London, M. Mahoney, W. Bingel, M. Calabrese, R. Bossi, and D. Waldron, "Material flow in friction stir welding monitored with Al-SiC and Al-W composite markers," *TMS2003, CA, K. Jata et al., eds,* p. 3, 2003.
[75] Z. Ma, S. R. Sharma, R. S. Mishra, and M. W. Mahoney, "Microstructural modification of cast aluminum alloys via friction stir processing," in *Materials Science Forum*, 2003, pp. 2891-2896.
[76] J. Schneider, R. Beshears, and A. C. Nunes Jr, "Interfacial sticking and slipping in the friction stir welding process," *Materials Science and Engineering: A,* vol. 435, pp. 297-304, 2006.
[77] B. Li, Y. Shen, and W. Hu, "The study on defects in aluminum 2219-T6 thick butt friction stir welds with the application of multiple non-destructive testing methods," *Materials & Design,* vol. 32, pp. 2073-2084, 2011.

[78] R. Keivani, B. Bagheri, F. Sharifi, M. Ketabchi, and M. Abbasi, "Effects of pin angle and preheating on temperature distribution during friction stir welding operation," *Transactions of Nonferrous Metals Society of China*, vol. 23, pp. 2708-2713, 2013.
[79] M. Grujicic, G. Arakere, H. Yalavarthy, T. He, C.-F. Yen, and B. Cheeseman, "Modeling of AA5083 material-microstructure evolution during butt friction-stir welding," *Journal of Materials Engineering and Performance*, vol. 19, pp. 672-684, 2010.
[80] K. Kumar and S. V. Kailas, "The role of friction stir welding tool on material flow and weld formation," *Materials Science and Engineering: A*, vol. 485, pp. 367-374, 2008.
[81] X. Hou, X. Yang, L. Cui, and G. Zhou, "Influences of joint geometry on defects and mechanical properties of friction stir welded AA6061-T4 T-joints," *Materials & Design*, vol. 53, pp. 106-117, 2014.
[82] Y. Zhao, L. Zhou, Q. Wang, K. Yan, and J. Zou, "Defects and tensile properties of 6013 aluminum alloy T-joints by friction stir welding," *Materials & Design*, vol. 57, pp. 146-155, 2014.
[83] Y. S. Sato, H. Takauchi, S. H. C. Park, and H. Kokawa, "Characteristics of the kissing-bond in friction stir welded Al alloy 1050," *Materials Science and Engineering: A*, vol. 405, pp. 333-338, 2005.
[84] S. Di, X. Yang, D. Fang, and G. Luan, "The influence of zigzag-curve defect on the fatigue properties of friction stir welds in 7075-T6 Al alloy," *Materials chemistry and physics*, vol. 104, pp. 244-248, 2007.
[85] R. Crawford, G. Cook, A. Strauss, D. Hartman, and M. Stremler, "Experimental defect analysis and force prediction simulation of high weld pitch friction stir welding," *Science and Technology of Welding and Joining*, vol. 11, pp. 657-665, 2006.
[86] R. Leal and A. Loureiro, "Effect of overlapping friction stir welding passes in the quality of welds of aluminium alloys," *Materials & Design*, vol. 29, pp. 982-991, 2008.
[87] H. Liu and H. Zhang, "Repair welding process of friction stir welding groove defect," *Transactions of Nonferrous Metals Society of China*, vol. 19, pp. 563-567, 2009.
[88] A. P. Reynolds, "Visualisation of material flow in autogenous friction stir welds," *Science and Technology of Welding and Joining*, vol. 5, pp. 120-124, 2000.
[89] M. Guerra, J. C. McClure, L. E. Murr, and A. C. Nunes, "Metal flow during friction stir welding," in *Friction Stir Welding and Processing*, 2001, pp. 25-34.
[90] H. N. B. Schmidt, T. L. Dickerson, and J. H. Hattel, "Material flow in butt friction stir welds in AA2024-T3," *Acta Materialia*, vol. 54, pp. 1199-1209, 2006.
[91] Y. Morisada, H. Fujii, Y. Kawahito, K. Nakata, and M. Tanaka, "Three-dimensional visualization of material flow during friction stir welding by two pairs of X-ray transmission systems," *Scripta Materialia*, vol. 65, pp. 1085-1088, 2011.
[92] B. C. Liechty and B. W. Webb, "Flow field characterization of friction stir processing using a particle-grid method," *Journal of Materials Processing Technology*, vol. 208, pp. 431-443, 2008.
[93] K. Colligan, "Material flow behavior during friction welding of aluminum," *Weld J*, vol. 75, pp. 229s-237s, 1999.

[94] R. Kumar, V. Pancholi, and R. P. Bharti, "Material flow visualization and determination of strain rate during friction stir welding," *Journal of Materials Processing Technology*, vol. 255, pp. 470-476, 2018.
[95] E. L. Rooy, "Introduction to aluminum and aluminum alloys," *ASM International, Metals Handbook, Tenth Edition.*, vol. 2, pp. 3-14, 1990.
[96] D. Tyler and W. Black, "Introduction to copper and copper alloys," *ASM International, Metals Handbook, Tenth Edition.*, vol. 2, pp. 216-240, 1990.
[97] I. Galvão, A. Loureiro, and D. Rodrigues, "Critical review on friction stir welding of aluminium to copper," *Science and Technology of Welding and Joining*, vol. 21, pp. 523-546, 2016.
[98] P. Xue, D. Ni, D. Wang, B. Xiao, and Z. Ma, "Effect of friction stir welding parameters on the microstructure and mechanical properties of the dissimilar Al–Cu joints," *Materials science and engineering: A*, vol. 528, pp. 4683-4689, 2011.
[99] H. J. Liu, J. J. Shen, L. Zhou, Y. Q. Zhao, C. Liu, and L. Y. Kuang, "Microstructural characterisation and mechanical properties of friction stir welded joints of aluminium alloy to copper," *Science and Technology of Welding and Joining*, vol. 16, pp. 92-98, 2011.
[100] A. Abdollah-Zadeh, T. Saeid, and B. Sazgari, "Microstructural and mechanical properties of friction stir welded aluminum/copper lap joints," *Journal of alloys and Compounds*, vol. 460, pp. 535-538, 2008.
[101] H. Barekatain, M. Kazeminezhad, and A. Kokabi, "Microstructure and mechanical properties in dissimilar butt friction stir welding of severely plastic deformed aluminum AA 1050 and commercially pure copper sheets," *Journal of Materials Science & Technology*, vol. 30, pp. 826-834, 2014.
[102] M. F. X. Muthu and V. Jayabalan, "Tool travel speed effects on the microstructure of friction stir welded aluminum–copper joints," *Journal of Materials Processing Technology*, vol. 217, pp. 105-113, 2015.
[103] I. Galvao, J. Oliveira, A. Loureiro, and D. Rodrigues, "Formation and distribution of brittle structures in friction stir welding of aluminium and copper: influence of process parameters," *Science and Technology of Welding and Joining*, vol. 16, pp. 681-689, 2011.
[104] H. Bisadi, A. Tavakoli, M. T. Sangsaraki, and K. T. Sangsaraki, "The influences of rotational and welding speeds on microstructures and mechanical properties of friction stir welded Al5083 and commercially pure copper sheets lap joints," *Materials & Design*, vol. 43, pp. 80-88, 2013.
[105] I. Galvao, R. Leal, A. Loureiro, and D. Rodrigues, "Material flow in heterogeneous friction stir welding of aluminium and copper thin sheets," *Science and technology of welding and joining*, vol. 15, pp. 654-660, 2010.
[106] C. Tan, Z. Jiang, L. Li, Y. Chen, and X. Chen, "Microstructural evolution and mechanical properties of dissimilar Al–Cu joints produced by friction stir welding," *Materials & Design*, vol. 51, pp. 466-473, 2013.
[107] S. Kahl and W. Osikowicz, "Composite aluminum-copper sheet material by friction stir welding and cold rolling," *Journal of materials engineering and performance*, vol. 22, pp. 2176-2184, 2013.
[108] J. Ouyang, E. Yarrapareddy, and R. Kovacevic, "Microstructural evolution in the friction stir welded 6061 aluminum alloy (T6-temper condition) to copper," *Journal of Materials Processing Technology*, vol. 172, pp. 110-122, 2006.
[109] H. Okamura and K. Aota, "Joining of dissimilar materials with friction stir welding," *Welding international*, vol. 18, pp. 852-860, 2004.

[110] C. Genevois, M. Girard, B. Huneau, X. Sauvage, and G. Racineux, "Interfacial reaction during friction stir welding of Al and Cu," *Metallurgical and Materials Transactions A*, vol. 42, pp. 2290, 2011.
[111] M. Avettand-Fenoël, R. Taillard, G. Ji, and D. Goran, "Multiscale study of interfacial intermetallic compounds in a dissimilar Al 6082-T6/Cu friction-stir weld," *Metallurgical and Materials Transactions A*, vol. 43, pp. 4655-4666, 2012.
[112] P. Vilaça, L. Quintino, and J. F. dos Santos, "iSTIR—analytical thermal model for friction stir welding," *Journal of materials processing technology*, vol. 169, pp. 452-465, 2005.
[113] Y. Hwang, Z. Kang, Y. Chiou, and H. Hsu, "Experimental study on temperature distributions within the workpiece during friction stir welding of aluminum alloys," *International Journal of Machine Tools and Manufacture*, vol. 48, pp. 778-787, 2008.
[114] D. Kim, H. Badarinarayan, J. H. Kim, C. Kim, K. Okamoto, R. Wagoner, *et al.*, "Numerical simulation of friction stir butt welding process for AA5083-H18 sheets," *European Journal of Mechanics-A/Solids*, vol. 29, pp. 204-215, 2010.
[115] C. Chen and R. Kovacevic, "Finite element modeling of friction stir welding—thermal and thermomechanical analysis," *International Journal of Machine Tools and Manufacture*, vol. 43, pp. 1319-1326, 2003.
[116] P. Vilaça, L. Quintino, J. F. dos Santos, R. Zettler, and S. Sheikhi, "Quality assessment of friction stir welding joints via an analytical thermal model, iSTIR," *Materials Science and Engineering: A*, vol. 445, pp. 501-508, 2007.
[117] C. Hamilton, S. Dymek, and A. Sommers, "A thermal model of friction stir welding in aluminum alloys," *International journal of machine tools and manufacture*, vol. 48, pp. 1120-1130, 2008.
[118] C. Hamilton, A. Sommers, and S. Dymek, "A thermal model of friction stir welding applied to Sc-modified Al–Zn–Mg–Cu alloy extrusions," *International Journal of Machine Tools and Manufacture*, vol. 49, pp. 230-238, 2009.
[119] K. M. Williamson and T. Abdel-Salam, "A moving boundary formulation for recursive plastic heat release during friction stir welding," *Journal of materials processing technology*, vol. 180, pp. 49-52, 2006.
[120] S. Mandal and K. Williamson, "A thermomechanical hot channel approach for friction stir welding," *Journal of materials processing technology*, vol. 174, pp. 190-194, 2006.
[121] M. Song and R. Kovacevic, "Thermal modeling of friction stir welding in a moving coordinate system and its validation," *International Journal of Machine Tools and Manufacture*, vol. 43, pp. 605-615, 2003.
[122] H. J. Aval, S. Serajzadeh, and A. Kokabi, "Evolution of microstructures and mechanical properties in similar and dissimilar friction stir welding of AA5086 and AA6061," *Materials Science and Engineering: A*, vol. 528, pp. 8071-8083, 2011.
[123] G. Buffa, A. Ducato, and L. Fratini, "Numerical procedure for residual stresses prediction in friction stir welding," *Finite elements in analysis and design*, vol. 47, pp. 470-476, 2011.
[124] Z. Zhang and H. Zhang, "Numerical studies on controlling of process parameters in friction stir welding," *Journal of materials processing technology*, vol. 209, pp. 241-270, 2009.

[125] J. H. Hattel, K. L. Nielsen, and C. C. Tutum, "The effect of post-welding conditions in friction stir welds: from weld simulation to ductile failure," *European Journal of Mechanics-A/Solids*, vol. 33, pp. 67-74, 2012.
[126] J. Hilgert, H. N. B. Schmidt, J. F. dos Santos, and N. Huber, "Thermal models for bobbin tool friction stir welding," *Journal of Materials Processing Technology*, vol. 211, pp. 197-204, 2011.
[127] M. Assidi, L. Fourment, S. Guerdoux, and T. Nelson, "Friction model for friction stir welding process simulation: Calibrations from welding experiments," *International Journal of Machine Tools and Manufacture*, vol. 50, pp. 143-155, 2010.
[128] E. Feulvarch, J. Roux, and J. Bergheau, "A simple and robust moving mesh technique for the finite element simulation of Friction Stir Welding," *Journal of Computational and Applied Mathematics*, vol. 246, pp. 269-277, 2013.
[129] M. Chiumenti, M. Cervera, C. A. de Saracibar, and N. Dialami, "Numerical modeling of friction stir welding processes," *Computer methods in applied mechanics and engineering*, vol. 254, pp. 353-369, 2013.
[130] N. Dialami, M. Chiumenti, M. Cervera, and C. A. De Saracibar, "An apropos kinematic framework for the numerical modeling of friction stir welding," *Computers & Structures*, vol. 117, pp. 48-57, 2013.
[131] H. Zhang, Z. Zhang, and J. Chen, "3D modeling of material flow in friction stir welding under different process parameters," *Journal of Materials Processing Technology*, vol. 183, pp. 62-70, 2007.
[132] D. Jacquin, B. De Meester, A. Simar, D. Deloison, F. Montheillet, and C. Desrayaud, "A simple Eulerian thermomechanical modeling of friction stir welding," *Journal of Materials Processing Technology*, vol. 211, pp. 57-65, 2011.
[133] P. Heurtier, M. Jones, C. Desrayaud, J. H. Driver, F. Montheillet, and D. Allehaux, "Mechanical and thermal modelling of friction stir welding," *Journal of materials processing technology*, vol. 171, pp. 348-357, 2006.
[134] V. Soundararajan, S. Zekovic, and R. Kovacevic, "Thermo-mechanical model with adaptive boundary conditions for friction stir welding of Al 6061," *International Journal of Machine Tools and Manufacture*, vol. 45, pp. 1577-1587, 2005.
[135] H. B. Schmidt and J. H. Hattel, "Thermal modelling of friction stir welding," *Scripta Materialia*, vol. 58, pp. 332-337, 2008.
[136] H. Zhang, Z. Zhang, B. Jun, Z. Lei, and J. Chen, "Effect of viscosity on material behavior in friction stir welding process," *Transactions of Nonferrous Metals Society of China*, vol. 16, pp. 1045-1052, 2006.
[137] C. WU, W. ZHANG, S. Lei, and M. CHEN, "Visualization and simulation of plastic material flow in friction stir welding of 2024 aluminium alloy plates," *Transactions of Nonferrous Metals Society of China*, vol. 22, pp. 1445-1451, 2012.
[138] P. F. Mendez, K. E. Tello, and T. J. Lienert, "Scaling of coupled heat transfer and plastic deformation around the pin in friction stir welding," *Acta Materialia*, vol. 58, pp. 6012-6026, 2010.
[139] F. Gemme, Y. Verreman, L. Dubourg, and M. Jahazi, "Numerical analysis of the dwell phase in friction stir welding and comparison with experimental data," *Materials Science and Engineering: A*, vol. 527, pp. 4152-4160, 2010.
[140] S. Hirasawa, H. Badarinarayan, K. Okamoto, T. Tomimura, and T. Kawanami, "Analysis of effect of tool geometry on plastic flow during friction stir spot

welding using particle method," *Journal of materials processing technology*, vol. 210, pp. 1455-1463, 2010.

[141] G. N. Lampeas and I. D. Diamantakos, "Effects of Nonconventional Tools on the Thermo-Mechanical Response of Friction Stir Welded Materials," *Journal of Manufacturing Science and Engineering*, vol. 137, pp. 051020, 2015.

[142] R. Nandan, G. Roy, T. Lienert, and T. DebRoy, "Numerical modelling of 3D plastic flow and heat transfer during friction stir welding of stainless steel," *Science and Technology of Welding and Joining*, vol. 11, pp. 526-537, 2006.

[143] R. Nandan, G. Roy, T. Lienert, and T. Debroy, "Three-dimensional heat and material flow during friction stir welding of mild steel," *Acta Materialia*, vol. 55, pp. 883-895, 2007.

[144] A. K. Kadian. P. Biswas, "A Comparative Study of Material Flow Behavior in Friction Stir Welding Using Laminar and Turbulent Models," *Journal of Materials Engineering and Performance*, vol. 24(10) pp. 4119–4127, 2015.

[145] S. D. C. Hamilton, A. Sommers, "A thermal model of friction stir welding in aluminum alloys," *International Journal of Machine Tools & Manufacture*, pp. 1120–1130, 2008.

[146] M. R. H. Nazari, "Analysis of transient temperature and residual thermal stresses in friction stir welding of aluminum alloy 6061-T6 via numerical simulation," *Int J Adv Manuf Technol*, pp. 143–152, 2011.

[147] R. H. S. A.P. Colegrove, "3-Dimensional CFD modelling of flow round a threaded friction stir welding tool profile," *Journal of Materials Processing Technology*, pp. 320-327, 2005.

[148] A. P. G. K. E. Tello, and P. F. Mendez, "Constants for Hot Deformation Constitutive Models for Recent Experimental Data," *Science and Technology of Welding and Joining*, pp. 260-66, 2010.

[149] S. Gruner and W. Hoyer, "The dynamic viscosity of liquid Cu–Si alloys," *Journal of Alloys and Compounds*, vol. 460, pp. 496-499, 2008.

[150] L. Jin and R. Sandström, "Numerical simulation of residual stresses for friction stir welds in copper canisters," *Journal of Manufacturing Processes*, vol. 14, pp. 71-81, 2012.

List of Publication

International Journals

1. Arun Kumar Kadian and Pankaj Biswas, “The study of material flow behaviour in dissimilar material FSW of AA6061 and Cu-B370 alloys plates,” *Journal of Manufacturing Processes*, Vol. 34, pp 96-105, 2018.

2. Arun Kumar Kadian and Pankaj Biswas, “Effect of tool pin profile on the material flow characteristics of AA6061,” *Journal of Manufacturing Processes*, Vol. 26, pp 382–392, 2017.

3. Arun Kumar Kadian and Pankaj Biswas, “A Comparative Study of Material Flow Behavior in Friction Stir Welding Using Laminar and Turbulent Models,” *Journal of Materials Engineering and Performance*, Vol. 24, pp 4119-4127, 2015.

4. Anil Kumar Deepati, Arun Kumar Kadian and Pankaj Biswas, “Numerical and experimental study on influence of tool plunging force and shoulder size on thermal history of friction stir welding,” *Int. J. Manufacturing Research*, Vol. 10, No. 1, pp 64 – 86, 2015.

5. Arun Kumar Kadian & Pankaj Biswas, "Process Parameters effect on Thermal History of Friction Stir Welding by Considering Combined Stick & Slip Condition of AA6061," *Int. J. Manufacturing Research,* (under review) 2018.

6. Arun Kumar Kadian & Pankaj Biswas, "The comparative study of material flow behaviour of defected and undefected plates FSW," (under preperation).

7. Arun Kumar Kadian & Pankaj Biswas, "A review paper on material flow behaviour of friction stir welding," (under preperation).

8. Arun Kumar Kadian & Pankaj Biswas, "A comparison of Eulerian and Volume of Fluid material flow model for Dissimilar FSW of AA6061 and Cu-B370 alloys plates,"(under preperation).

Conferences

9. Arun Kumar Kadian, Gautam Puri, Pankaj Biswas, "Prediction of Thermal History of Friction Stir Welding by Considering Combined Stick & Slip Condition of AA1100," in 5th International and 26th All India Manufacturing Technology, Design and Research Conference, Guwahati, 2014.

10. Arun Kumar Kadian, Gautam Puri, Suman Das, Pankaj Biswas, "Effect of tool geometry and process parameters on the material flow of friction stir welding," in *5th International and 26th All India Manufacturing Technology, Design and Research Conference*, Guwahati, 2014.

11. Anil Kumar Deepati, Arun Kadian , Leena Nemade and Pankaj Biswas, "Effect of tool shoulder diameter on thermal history of FSW of aluminium alloy," in *Twenty-First International Symposium on Processing and Fabrication of Advanced Materials*, Guwahati, 2012.

12. Deepati Anil Kumar, Pankaj Biswas, Arun Kadian, Leena Nemade, "3D-Finite Element modelling and the effect of backing plate on thermal history of FSW AA5083," in *National Conference on Advances in Welding Technology- Indian welding society. NERIST*, Arunachal Pradesh, 2013.

13. Nandan Kanan Das, Arun Kumar Kadian, Avinish Tiwari, Pardeep Pankaj, Pankaj Biswas, " Transient Thermal Analysis on Friction Stir Welding of AA6061," in *5th International Conference on Production and Industrial Engineering (CPIE-2018),* Bangkok, Thailand, 2018.

14. Pardeep Pankaj, Avinish Tiwari, Arun Kumar Kadian, Pankaj Biswas, "Transient thermal analysis of CO2 laser welding of AISI 304 stainless steel thin plates," in *5th International Conference on Production and Industrial Engineering (CPIE-2018),* Bangkok, Thailand, 2018.